Stratospheric Aerosol Particle Size Retrieval

A Thesis Submitted to the
College of Graduate Studies and Research
in Partial Fulfillment of the Requirements
for the degree of Master of Science
in the Department of Physics and Engineering Physics
University of Saskatchewan
Saskatoon

By
Landon Rieger

Permission to Use

In presenting this thesis in partial fulfilment of the requirements for a Postgraduate degree from the University of Saskatchewan, I agree that the Libraries of this University may make it freely available for inspection. I further agree that permission for copying of this thesis in any manner, in whole or in part, for scholarly purposes may be granted by the professor or professors who supervised my thesis work or, in their absence, by the Head of the Department or the Dean of the College in which my thesis work was done. It is understood that any copying or publication or use of this thesis or parts thereof for financial gain shall not be allowed without my written permission. It is also understood that due recognition shall be given to me and to the University of Saskatchewan in any scholarly use which may be made of any material in my thesis.

Requests for permission to copy or to make other use of material in this thesis in whole or part should be addressed to:

Head of the Department of Physics and Engineering Physics
116 Science Place
University of Saskatchewan
Saskatoon, Saskatchewan
Canada
S7N 5E2

Abstract

The advent of satellite limb scatter measurements has allowed the stratosphere to be studied at a scope unparalleled by previous observational techniques, affording the opportunity to study structures on both small spacial and temporal scales. Utilizing these measurements to their fullest has fueled the development of radiative transfer models to simulate the measurements, but also inversion techniques to retrieve atmospheric parameters. The limb scatter instrument OSIRIS, onboard the Odin satellite, is currently used in conjunction with the SASKTRAN radiative transfer model and multiplicative algebraic reconstruction technique to retrieve stratospheric aerosol extinction. In this work, the aerosol information content of limb scatter measurements is explored and an improved version of the aerosol retrieval is developed through the simultaneous retrieval of a second aerosol parameter, the Ångström coefficient, which is related to particle size.

The sensitivity of limb scatter measurements to aerosol is investigated through forward modelling of OSIRIS measurements as a function of wavelength, satellite geometry and particle size. Information content of the measurements is investigated to determine the feasibility of retrieving various aerosol size parameters and a simple linear inversion technique is tested. Results from this study are used to develop a non-linear inversion technique with minimal sensitivity to the required assumptions.

Incorporation of longer wavelength data into the retrieval allows for the determination of the wavelength dependence of the scattered signal, which when combined with a lognormal particle size distribution of constant mode width allows for the retrieval of aerosol number density and mode radius. Conversion of these parameters to extinction and the Ångström coefficient provides retrieved quantities with minimal dependence on the assumed size distribution. Application of this technique to the OSIRIS data set shows improved extinction results through both internal comparisons of the data and when compared with other results from SAGE II, III and CALIPSO satellite measurements. Although the retrieved Ångström coefficient shows some bias due to the required assumptions, comparisons with the SAGE II data set show considerable improvement over the *a priori* estimate.

Acknowledgements

I have not only learned a tremendous amount, but have also had an exceptional time putting this work together and would like to thank the Institute for Space and Atmospheric Studies, the University of Saskatchewan and the Canadian Space Agency for the financial support that made this possible.

Members of the ISAS department have been a great help, and I would like to thank those who I've worked with on this project. In particular Dr. Nick Lloyd for all of his help and advice, especially in learning and navigating SASKTRAN; Chris Roth for his help with using and improving the infrared data set; and Dr. Doug Degenstein for his sage advice and skeptical ear.

I would like to extend my sincere thanks to my advisor, Dr. Adam Bourassa, whose knowledge and enthusiasm for the subject have been truly contagious. His encouragement and guidance on this project have made it what it is and I am grateful for the opportunity to pursue this work.

Finally, I would like to thank my family whose support has been absolute.

To my parents, Bill and Marlene Rieger.

Contents

List of Figures

Nomenclature

α	Ångstöm Coefficient
γ	Damping factor used in Levenberg-Marquardt algorithm
Θ	Scattering angle, the angle between the incoming and outgoing rays
λ	Wavelength
σ	Scattering cross section
σ_{g}	Mode width of a unimodal distribution
τ	Optical depth
$\hat{\Omega}$	Direction of propagation
a	Albedo, the ratio of upwelling to downwelling radiation
F_0	Solar radiance
$I(s, \hat{\Omega})$	Radiance
$J(s, \hat{\Omega})$	Multiply scattered radiance source term
k	Extinction
n_{aer}	Aerosol particle number density
$\mathrm{p}(\Theta)$	Phase function, the angular distribution of scattered light
r	Radius
r_{g}	Mode radius of a lognormal distribution
s	Position along the line of sight
$\mathbf{A}$	Averaging kernel matrix, describes change in the retrieved state for a change in the true state
$\tilde{\mathbf{b}}$	Forward model parameters
$\mathbf{F}(\mathbf{x}, \tilde{\mathbf{b}})$	Forward model of an observation
$\mathbf{G}$	Gain matrix, describes change in the retrieved state due to change in the measurement
$\mathbf{K}$	Jacobian matrix describing the sensitivity of the forward model
$\mathbf{S}_a$	Covariance of a priori atmospheric state
$\mathbf{S}_m$	Covariance matrix of the retrieved quantity
$\mathbf{S}_\epsilon$	Covariance of measurement noise
$\mathbf{W}$	Weighting matrix used in MART retrievals
$\mathbf{x}$	Atmospheric state vector
$\mathbf{x}_a$	*A priori* estimate of the atmospheric state vector
$\hat{\mathbf{x}}$	Retrieved atmospheric state vector
$\mathbf{y}$	Measurement vector

Chapter 1

Introduction

Remote sensing has played an integral part in advancing knowledge about our physical world, and in particular has been crucial to the study of Earth's atmosphere. No other technique allows for both the scale and precision of atmospheric measurements that remote sensing satellite platforms provide. These measurements have allowed for global maps of atmospheric constituents, surface properties, and temperature and pressure profiles among others. Through measurement of the intensity and spectrum of light reaching an instrument a great deal can be determined about the medium, and in this case the atmosphere, that the light passed through. Some of the earliest satellites designed to monitor atmospheric composition used the occultation approach, where the instrument looks through the atmosphere directly at the sun to produce high resolution vertical profiles, others used nadir geometry to improve coverage and take measurements of an atmospheric column, but with little vertical information. More recently, satellite LIDARs and limb scatter instruments have been used to provide both improved coverage and good vertical resolution.

The limb scatter technique views the atmosphere edge-on, measuring sunlight scattered into the field of view of the instrument. Since this does not require sunrise or sunset events, only that the "edge" or limb of the atmosphere be illuminated by the sun, it provides excellent global coverage as well as vertical information. The cost of limb scattered measurements comes in the more complicated light path; limb measurements are a product of the amount of scattering and the angular distribution of the scattered light. This makes determining atmospheric properties from radiance measurements difficult, and necessitates the use of sophisticated inversion techniques, including the ability to accurately model the measurements in a spherical, multiply scattering atmosphere. While this task is difficult, for molecules the angular dependence of scattered light is well described by the Rayleigh phase function, and so can be modelled accurately knowing only the molecular concentrations. However, the phase function of larger particles is much more variable and depends on their size, shape and composition, making accurate modelling, and hence determination of the true atmospheric state, particularly challenging.

In the stratosphere these larger particles are primarily aerosol droplets composed of water and sulphuric acid. Created through oxidation of sulphur compounds these droplets form an aerosol layer in the relatively stable stratosphere. This layer plays an important role in Earth's radiative balance as well as the stratospheric chemistry. In addition, the size and number of particles is highly variable, with large enhancements due to volcanic activity occurring sporadically. These factors make improved monitoring and understanding of the composition and dynamics of this aerosol layer increasingly important to fully understand Earth's atmosphere.

One satellite performing limb scattered sunlight measurements is the Optical Spectrograph and InfraRed Imaging System (OSIRIS) on the Odin satellite. OSIRIS produces vertical radiance profiles of the upper troposphere and stratosphere which are inverted to produce information on the quantity of light scattered by the aerosol particles. The limitation of this technique is that for the inversion to be performed the angular distribution of scattered light from the aerosols must be known, which requires an assumed aerosol particle size distribution. If this size distribution is assumed incorrectly, then a systematic error in the retrieved quantity results. Thus, it is the goal of this work to use information in the OSIRIS measurements to derive information on stratospheric aerosol particle size distributions, both for the physical importance, as well as the improvement of other retrieved quantities.

A more detailed account of the stratospheric aerosol layer and its importance is contained in Chapter 2, as well as information on the various satellite measurement techniques. There a detailed description of the OSIRIS instrument is given. Following this is the essential background to radiative transfer and the SASKTRAN implementation used to model the OSIRIS measurements. Finally, Chapter 2 describes the theory behind inverse problems and typical solution techniques, in particular the current algorithm used to retrieve aerosol information from the OSIRIS measurements.

Chapter 3 explores the particle size problem in the OSIRIS retrievals through comparison with other aerosol data sets. Here a systematic error is evident in the OSIRIS retrievals that is well explained by incorrect assumptions about the aerosol particle size. Methods that previous groups have used to extract particle size information from measurements are explored as well as the applicability to OSIRIS measurements.

Chapter 4 discusses the aerosol information available from the OSIRIS spectral radiance measurements, both through exploiting the wavelength dependence and the different viewing geometries. Aerosol particles have a broad wavelength response which is studied, as well as the signal dependence on satellite viewing geometry. Using this information, a particle size retrieval technique is

designed and tested through simulated measurements. In Chapter 5 this new retrieval technique is applied to a subset of the OSIRIS measurements and comparisons with other satellite measurements are used to test the fidelity of the new retrieval. Finally, important results and conclusions are summarized in Chapter 6.

Chapter 2

Background

2.1 Aerosols and the Stratosphere

In the late 19$^{\text{th}}$ century a curious phenomenon was discovered through the use of balloon soundings: as the balloon rose through the atmosphere the temperature decreased until approximately 12 km, when an apparent isothermal layer was reached. While initially dismissed as measurement error and corrected out of the data, this temperature inversion was soon found to be the rule rather than the exception, and the stratosphere was discovered (*Hoinka*, 1997). Since then the stratosphere has typically been defined as the region of air above the inversion point in which temperature increases with altitude, and has been the focus of intense study, particularly due to ozone and aerosol concentrations and large scale circulation patterns which can affect the troposphere (*Baldwin et al.*, 2007; *Elsner et al.*, 1999). Beginning at around 17 km in the tropics and 8 km at higher latitudes, the stratosphere extends to approximately 50 km in altitude, and due to the increasing temperature profile is thermodynamically stable (*Andrews et al.*, 1987, chap. 1.1). This limits the vertical transport of species within the layer and results in long lifetimes for stable species that are transported to the stratosphere, often on the order of months or years depending on the species (*Waugh and Hall*, 2002; *McCormick et al.*, 1995).

The majority of stratospheric makeup is dictated by large scale exchange processes with the troposphere such as slow upwelling in the tropics, tropopause folds and the polar vortices, as well as stratospheric circulation patterns such as the Brewer-Dobson circulation. These processes transport chemicals across the tropopause boundary and facilitate mixing of the stratosphere enabling important dynamics and chemistry to occur (*Holton et al.*, 1995). One important reaction is the oxidation of sulphur compounds into hydrated sulphuric acid (*McKeen et al.*, 1984). As sulphuric acid nucleates, the nanometer sized particles condense and coagulate producing liquid droplets of various sizes, typically in the sub-micron range (*Turco et al.*, 1982). As the particles evolve, large particles begin to sediment out and are removed from the stratosphere through the exchange mech-

anisms. Smaller particles can slowly rise through the stratosphere and evaporate in the decreased pressures and increased temperatures of higher altitudes. Taken together, these processes create a relatively stable aerosol layer extending from above the tropopause to approximately 30 km in altitude (*Hamill et al.*, 1997; *Brock et al.*, 1995).

2.1.1 Aerosol Microphysics

The first measurements of the aerosol layer came in the late 1950s using instruments carried on weather balloons that could monitor the number of particles in the range of 0.1 to 1.5 µm (*Junge et al.*, 1961). These experiments found a high sulphur content in the aerosols with more in depth studies finding particles consisting of 75% H_2SO_4 and 25% H_2O by mass under typical stratospheric conditions (*Rosen*, 1971; *Carslaw et al.*, 1995). The primary source of this sulphur is SO_2 and OCS from the troposphere, produced by the oceans, biomass burning, volcanic emissions and anthropogenic sources from fossil fuel burning (*Graf et al.*, 1997; *Andreae and Crutzen*, 1997). OCS has a relatively long lifetime in the troposphere but is present in small amounts and accounts for approximately 30% of the aerosol sulphur budget, with SO_2 providing the majority of the remaining 70% (*Thomason and Peter*, 2006). SO_2 is converted through a chain of reactions to H_2SO_4 quickly in the troposphere, on the order of hours to days, but takes several weeks to be converted in the stratosphere due the relatively low concentrations of OH and H_2O (*Eisinger and Burrows*, 1998).

The size of the particles is much more variable than the composition and is governed by the competing processes of nucleation, condensation, coagulation, sedimentation and evaporation. Often, the resulting size distribution is represented as a lognormal (*Bauman et al.*, 2003; *Bingen et al.*, 2004; *Wurl et al.*, 2010), given by the equation

$$\frac{dn(r)}{dr} = \frac{n_{\text{aer}}}{r\ln(\sigma_g)\sqrt{2\pi}} \exp\left(-\frac{(\ln r - \ln r_g)^2}{2\ln(\sigma_g)^2}\right). \tag{2.1}$$

This provides a distribution with a single peak (or mode) where the number of particles is normally distributed according to the logarithm of particle radius. The number of particles between radius r and $r + dr$ is given by $dn(r)/dr$ and is normalized such that

$$\int_0^\infty \frac{dn(r)}{dr} dr = n_{\text{aer}}. \tag{2.2}$$

Aerosol concentration is then fully described by three parameters: mode radius, r_g, mode width, σ_g, and the total number of particles, n_{aer}. There are theoretical reasons to predict the development of a unimodal lognormal size distribution (*Granqvist and Buhrman*, 1976; *Kiss et al.*, 1999); however, experimental confirmation of the unimodal constraint has been mixed (*Oberbeck et al.*, 1983;

Hayasaka et al., 1998). One of the longest and most comprehensive records of local stratospheric aerosol conditions is from the University of Wyoming's optical particle counters carried on weather balloons. These instruments measure the number of aerosol particles in several size bins, ranging from 0.01 to 2 µm, and have yielded vertical profiles of aerosol concentration as well as particle size over the span of 30 years. These experiments have shown that during low aerosol loading the unimodal lognormal distribution is a good fit to the data. During heavier loading such as after volcanic events, however, a second mode of larger particles is often present. Figure 5 from *Deshler et al.* (2003), recreated here as Figure 2.1, shows the particle size distribution for two cases: a balloon flight in 1993 shortly after the Mount Pinatubo eruption, and a second from 1999, once the stratosphere had returned to approximately background aerosol levels. These tests show a clear bimodal distribution in 1993, but also that the unimodal distribution can be an excellent approximation during background levels.

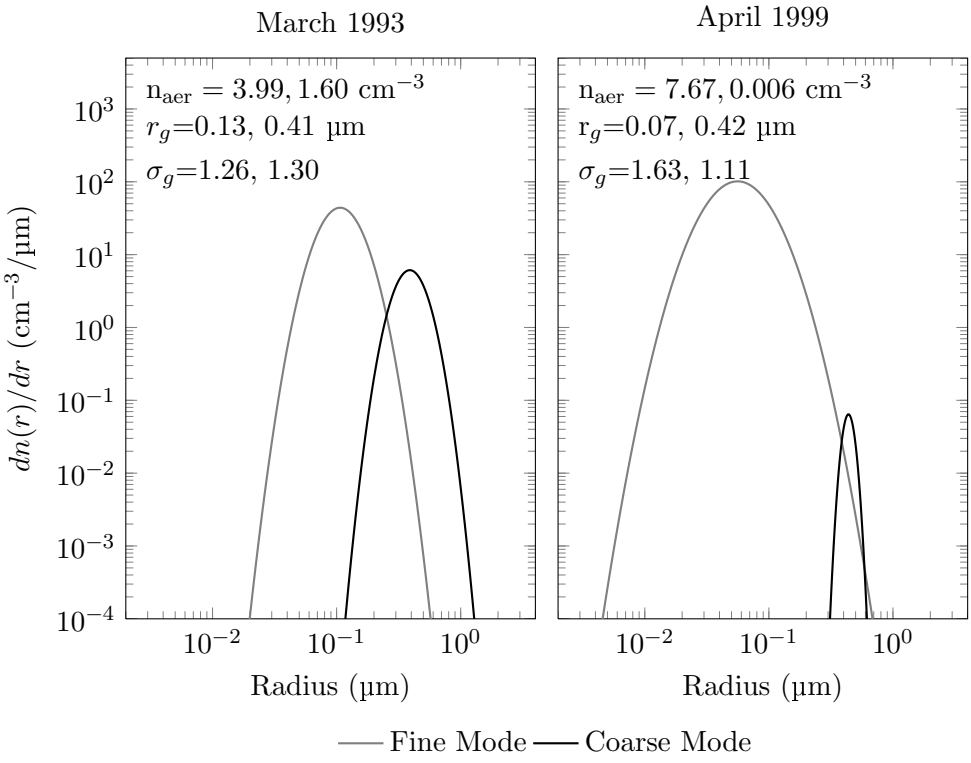

Figure 2.1: Bimodal lognormal size distributions fit to optical particle counter measurements for (a) a 1993 measurement in volcanic aerosol and (b) a 1999 measurement in background aerosol, both at 20 km altitude. The gray line shows the differential fine mode distribution and the black line the differential coarse mode distribution, both assumed to be lognormal. Figure recreated from *Deshler et al.* (2003).

2.1.2 Climate Effects

Aerosols play an important role in the radiative forcing of the atmosphere with several competing effects. Directly, aerosols scatter sunlight, increasing Earth's albedo and reducing warming of the surface (*Lacis et al.*, 1992). Conversely, aerosols also scatter upwelling infrared radiation with an efficiency that is dependent on particle size, increasing the greenhouse effect (*Kiehl and Briegleb*, 1993). Further complicating this is the indirect effect aerosols have through the seeding of clouds, contributing to heterogenous chemistry and ozone depletion (*Hofmann and Solomon*, 1989). Overall, the radiative forcing produced by these effects is relatively small and negative during times of low aerosol loading, referred to as the background level (*Solomon et al.*, 2011). However, large amplifications of the background level can occur during volcanically active periods, such as that produced by the eruption of Mt. Pinatubo in 1991. Pinatubo injected approximately 30 million tons of SO_2 into the stratosphere and the effect was a global cooling of approximately 0.5°C and a heating of the stratosphere by more than 2°C for months following the eruption (*McCormick et al.*, 1995; *Robock*, 2000). The lifetime of these volcanically active periods is also quite long, with the aerosols taking years to return to background levels.

2.2 Atmospheric Remote Sensing

While balloon-borne optical particle counters and ground based LIDARs provide excellent quality measurements they are fundamentally limited in extent. For truly global measurements satellites are required, and have an increasingly important role in the monitoring and tracking of atmospheric changes. In the last few decades numerous satellites have been launched with the capability of monitoring the stratospheric aerosol layer, each with distinct advantages and disadvantages. While OSIRIS uses only the limb scatter technique to monitor the atmosphere, comparisons between data sets made with fundamentally different approaches are valuable tools for assessing the accuracy and precision of measurements and so the major satellite techniques are discussed briefly below.

2.2.1 Occultation

One of most tested and robust methods of atmospheric remote sensing is the solar occultation method shown in Figure 2.2. Here, the satellite watches the sun rise or set, measuring the attenuation of the solar beam as it does so. This method has several advantages including high signal to noise and an inherent calibration through measurement of the exo-atmospheric solar spectrum

before or after each vertical profile is taken. As well, since the satellite is looking directly at the sun, the optical depth of the atmosphere is a straightforward logarithmic ratio of the measured reference spectrum over the measurement. This can then be combined with an "onion peel" technique where each measurement is used with the ones above to determine a vertical extinction profile of the atmosphere (*Chu and McCormick*, 1979). This technique has been used successfully for decades on numerous satellites starting with the Stratospheric Aerosol Measurement (SAM) II launched in 1978 (*McCormick et al.*, 1979), and followed by the Stratospheric Aerosol and Gas Experiments (SAGE) I, II (*Russell and McCormick*, 1989) and III (*Thomason and Taha*, 2003), which were operational until 2005, among others. With the exception of SAM II, these satellites retrieved vertical extinction profiles at numerous wavelengths, providing a valuable, long term, global data set of wavelength-dependent aerosol extinction. The drawback to solar occultation comes in the sampling rate; since measurements are only possible during local sunrise or sunset, this technique is limited to approximately 16 to 32 measurements per day depending on the orbit.

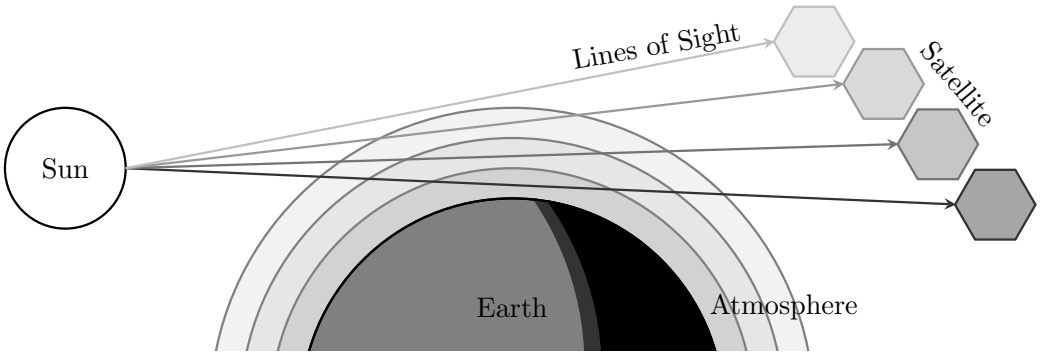

Figure 2.2: Occultation geometry showing a satellite taking measurements at various altitudes.

2.2.2 LIDAR

LIght Detection And Ranging (LIDAR) instruments have been used for atmospheric observations for decades and work by transmitting a laser pulse and monitoring the intensity and polarizations of the backscattered signal. By gating the detector it is possible to measure light that has been scattered from particular distances, yielding very high vertical resolutions. Only recently, have LIDARs been put onto satellites such as the Ice, Cloud, and Land Elevation Satellite (ICESat) (*Schutz et al.*, 2005) and the Cloud-Aerosol Lidar and Infrared Pathfinder Satellite Observations (CALIPSO) (*Winker et al.*, 2007). CALIPSO is a NASA observation platform and uses a two wavelength polarization LIDAR to produce high resolution vertical profiles of clouds and aerosols

along the orbital ground track, as shown in figure 2.3. This technique provides vertical resolution on the order of 10s to 100s of meters, depending on the altitude, and by incorporating polarization information allows for the categorization of aerosols into several types including sulphates, ash, and dust (*Vaughan et al.*, 2004). The disadvantage to using satellite based LIDARs is that signal to noise ratio is low, particularly during daytime measurements, limiting the detection of background level and high altitude aerosols (*Kacenelenbogen et al.*, 2011).

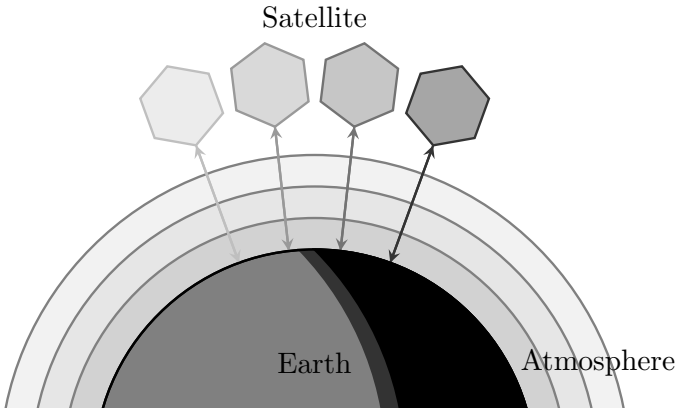

Figure 2.3: LIDAR satellite taking several measurements along a ground track.

2.2.3 Limb Scatter

Limb scattering is a technique used in a small number of satellites including the SCanning Imaging Absorption spectroMeter for Atmospheric CHartographY (*Bovensmann et al.*, 1999), Ozone Mapper Profiler Suite (*Dittman et al.*, 2002; *Rault and Xu*, 2011) and OSIRIS (*Llewellyn et al.*, 2004). These instruments work on the principle of looking slightly above the Earth's surface, measuring light that is scattered into their line of sight. The line of sight is then scanned up or down through the atmosphere, creating a vertical profile of spectral radiances. This allows for good vertical resolution, typically around 1 km, and the ability to take measurements over any sunlit portion of the globe. As mentioned previously, the major drawback to limb scattered measurements is in the complexity of the scattered light. Not only must the atmosphere along the line of sight be considered, but also any region of the atmosphere which may contribute photons to the line of sight through multiple scattering (*Oikarinen et al.*, 1999). While this means a limb scattered signal contains large amounts of information, it also makes extracting the information more difficult, and ultimately relies on the ability to accurately model the observations.

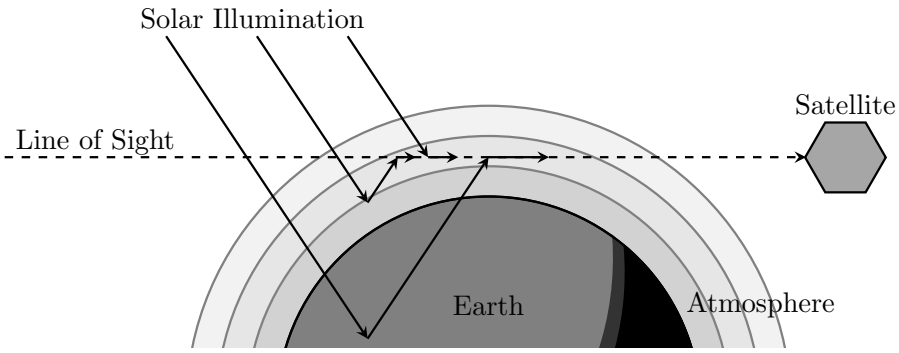

Figure 2.4: Limb geometry measurement technique: shown is a measurement at a single tangent altitude with single, multiple and surface scattered light rays.

2.3 OSIRIS and the Odin Orbit

The Optical Spectrograph and InfraRed Imaging System (OSIRIS) was launched in 2001 onboard the Odin satellite. The Odin orbit is sun-synchronous with an inclination of 98° from the equator. OSIRIS views in the orbital plane and therefore provides measurements from 82°N to 82°S with equatorial crossings at 1800 h and 0600 h for the north and southbound crossings, respectively. This dusk/dawn orbit provides coverage of a large latitude range, but also restricts OSIRIS from taking measurements in the winter hemisphere, as this portion of the globe is not sunlit. As OSIRIS orbits, the satellite nods with each measurement to scan the optical axis from approximately 7 to 65 km or 7 to 100 km above the ground, depending on the scanning mode.

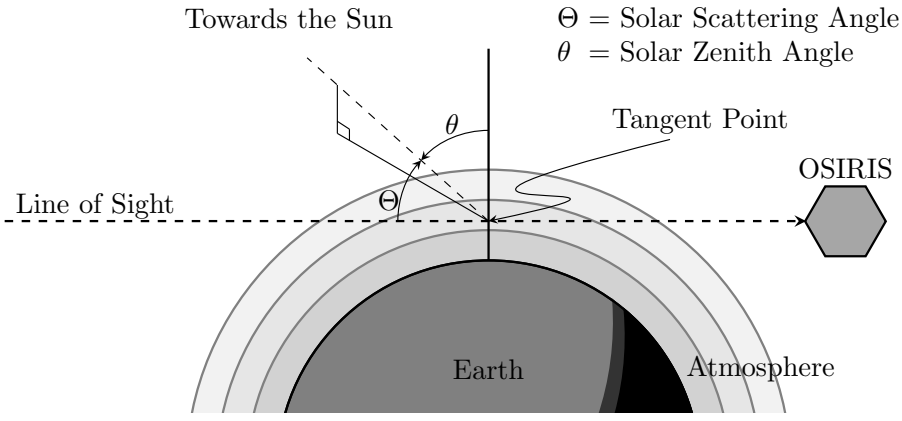

Figure 2.5: OSIRIS solar angle definitions and measurement geometry.

Since OSIRIS does not look directly at the sun, there are two important angles for each measurement, defined from the location along the line of sight that passes closest to the Earth, called the tangent point, shown in Figure 2.5. The solar zenith angle (SZA) is defined as the angle between

the sun and the vertical. Due to the dusk/dawn orbit, this angle varies between about 60° and 120°. The solar scattering angle (SSA) is the angle between the OSIRIS line of sight and the sun and also varies between approximately 60° and 120°.

The OSIRIS measurements can be divided into two sets, ascending track and descending track, based on whether the satellite is moving north or south, respectively. This can provide valuable information for the retrieval of aerosols since after 7.5 orbits the tangent point will be in approximately the same position over the Earth as it was 12 hours prior, except in a different solar geometry. This allows for comparisons between two measurements of approximately the same atmosphere with different viewing angles. Figure 2.6 shows the geometry of two scans, also known as a matched pair, that have measured a similar location, once on the ascending and once on the descending node.

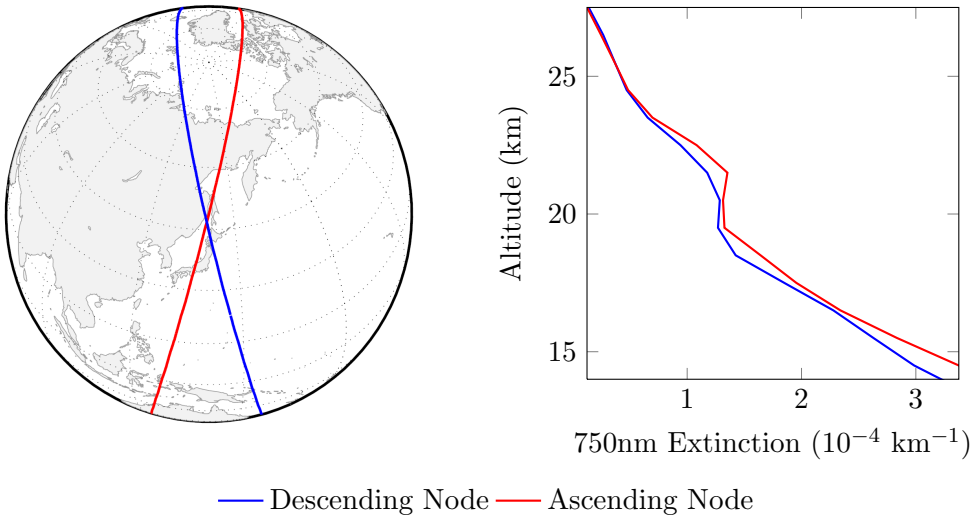

Figure 2.6: Example of a matched ascending (red) and descending node (blue), crossing point is the matched scans, 11222020 and 11229004. Shown on right is the retrieved extinction profiles for the scans.

2.3.1 Optical Spectrograph

The primary instrument onboard OSIRIS is the optical spectrograph which has a single line of sight with a 1 km field of view at the tangent point. As Odin nods the line of sight is scanned vertically to produce an altitude profile of integrated line of sight measurements. The spectrometer focuses spectrally dispersed light on a CCD measuring wavelengths from 274 to 810 nm at approximately 1 nm resolution. Figure 2.7 shows optical spectrograph measurements for a few altitudes from a typical scan; the missing region between approximately 480 and 530 nm is due to the edge of a

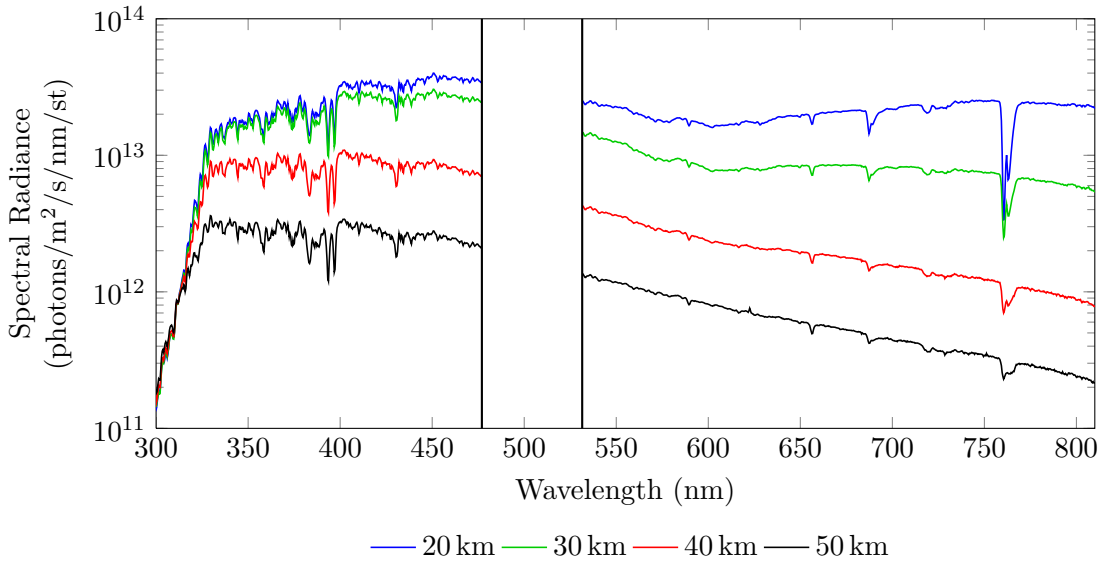

Figure 2.7: Limb spectral radiance measurements as the satellites nods and looks through various tangent altitudes.

spectral order sorting filter that contaminates the measurements. Spectra at high altitudes exhibit broad features such as strong UV absorption due to ozone and a rapidly decaying signal with wavelength due to the strong wavelength dependence of Rayleigh scattering. At lower altitudes UV absorption is still present; in addition, absorption near 600 nm is also apparent due to the Chappuis absorption band. At these altitudes there is also a broad enhancement at longer wavelengths due to scattering by large aerosol particles.

2.3.2 Infrared Imager

The second imaging system onboard Odin is the Infrared Imager. Designed to measure hydroxyl and oxygen emission bands, the InfraRed Imager (IRI) is composed of three vertical photodiode arrays, each with 128 pixels, measuring 1.26, 1.27 and 1.53 µm. The measurement technique of the infrared imager is fundamentally different than that of the optical spectrograph; each pixel measures a line of sight at a particular altitude with a vertical resolution of approximately 1 km, creating an entire vertical profile spanning approximately 100 km with each exposure. As the satellite nods, the altitude range is then shifted. This provides a large increase in the amount of data compared to the OS, as each exposure creates a full profile, but also makes the IRI more susceptible to noise at higher altitudes, as exposure times are equal for all pixels. This also has a tendency to saturate pixels looking at low altitudes where the atmosphere is extremely bright. In addition, the wider

field of view and simple optical layout is more susceptible to contamination from stray light, which is addressed in Appendix A.

2.4 Radiative Transfer

Modelling of the scattered sunlight spectra is a complicated task and relies on solving the radiative transfer equation, which describes how light is scattered and absorbed as it moves through a medium (*Chandrasekhar*, 1960). While ultimately, it is photons incident on a detector which create a measurement, the design of an optical instrument makes the measured quantity much more limited, and thus much more useful in practice. Detectors have exposure times and finite areas, limiting the time frame and spacial extent to provide a measure of *irradiance*, expressed in units of J/cm^2/s. Of course, the energy of a photon is dictated by wavelength, and measurement systems can be constructed to measure this wavelength dependence of the irradiance through use of prisms or gratings, creating a measurement of *spectral irradiance*, in units of J/cm^2/s/nm. Typically, instruments observe incident light only in a defined direction, $\hat{\Omega}$, with an angular field of view, $d\hat{\Omega}$, distilling the quantity to *spectral radiance* with units of J/cm^2/s/nm/steradian. It is this quantity that OSIRIS measures and must therefore be modelled. While the measurement of spectral radiance is the integration of photons over small but discrete values determined by the optical system, the physical quantity of spectral radiance is a continuous property of position, $\vec{r}$, and propagation direction, $\hat{\Omega}$. If a detector is observing an object with area dA at an angle of θ with respect to the surface normal, than the spectral radiance of the surface is given by

$$I(\vec{r},\hat{\Omega}) = \frac{dE(\vec{r})}{dA\cos(\theta)\,dt\,d\lambda\,d\hat{\Omega}}. \tag{2.3}$$

This is subtly different than the measured spectral radiance which is an average of the true spectral radiance over the solid angle seen by the detector, or

$$I_{\text{meas}}(\vec{r},\hat{\Omega}) = \frac{\int_\Omega I(\vec{r},\hat{\Omega})d\hat{\Omega}}{\int_\Omega d\hat{\Omega}}. \tag{2.4}$$

While this distinction can be important, it is often unnecessary in practice, and quantities such as the spectral radiance are assumed to be constant over the limits of integration, as is the case for OSIRIS measurements, making $I_{\text{meas}}(\vec{r},\hat{\Omega}) = I(\vec{r},\hat{\Omega})$. As well, since optical instruments are typically sensitive to the number of photons rather than their energy it is customary in remote sensing to express spectral radiance in units of photons/cm^2/s/nm/steradian. Conversion to energy

is then straightforward through multiplication of the photon count by the energy of the photons at the wavelength measured.

It is useful here to introduce a coordinate system on which to base the following radiative transfer equations. Consider a ray, I, traveling with a propagation direction, $\hat{\Omega}$, along the path s. The ray will be said to originate at s_0, located at $\vec{r}_0$, as is shown in Figure 2.8. The position along the path, s, is then enough to fully determine both the position, $\vec{r}_0$, and the propagation direction, $\hat{\Omega}$.

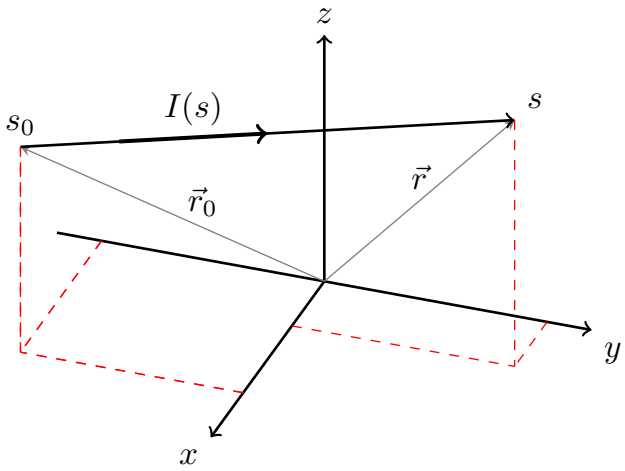

Figure 2.8: Coordinate system for light ray with spectral radiance I traveling along path s.

The fundamental building block of radiative transfer is the Beer-Lambert law, which describes how light is attenuated through an infinitesimally thin region of space, as shown in Figure 2.9.

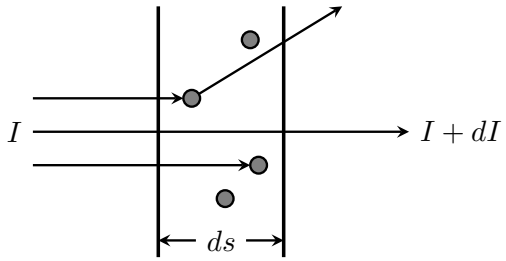

Figure 2.9: Attenuation of a light beam through an infinitesimally thin region of space.

As a monochromatic beam of light with radiance I enters a space with thickness ds, some photons in the beam will be either absorbed or scattered by particles in the space. This change in radiance of the beam, dI, is dictated by the number of particles, n, as well as the particle cross section, σ. If multiple types of particles are present in the space, then summing over all species, i,

in the region yields the Beer-Lambert law:

$$\frac{\mathrm{d}I(s)}{\mathrm{d}s} = -I(s)\sum_i \sigma_i n_i. \tag{2.5}$$

Solving yields the light intensity at any point along the path, s,

$$I(s) = I(s_0)e^{-\int_s \sum_i \sigma_i(s')n_i(s')ds'}, \tag{2.6}$$

with respect to the intensity at the reference point, s_0. The summation term is often referred to as extinction, k, defined as

$$k(s) = \sum_i \sigma_i(s)n_i(s). \tag{2.7}$$

When integrated over the path, s, this yields the optical depth, $\tau(s)$ and Equation 2.6 can be rewritten as

$$I(s) = I(s_0)e^{-\int_s k(s')ds'} = I(s_0)e^{-\tau(s)}. \tag{2.8}$$

The above formulation accounts for light that is removed from a beam due to scattering or absorption, but neglects light that has been scattered or emitted into the beam. This requires the inclusion of an additional source term, J, into Equation 2.5, and using the definition of extinction yields

$$\frac{\mathrm{d}I(s)}{\mathrm{d}s} = k(s)(J(s) - I(s)). \tag{2.9}$$

Contributions to the source term come from photochemical and blackbody emissions as well as scattered light. Blackbody radiation is negligible at visible and near infrared wavelengths in the sunlit atmosphere, so for wavelengths without significant photochemical emissions the source term is dominated by scattered light. The amount of light scattered into the direction of propagation, $\hat{\Omega}$, at point s, from the diffuse radiance is determined by the scattering cross section, number density of scatterers and the phase function along the path. Integration over all angles of the diffuse radiance, I_{diff}, then yields the total light scattered into the direction $\hat{\Omega}$

$$J(s,\hat{\Omega}) = \frac{k_{scat}(s)}{k(s)}\int_{4\pi} I_{diff}(s,\hat{\Omega}')\mathrm{p}(s,\Theta)d\hat{\Omega}'. \tag{2.10}$$

The phase function, $\mathrm{p}(s,\Theta)$, plays an important role and describes the angular distribution of scattered light; where Θ is the angle between the incoming and outgoing rays:

$$\cos(\Theta) = \hat{\Omega}\cdot\hat{\Omega}'. \tag{2.11}$$

The total radiance at a point s_1 is the summation of the attenuated source terms along the path, as well as the attenuated radiance from the beginning of the path at s_0

$$I(s_1) = I(s_0)e^{-\tau(s_0,s_1)} + \int_{s_0}^{s_1} k(s)J(s)e^{-\tau(s,s_1)}\mathrm{d}s. \tag{2.12}$$

The difficulty in solving this equation in the atmosphere comes from the computation of the diffuse radiance, $I_{diff}(s,\hat{\Omega})$, coming from each direction, since this requires solving the radiance equation at each point in the atmosphere.

2.4.1 SASKTRAN

SASKTRAN, developed at the University of Saskatchewan for OSIRIS data analysis (*Bourassa*, 2007), is a fully spherical, horizontally homogenous radiative transfer model. SASKTRAN solves Equation 2.12 by by breaking the radiance into successive orders of scattering, with the solar source term being traced through the atmosphere to generate the first order contribution, then scattered and attenuated through the atmosphere to generate the second, and so on. The first order is light that has been scattered only a single time from the solar beam, $F_0(\hat{\Omega}_0)$, either by the atmosphere or the Earth's surface. The single scatter source term due to atmospheric scattering, $J_1(s,\hat{\Omega})$, is found by attenuating the solar beam from the top of the atmosphere down to a point along path s. The amount scattered in the path direction, $\hat{\Omega}$ is then found by multiplying this term by the phase function, $\mathrm{p}(s,\Theta)$, yielding

$$J_1(s,\hat{\Omega}) = \frac{k_{scat}(s)}{k(s)}F_0(\hat{\Omega}_0)e^{-\tau(\mathrm{sun},s)}\mathrm{p}(s,\Theta). \tag{2.13}$$

The source term due to light that has been reflected off the Earth's surface requires an assumption about how the surface reflects light. Rough surfaces are often modelled as Lambertian, which states that the reflectance of a surface is proportional to the cosine of the angle from the surface normal and results in the brightness of a surface being independent of viewing angle. An observed radiance from a Lambertian surface, at location $\vec{r}$, is then

$$I(\vec{r}) = \frac{a}{\pi}F_{\mathrm{down}}(\vec{r},\theta). \tag{2.14}$$

where a is the albedo, the ratio of upwelling to downwelling radiative flux. The surface scattered source term, $\tilde{I}(s_0)$, is then given by

$$\tilde{I}_1(s_0) = \frac{a}{\pi}F_0(\hat{\Omega}_0)e^{-\tau(\mathrm{sun},s_0)}\cos(\theta_{sza}). \tag{2.15}$$

The cosine of the solar zenith angle is required to properly account for the decrease in flux due to light striking the surface at an angle. If the path does not intersect the ground then $\tilde{I}_1(s_0)$ is zero. These terms can then be substituted into Equation 2.12 and the radiance at point s_1 on the path, in the direction of $\hat{\Omega}$, due to a single scattered solar beam is given by

$$I_1(s_1, \hat{\Omega}) = \tilde{I}_1(s_0) e^{-\tau(s_0, s_1)} + \int_{s_0}^{s_1} k(s) J_1(s, \hat{\Omega}) e^{-\tau(s, s_1)} \mathrm{d}s. \tag{2.16}$$

Aside from the discretization of the atmosphere into homogenous spherical shells, no approximations are used for this calculation in SASKTRAN. The source term for light that is scattered two or more times is Equation 2.10 with the diffuse radiance found from the previous scattering calculation, yielding

$$J_i(s, \hat{\Omega}) = \frac{k_{scat}(s)}{k(s)} \int_{4\pi} I_{i-1}(s, \hat{\Omega}') \mathrm{p}(s, \Theta) d\Omega'. \tag{2.17}$$

The ground scattered component at point s_0 due to i scattering events can be calculated by integrating over all upward directions

$$\tilde{I}_i(s_0) = \frac{a}{\pi} \int_{2\pi} I_{i-1}(s_0, \hat{\Omega}') \cos(\theta') d\Omega'. \tag{2.18}$$

The radiance due to the i^{th} scattering event, at point s_1 and direction $\hat{\Omega}$ is then

$$I_i(s_1, \hat{\Omega}) = \tilde{I}_i(s_0) e^{-\tau(s_0, s_1)} + \int_{s_1}^{s_0} k(s) J_i(s, \hat{\Omega}) e^{-\tau(s, s_1)} \mathrm{d}s, \tag{2.19}$$

and the total radiance at s_1 in direction $\hat{\Omega}$ can then be determined by summing over all scattering events

$$I(s_1, \hat{\Omega}) = \left[\tilde{I}_1(s_0) + \sum_{i=2}^{\infty} \tilde{I}_i(s_0) \right] e^{-\tau(s_0, s_1)} + \int_{s_0}^{s_1} \left[J_1(s, \hat{\Omega}) + \sum_{i=2}^{\infty} J_i(s, \hat{\Omega}) \right] k(s) e^{-\tau(s, s_1)} \mathrm{d}s. \tag{2.20}$$

Second order scattering is treated in a similarly exact way with each single scattered ray being traced through the spherical atmosphere without approximation. For each point along the line of sight the incoming single scattered light is integrated and re-scattered. The integration and scattering requires angular discretization of the cell; however, incoming and outgoing resolutions need not be the same and optimization of these numerical quadratures is the focus of much work (*Wiensz et al.*, 2012). Higher order scattering contributes only a small component of the total signal, and so is approximated at all points along the line of sight (*Bourassa*, 2007). For these higher orders, the source terms, $I_{i-1}(s_1, \hat{\Omega})$, are calculated as an altitude profile for a variety of solar zenith angles. The source term's contributions which are scattered into the line of sight are then summed to yield the total contribution for the i^{th} scattering order.

The exact amount and direction that each cell attenuates and scatters light is dictated by the atmospheric constituents and concentrations. The SASKTRAN atmospheric model typically involves two main types of species: scatterers and absorbers. Absorbers are gases such as ozone and NO_2, which absorb light, but do not re-emit. The efficiency at which a gas absorbs light is often strongly wavelength dependent and is defined by the absorption cross section, σ_{abs}. These can be calculated using quantum mechanics, but are typically experimentally determined, as is the case for absorbers used in SASKTRAN.

Scattering particles can be further broken into two groups, the molecular atmosphere and aerosols. Lord Rayleigh was the first to calculate scattering from the molecular atmosphere by treating the molecules as dielectric spheres, with a radius much smaller than the wavelength of light. This results in a molecular scattering cross section, σ_{Ray}, that is highly wavelength dependent and given by the equation

$$\sigma_{\text{Ray}} = \frac{128\pi^5\alpha_0^2(6+3\rho_n)}{3\lambda^4(6-7\rho_n)}, \tag{2.21}$$

where α_0 and ρ_n are the volume polarizability and depolarization factors respectively. The phase function for a molecular scatterer is relatively flat and symmetric about a scattering angle of 90°,

$$\text{p}_{\text{Ray}}(\Theta) = \frac{3}{4}(1+\cos^2(\Theta)). \tag{2.22}$$

Aerosol particles are much larger, on the same order of magnitude as the wavelength of visible light, so the small sphere approximation no longer holds and a more rigorous solution to Maxwell's equations is needed. Mie formulated a solution for this general case of electromagnetic scattering by a sphere which takes the form of an infinite series of spherical Bessel and Hankel functions (*Mie*, 1908). While computationally complex, significant work has been done to implement efficient numerical solutions, of which the *Wiscombe* (1980) code has become widely used and is implemented in SASKTRAN. Since aerosols are a collection of particles, a distribution function describing the size is needed. In SASKTRAN unimodal lognormal distributions, as given by Equation 2.1, are typically used for stratospheric aerosols. Calculations of relevant properties such as the total aerosol phase function, $\bar{\text{p}}_{\text{aer}}(\Theta)$, then require an integration over all particle sizes (*Hansen and Travis*, 1974):

$$\bar{\text{p}}_{\text{aer}}(\Theta) = \frac{1}{n_{\text{aer}}}\int_0^\infty \text{p}_{\text{aer}}(\Theta, r)\frac{dn(r)}{dr}dr. \tag{2.23}$$

2.5 Measurement Inversion

Satellites monitor the atmospheric state indirectly and require the process in question to be modelled so the measurement can be converted to a physical quantity. This is called measurement inversion and is typically done through the construction of a measurement vector, $\mathbf{y}$, from a set of spectral radiances that maximizes the sensitivity to a desired quantity while minimizing the sensitivity to other parameters. A model, $\mathbf{F}$, with input states described by $\tilde{\mathbf{b}}$ and the specific desired parameter, $\mathbf{x}$, is then used to calculate, or "forward model", the measurement vector. Vectors $\mathbf{x}$ and $\mathbf{y}$ have lengths n and m respectively, with each element describing a value at a particular altitude. Solving for the state vector, $\mathbf{x}$, then requires inverting the equation:

$$\mathbf{y} = \mathbf{F}(\mathbf{x}, \tilde{\mathbf{b}}) + \boldsymbol{\epsilon} \tag{2.24}$$

where $\boldsymbol{\epsilon}$ is the measurement error. For a linear model with no error this can be solved directly using an *a priori* state, or initial guess, $\mathbf{x_a}$, to determine the retrieved state $\hat{\mathbf{x}}$:

$$\mathbf{y} = \mathbf{K}(\mathbf{x} - \mathbf{x}_a) + \mathbf{F}(\mathbf{x_a}, \tilde{\mathbf{b}}), \tag{2.25}$$

$$\hat{\mathbf{x}} = \mathbf{x}_a + \mathbf{K}^{-1}\left(\mathbf{y} - \mathbf{F}(\mathbf{x}_a, \tilde{\mathbf{b}})\right), \tag{2.26}$$

where $\mathbf{K}$ is the Jacobian matrix

$$\mathbf{K} = \begin{pmatrix} \frac{\partial F_1}{\partial x_1} & \cdots & \frac{\partial F_1}{\partial x_n} \\ \vdots & \ddots & \vdots \\ \frac{\partial F_m}{\partial x_1} & \cdots & \frac{\partial F_m}{\partial x_n} \end{pmatrix}. \tag{2.27}$$

However, satellite measurements are typically non-linear, with the forward model and the Jacobian relying on numerical approximations. Because of this non-linearity the above approach is often inapplicable and an iterative approach is adopted. Although solving non-linear problems is an active field, a few of the more widely used methods are discussed below.

2.5.1 Optimal Estimation

Optimal estimation is a standard and often used method of updating the atmospheric state based on a Bayesian approach to knowledge of the *a priori* information and a current measurement with some amount of error (*Rodgers*, 2000, chap. 2.3.2). The probability of the atmospheric state being $\mathbf{x}$ given the measurement $\mathbf{y}$ is

$$P(\mathbf{x}|\mathbf{y}) = \frac{P(\mathbf{y}|\mathbf{x})P(\mathbf{x})}{P(\mathbf{y})}. \tag{2.28}$$

If the *a priori* atmospheric state and measurement error are both assumed to have Gaussian probability distributions then $P(\mathbf{y}|\mathbf{x})$ and $P(\mathbf{x})$ can be expressed as

$$-2\ln P(\mathbf{y}|\mathbf{x}) = (\mathbf{y}-\mathbf{K}\mathbf{x})^{\mathrm{T}}\mathbf{S}_{\epsilon}^{-1}(\mathbf{y}-\mathbf{K}\mathbf{x}) + c_1 \tag{2.29}$$

$$-2\ln P(\mathbf{x}) = (\mathbf{x}-\mathbf{x}_a)^{\mathrm{T}}\mathbf{S}_{a}^{-1}(\mathbf{x}-\mathbf{x}_a) + c_2, \tag{2.30}$$

where $\mathbf{S}_{\epsilon}$ and $\mathbf{S}_a$ are the covariance matrices for the measurement error and *a priori* atmospheric state, respectively. Substitution into Equation 2.28 and equating like terms yields the retrieved atmospheric state

$$\hat{\mathbf{x}} = \mathbf{x}_a + \mathbf{S}_a\mathbf{K}^{\mathrm{T}}\left(\mathbf{K}\mathbf{S}_a\mathbf{K}^{\mathrm{T}} + \mathbf{S}_{\epsilon}\right)^{-1}(\mathbf{y}-\mathbf{K}\mathbf{x}_a). \tag{2.31}$$

For non-linear problems this process can be iterated until a solution is converged upon.

A primary limitation of this method is the assumption that the knowledge of the *a priori* atmospheric state is accurately modelled with a Gaussian probability distribution. If this is not the case, or the *a priori* parameters are inaccurate, then the retrieved atmospheric state will be biased by this uncertainty, particularly in the case of noisy measurements. While this technique is not used in this work, it is included for completeness due to the common use in the field.

2.5.2 Multiplicative Algebraic Reconstruction Technique

The Multiplicative Algebraic Reconstruction Technique (MART), initially developed to deblur Fabry-Perot images (*Lloyd and Llewellyn*, 1989), is a computationally efficient method of updating the atmospheric state, $\mathbf{x}$, based on a ratio of the model, $\mathbf{F}(\mathbf{x},\tilde{\mathbf{b}})$ to the measurement, $\mathbf{y}$. Similar to Chahine relaxation (*Chahine*, 1970, 1972) with an added weighting matrix, $\mathbf{W}$, MART allows multiple measurement vectors to be used in the determination of each species concentration. The weighting matrix defines the contribution of each measurement vector, k, and tangent altitude, j, to the retrieved altitude, i, based on relative path lengths through the atmosphere and the sensitivity of the measurement vectors at that altitude

$$\hat{x}_i^{(n+1)} = \hat{x}_i^{(n)} \sum_k \sum_j \frac{y_{jk}}{F_{jk}\left(\mathbf{x}^{(n)},\tilde{\mathbf{b}}\right)} W_{ijk}. \tag{2.32}$$

This technique has the advantage of not requiring the Jacobian to be calculated or inverted, a computationally expensive task for a limb measurement. Note that the sensitivity of the measurement vector to the state parameter must be positive. However, for typical retrieval scenarios, the measurement vector can be constructed to ensure positivity making MART a fast and effective retrieval technique.

2.5.3 Levenberg-Marquardt

One the more classical approaches to non-linear problems is the Gauss-Newton method which aims to minimize a residual, S, which is the sum of squared difference between a model, $\mathbf{F}(\mathbf{x}, \tilde{\mathbf{b}})$ and set of measurements, $\mathbf{y}$:

$$S(\mathbf{x}) = \sum_i \left(y_i - \mathbf{F}(\mathbf{x}, \tilde{\mathbf{b}}) \right)^2. \tag{2.33}$$

If the atmospheric state, $\mathbf{x}$ is perturbed by an amount, $\boldsymbol{\delta}$, then Taylor expansion yields

$$S(\mathbf{x} + \boldsymbol{\delta}) \approx S(\mathbf{x}) + \nabla S(\mathbf{x})\boldsymbol{\delta} + \frac{1}{2}\boldsymbol{\delta}^{\mathrm{T}}\mathbf{H}(S(\mathbf{x}))\boldsymbol{\delta}, \tag{2.34}$$

where $\mathbf{H}(S(\mathbf{x}))$ is the Hessian matrix of $S(\mathbf{x})$. The gradient of $S(\mathbf{x})$ can be rewritten in terms of the Jacobian, $\mathbf{K}$ as

$$\nabla S(\mathbf{x}) = -2\mathbf{K}^{\mathrm{T}} \left[\mathbf{y} - \mathbf{F}(\mathbf{x}, \tilde{\mathbf{b}}) \right]. \tag{2.35}$$

The Hessian is the matrix of second order partial derivatives, with one element given by

$$H_{ij}(S(\mathbf{x})) = 2\sum_k \frac{\partial F_k(\mathbf{x}, \tilde{\mathbf{b}})}{\partial x_i} \frac{\partial F_k(\mathbf{x}, \tilde{\mathbf{b}})}{\partial x_j} + 2\sum_k \left[y_k - F_k(\mathbf{x}, \tilde{\mathbf{b}}) \right] \frac{\partial^2 F_k(\mathbf{x}, \tilde{\mathbf{b}})}{\partial x_i \partial x_j} \tag{2.36}$$

If the second derivative is assumed to be small, the Hessian matrix can be approximated using

$$\mathbf{H}(S(\mathbf{x})) \approx 2\mathbf{K}^{\mathrm{T}}\mathbf{K}, \tag{2.37}$$

simplifying Equation 2.34 to:

$$S(\mathbf{x} + \boldsymbol{\delta}) \approx S(\mathbf{x}) - 2\mathbf{K}^{\mathrm{T}} \left[\mathbf{y} - \mathbf{F}(\mathbf{x}, \tilde{\mathbf{b}}) \right] \boldsymbol{\delta} + \boldsymbol{\delta}^{\mathrm{T}}\mathbf{K}^{\mathrm{T}}\mathbf{K}\boldsymbol{\delta}. \tag{2.38}$$

Differentiating with respect to $\boldsymbol{\delta}$, and equating to zero then gives the perturbation which minimizes S, producing the classic Gauss-Newton algorithm

$$\mathbf{K}^{\mathrm{T}}\mathbf{K}\boldsymbol{\delta} = \mathbf{K}^{\mathrm{T}} \left[\mathbf{y} - \mathbf{F}(\mathbf{x}, \tilde{\mathbf{b}}) \right]. \tag{2.39}$$

This is a powerful result, often producing fast convergence, even for non-linear problems. From this derivation, however, it is clear that the limitations lie in limited Taylor expansion, and more immediately in the approximated Hessian. If the second derivative terms are not small, i.e., the problem is more than quadratic, this assumption is violated and convergence may fail.

A different technique, often called gradient descent uses the intuitive approach of moving along the solution space in the direction of steepest descent. Choosing a step size, γ', such that the residual, $S(\mathbf{x})$, is reduced leads to the algorithm

$$\boldsymbol{\delta} = -\gamma' \nabla S(\mathbf{x}) = 2\gamma' \mathbf{K}^{\mathrm{T}} \left[\mathbf{y} - \mathbf{F}(\mathbf{x}, \tilde{b}) \right]. \tag{2.40}$$

Choosing the optimal γ' such that $S(\mathbf{x})$ is reduced is not trivial, with over estimations causing iterations to be thrown out and underestimations limiting the step size unnecessarily. Even with an ideal γ' however, because second derivatives are not computed even approximately, this method can converge very slowly for certain types of problems.

Levenberg sought to combine the fast convergence of Gauss-Newton with the robustness of gradient descent by merging the methods and taking a step that is a compromise between the two (*Levenberg*, 1944). This was accomplished by adding a diagonal matrix to $\mathbf{K}^{\mathrm{T}}\mathbf{K}$, such that the Gauss-Newton step is damped, resulting in

$$\left(\mathbf{K}^{\mathrm{T}}\mathbf{K} + \gamma\mathbf{I}\right)\boldsymbol{\delta} = \mathbf{K}^{\mathrm{T}}\left(\mathbf{y} - \mathbf{F}(\mathbf{x}, \tilde{\mathbf{b}})\right). \tag{2.41}$$

If γ is chosen to be small the method approaches that of Gauss-Newton, while if large, a step is taken in the direction of gradient descent, although heavily damped. Proper choice of γ then allows the step to be taken as large as possible while staying within an approximately linear region. The downside to this technique is that if γ is large very small steps will be taken along directions of small gradients, leading to the same problems as simple gradient descent methods. *Marquardt* (1963) noted that by replacing $\mathbf{I}$ with the diagonal elements of the approximate Hessian this problem could be avoided, with larger steps being taken along directions of small gradients, leading to the Levenberg-Marquardt algorithm

$$\left(\mathbf{K}^{\mathrm{T}}\mathbf{K} + \gamma\mathrm{diag}(\mathbf{K}^{\mathrm{T}}\mathbf{K})\right)\boldsymbol{\delta} = \mathbf{K}^{\mathrm{T}}\left(\mathbf{y} - \mathbf{F}(\mathbf{x}, \tilde{\mathbf{b}})\right). \tag{2.42}$$

With this, the next iteration of the atmospheric state is

$$\hat{\mathbf{x}}^{(n+1)} = \hat{\mathbf{x}}^{(n)} + \boldsymbol{\delta}. \tag{2.43}$$

Determination of the optimal damping factor, γ, can be found by a numerical search for each choice of model parameters; ultimately, this requires calculating the forward model for each guess, so quickly becomes prohibitive. For efficiency more ad hoc methods of determining γ are often used. *Rodgers* (2000, chap. 5.7), recommends a damping factor proportional to the non-linearity of the solution space at the location being tested. This ensures that the next guess is always taken within an approximately linear range and guarantees a reduction in the residual.

2.6 OSIRIS Aerosol Extinction Retrieval

The stratospheric aerosol extinction coefficient, which is currently retrieved as part of the standard OSIRIS data processing, uses an assumed unimodal lognormal particle size distribution with a

mode radius of 0.08 µm and mode width of 1.6, as these are typical of the background aerosol loading conditions (*Deshler et al.*, 2003). The scattering cross sections and phase functions are then calculated using Mie theory, and aerosol number density is retrieved using a single measurement vector based on the ratio of spectral radiances at two wavelengths

$$\tilde{I}(j) = \frac{I(j, 750\,\mathrm{nm})}{I(j, 470\,\mathrm{nm})}. \tag{2.44}$$

This normalization is used to reduce the effect of local density fluctuations in the neutral background, that would otherwise be fit with the aerosol concentration, and to increase sensitivity to the Mie scattering signal (*Bourassa et al.*, 2007). To further increase the sensitivity to aerosol the measurement is normalized by a modelled Rayleigh signal, $\tilde{I}_{\mathrm{Ray}}(j)$, yielding

$$y_j = \ln\left(\frac{\tilde{I}(j)}{\tilde{I}_{\mathrm{Ray}}(j)}\right). \tag{2.45}$$

Finally, the measurement vector is normalized by one or more high altitude measurements. This eliminates the need for an absolute calibration and decreases the sensitivity to unknown surface albedo and tropospheric clouds (*von Savigny et al.*, 2003). To improve the signal to noise of normalizing by a single high altitude measurement, normalization is chosen over an altitude range such that Equation 2.45 is at a minimum within a noise margin of 0.01 (*Bourassa et al.*, 2011) . This provides the final aerosol measurement vector

$$y_j = \ln\left(\frac{\tilde{I}(j)}{\tilde{I}_{\mathrm{Ray}}(j)}\right) - \frac{1}{N}\sum_{j=m}^{m+N} \ln\left(\frac{\tilde{I}(j)}{\tilde{I}_{\mathrm{Ray}}(j)}\right), \tag{2.46}$$

where N tangent altitudes between m and $m+N$ have been used for the normalization.

Since only one measurement vector is used this simplifies the MART equation to

$$\hat{x}_i^{(n+1)} = \hat{x}_i^{(n)} \sum_j \frac{y_j}{F_j\left(\mathbf{x}^{(n)}, \tilde{\mathbf{b}}\right)} W_{ij}. \tag{2.47}$$

Here the weighting matrix, W, provides the contribution of various lines of sight at tangent altitudes, j, to the retrieved altitude, i, based on relative path lengths of the line of sight through the spherical shells. Equation 2.47 is then used with the SASKTRAN model to iteratively calculate the aerosol number density.

The problem with this approach is that the measurement vector, y_{aer}, is approximately proportional to $n_{\mathrm{aer}}\bar{\sigma}_{\mathrm{aer}}\bar{\mathrm{p}}_{\mathrm{aer}}(\Theta)$, as shown in detail in Chapter 4, resulting in any error in $\bar{\sigma}_{\mathrm{aer}}$ or $\bar{\mathrm{p}}_{\mathrm{aer}}(\Theta)$ being translated to the retrieved quantity n_{aer}. To minimize this effect the aerosol number density

is converted to extinction for the final product using the relationship $k_{\mathrm{aer}} = n_{\mathrm{aer}}\bar{\sigma}_{\mathrm{aer}}$, as it has a smaller dependence on the assumed particle size (*McLinden et al.*, 1999). The phase function must still be assumed however, and the error resulting from this is explored in the following chapter.

Chapter 3

The Particle Size Problem

Enhancements to the background stratospheric aerosol layer are highly variable, with volcanoes such as El Chichon and Mt. Pinatubo increasing the total aerosol load by an order of magnitude or more (*McCormick et al.*, 1995). These enhancements also change the particle size distribution, with larger aerosol loadings typically having larger particles (*Bauman et al.*, 2003). While the last major eruption was Mt. Pinatubo in 1991, several smaller eruptions have since occurred and their impact on stratospheric aerosols can clearly be seen in the satellite measurements. Figure 1 from *Vernier et al.* (2011), reproduced below as Figure 3.1, shows the extinction ratio at 525 nm as measured by the SAGE II and CALIPSO missions. Extinction ratio is the ratio of extinction due to aerosol to the molecular extinction and is analogous to volume mixing ratio. Although El Chichon erupted in 1982, three years prior to the start of the SAGE II measurements, the early years are still dominated by the El Chichon and Mt. Pinatubo (Pi) eruptions, with aerosol levels only returning to background conditions after approximately 1997. This quiescence lasts until 2005 at which time aerosol enhancements from smaller volcanoes such as Mt. Manam (Ma), Soufriére Hills (So) and Tavurvur (Ta) can be seen. The long timescale of volcanic aerosols is also visible, with particles typically taking more than a year to propagate upward through the stratosphere.

Due to the highly variable nature of stratospheric aerosols during volcanically active times, it draws into question the validity of assuming a constant unimodal lognormal particle size distribution. This can be tested by comparing data taken at similar locations and times, but with different viewing geometries. If the particle size, and thus the phase function is correct, then measurements will be independent of the scattering angle. If, on the other hand, particle size has been incorrectly assumed, the phase function will be wrong, and the retrieval will compensate with differing amounts of aerosol depending upon the on scattering angle. This can be examined by exploiting the geometry of the Odin orbit and comparing matching pairs of scans.

To reduce the noise involved in a single measurement pair a comparison of ascending and descending node measurements was done using daily zonal averages for 20°N to 20°S. In Figure 3.2 the

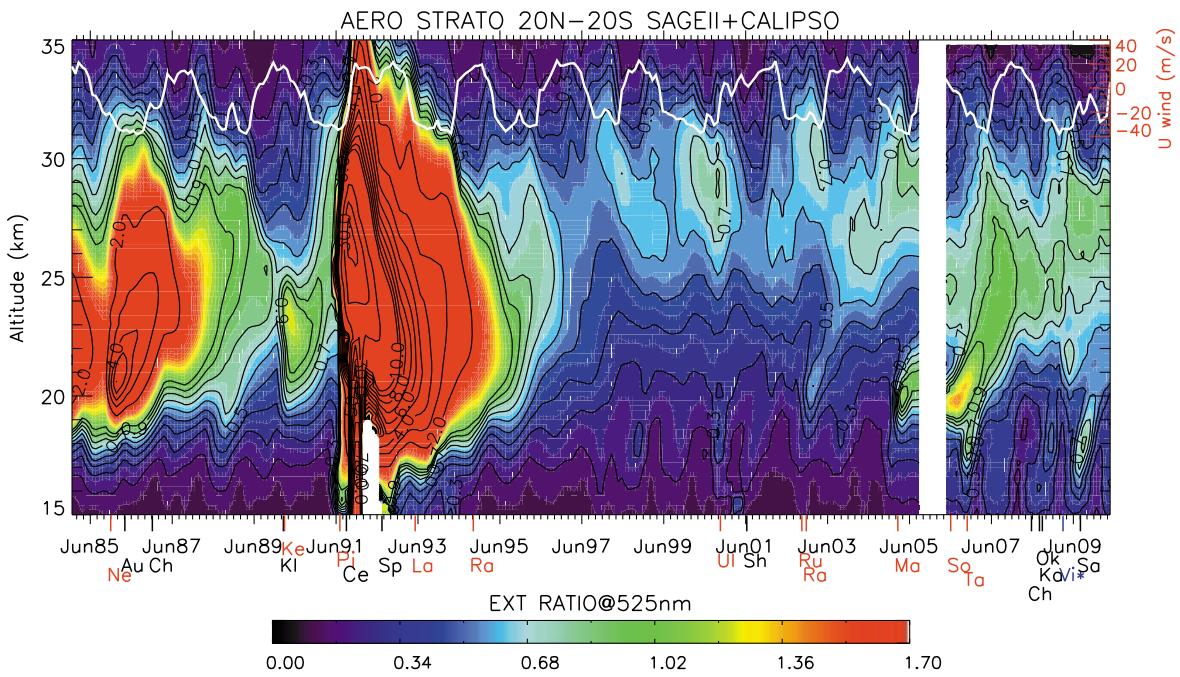

Figure 3.1: Monthly mean aerosol extinction ratio (525 nm) in the tropics (20°N to 20°S) from January 1985 to June 2010. Data is from the SAGE II (1985-2005) and CALIPSO (2006-2010) missions. Shown in white is the Singapore zonal wind component at 10hPa. Figure 1 from *Vernier et al.* (2011) reproduced by permission of American Geophysical Union.

ascending and descending node scattering angles are shown in orange and red, and the daily aerosol extinction ratios averaged between 25 and 28 km are shown in green and blue for the respective nodes. As the OSIRIS orbit precesses the ascending node equatorial crossing time becomes later in the evening, and the tangent point zenith angle increases, eventually exceeding 90° and limiting the aerosol retrievals to a single geometry in the tropics. Although this limits the comparison during the later years, it is clear that there is a systematic difference in retrieved aerosol based on the viewing geometry even for the earlier years, indicating that the phase function and hence assumed particle size distribution is likely incorrect.

It is worth clarifying here that there are two possible physical reasons to see systematic shifts in the data; yearly cycles in the aerosol layer which may happen to coincide with the Odin orbit, and daily cycles which may present as a shift in the ascending/descending node measurements. The effect of yearly cycles is removed by comparing the ascending and descending node measurements on a daily basis. Daily cycles, while possible, are not expected to be measurable due to the long time scales of aerosol variability. This is confirmed by comparing daily measurements of different nodes which have similar scattering angles, as occurs twice per year near the equinoxes. Here we see little

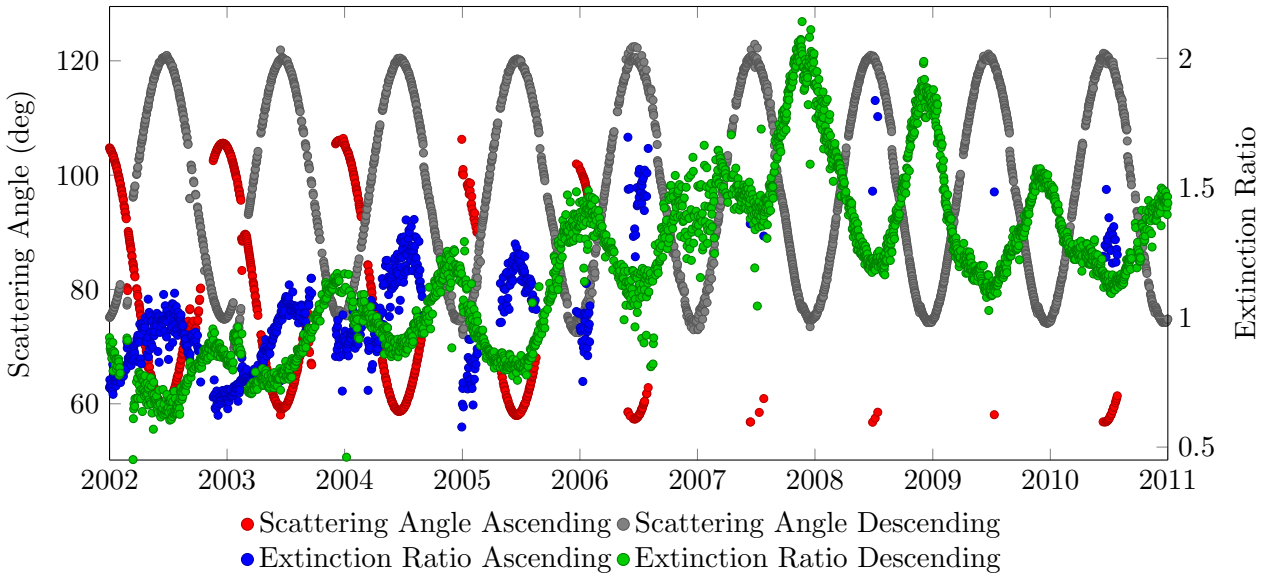

Figure 3.2: Comparison of daily ascending and descending node aerosol measurements in the tropics between 23 and 28 km altitude (20°N to 20°S).

to no difference in the measurements of the two nodes despite a 12 hour difference in measurement time, confirming the bias is due primarily to particle size assumptions and not physical variation.

3.1 Effect of Particle Size on OSIRIS Retrievals

From the above analysis it is clear that a systematic error is present due to the incorrect assumption on particle size. Unfortunately, quantitative analysis of the effect is more difficult, primarily due to the lack of large scale aerosol measurements with which to compare against. Figure 3.3, also from *Vernier et al.* (2011), shows a qualitative comparison between the OSIRIS and SAGE II/CALIPSO data from 2002 to 2010. In general, agreement is excellent, particularly for the early years of the mission with low aerosol loading. Systematic differences are also apparent after the Soufriére Hills eruption in 2006. Past this time OSIRIS measures increases in the aerosol extinction ratio near the end of each year; increases that are not seen in the CALIPSO data. However, since these instruments measure extinction at different wavelengths than OSIRIS, it is difficult to quantify the error due to particle size; for this it is best to compare against an instrument with a more similar wavelength.

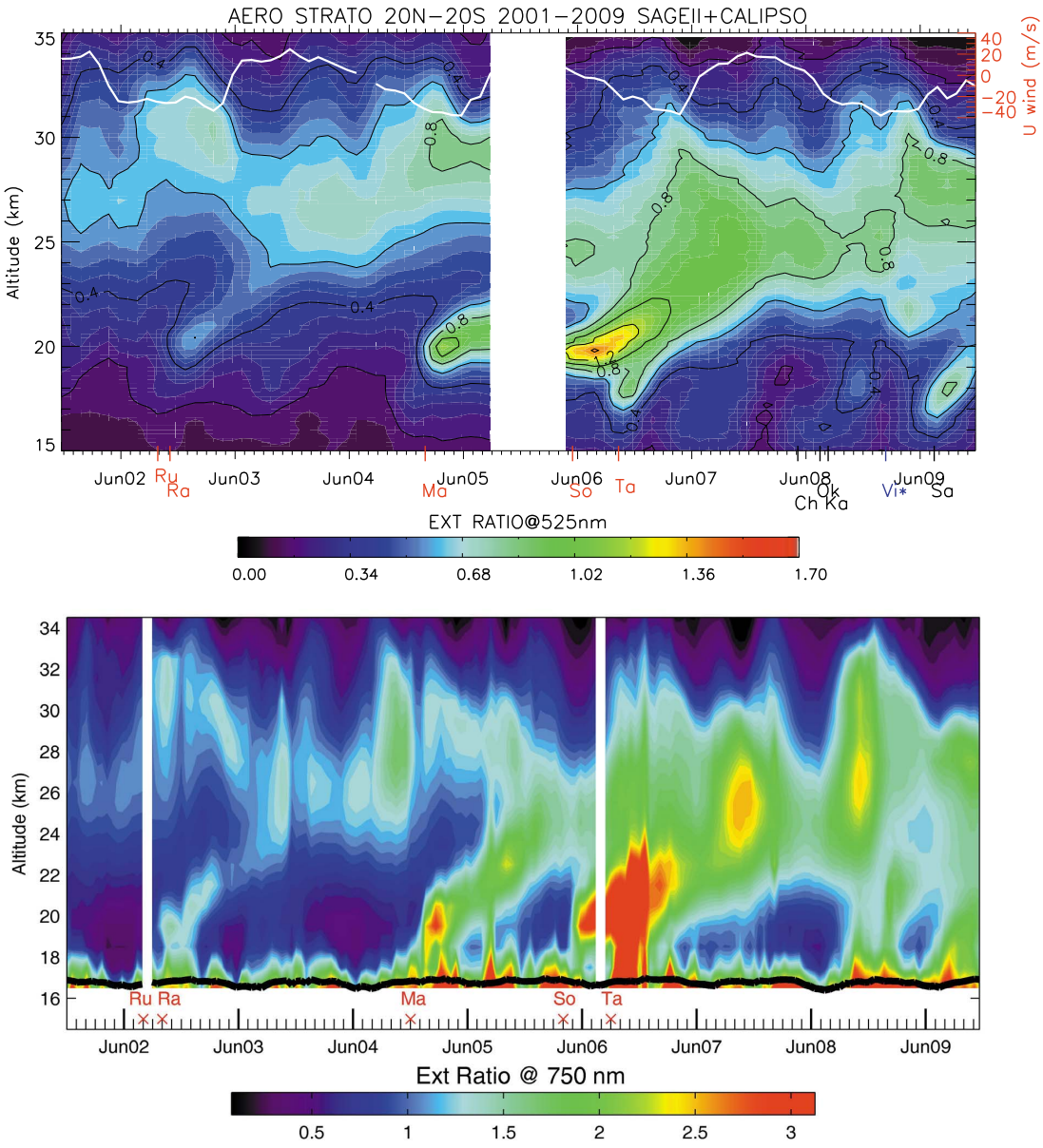

Figure 3.3: Comparison of the OSIRIS and SAGE II/CALIPSO monthly extinction ratio measurements. Figure 2 from *Vernier et al.* (2011) reproduced by permission of American Geophysical Union.

3.1.1 SAGE III Comparison

In operation from 2001 until 2005, SAGE III measured aerosol extinction profiles at nine wavelengths, ranging from 385 nm to 1.54 µm. SAGE III was launched on the Meteor 3M platform into a polar orbit, performing occultations in the mid to polar latitudes. With an accuracy and precision on the order of 10%, and a channel at 755 nm, SAGE III provides an excellent data set for comparison (*Thomason et al.*, 2010). Figure 3.4 shows the percent difference (solid) and standard deviation (dotted) between the SAGE III 755 nm and OSIRIS 750 nm extinction measurements that were within 6 hours, 1° latitude and 2.5° longitude. While agreement between the two data sets is generally excellent, all years show a positive bias below approximately 17 km. As well, nearly all altitudes in 2005 show a positive bias with an increased standard deviation. This is well explained by an inaccurate particle size assumption, which may not be accurate at low altitudes and during the increased aerosol loading after the 2004 Mt. Manam eruption. This comparison suggests an average extinction bias of approximately 10% due to particle size in 2005, although this error likely increases in later years as volcanogenic aerosols become more prominent. In addition, the good agreement suggests that while error due to particle size may be present from 2002-2004, the systematic error is small, and the true extinction lies between the extremes retrieved by OSIRIS.

3.2 Particle Size Measurements

The solution to the particle size problem is to measure the particle size more accurately using the OSIRIS measurements, or incorporate measurements from other systems to improve the size distribution used in the retrievals. Unfortunately, comprehensive stratospheric aerosol particle size measurements do not exist for the duration of the OSIRIS mission, and indeed this lack of measurement is a large driver of this work, making the direct retrieval of particle size the foremost option. Although comprehensive particle size data sets do not exist, aerosol particle size has certainly been measured before, both directly using balloon-borne instruments (*Renard et al.*, 2005; *Deshler et al.*, 2003) and remotely using ground based LIDARs (*Wandinger et al.*, 1995; *Müller et al.*, 1999; *Jumelet et al.*, 2008). Some satellites have also had the ability to retrieve particle size and we first look to these methods for solutions to the particle size dilemma.

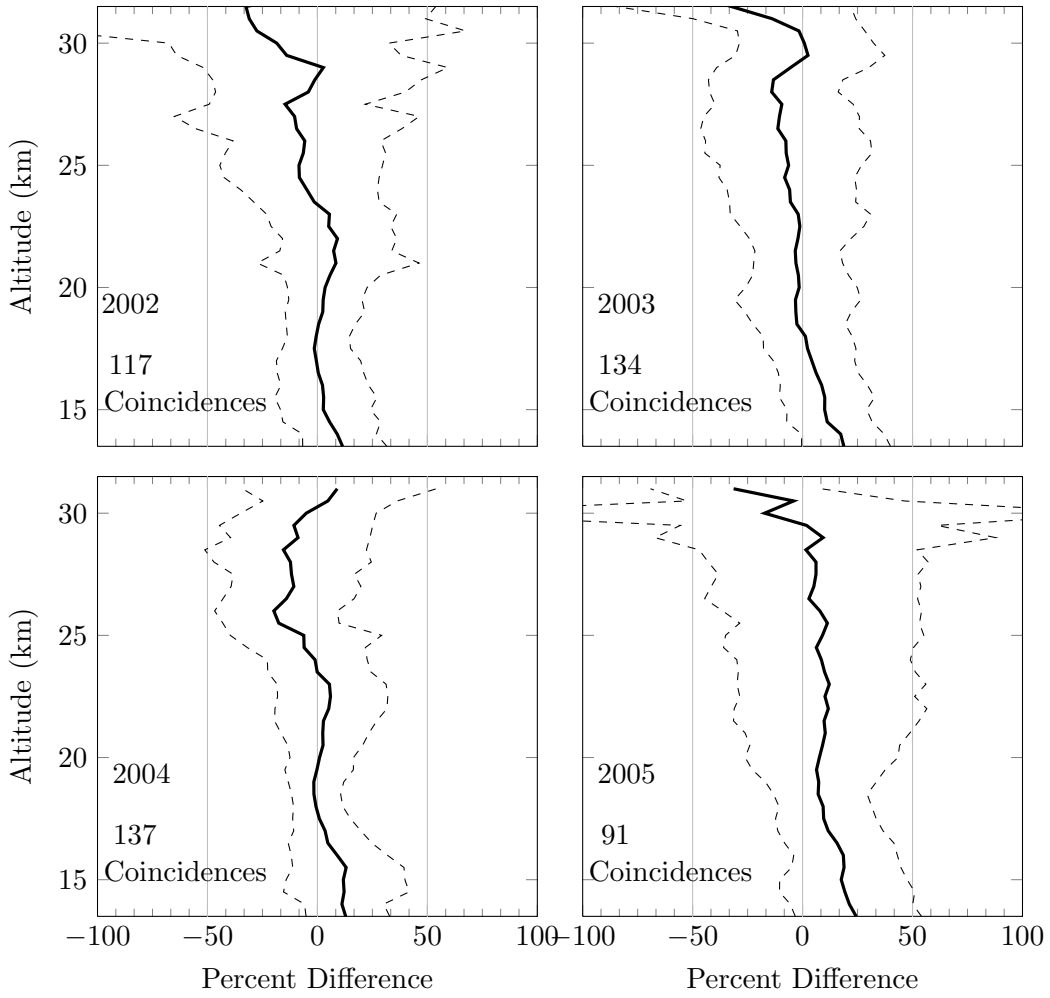

Figure 3.4: Comparison of SAGE III and OSIRIS aerosol retrievals for yearly coincident measurements. Percent difference shown as black line, standard deviation shown as gray lines.

3.2.1 Solar Mesosphere Explorer

One of the first satellites to measure stratospheric aerosol particle size was the Solar Mesosphere Explorer (SME) launched in 1981 (*Barth et al.*, 1983). Designed to monitor ozone in the mesosphere, SME was equipped with four limb scanning instruments including an infrared radiometer and a near infrared spectrometer. By spinning the satellite at 5 rpm on an axis perpendicular to the orbital plane these instruments measured vertical profiles at 1.27, 1.86 and 6.8 µm every 12 seconds. Aerosol retrievals were first performed by *Thomas et al.* (1983) by assuming the scattering contribution to the radiance measurements at 6.8µm was negligible, simplifying the radiative transfer equation to

$$I(\lambda = 6.8\mu m) = \int_{s_0}^{s_1} B(T(s))[k_{H_2O}(s) + k_{\text{aer}}(s)] \exp(-\tau(s, s_1))ds, \tag{3.1}$$

where $B(T(s))$ is the Planck function at the atmospheric temperature T at position s along the line of sight. If the amount of water vapour in the atmosphere is known, k_{H_2O} can then be calculated and k_{aer} retrieved. It was further noted that the extinction cross section of aerosol particles at 6.8 µm was approximately proportional to the cube of the particle radius. This allowed for conversion from aerosol optical depth, τ_{aer}, to aerosol column mass, M_{aer}, by combining the equations:

$$\tau_{\text{aer}} = \int_{s_0}^{s_1} \int_0^{\infty} C_1 r^3 \frac{dn(r)}{dr} dr ds \tag{3.2}$$

$$M_{\text{aer}} = \int_{s_0}^{s_1} \int_0^{\infty} \frac{4}{3} \pi \rho r^3 \frac{dn(r)}{dr} dr ds \tag{3.3}$$

to obtain

$$M_{\text{aer}} = C_2 \tau_{\text{aer}}. \tag{3.4}$$

The constant, C_2, was estimated to be 6.3 g/m^2 using an approximate particle size distribution, but is actually independent of the distribution shape provided the total number of particles remains unchanged. *Eparvier et al.* (1994) extended this column mass technique to include particle size by incorporating the 1.27 and 1.86 µm channels. Radiance measurements at 1.27 and 1.86 µm were averaged into weekly 5° latitude bins, and based on the mass density from the 6.8 µm channel, were compared to modelled values for a range of unimodal lognormal distributions. Least squares fitting of the measured and modelled radiances then yielded the mode radius and mode width size parameters. Results from this technique compare well to LIDAR observations made at Mauna Loa, Hawaii (*Dutton et al.*, 1994), but fundamentally rely on a "known" aerosol mass derived from infrared radiometer data.

3.2.2 SAGE II

A second satellite data set which has been used numerous times to derive stratospheric aerosol particle size is that of SAGE II. Occultation measurements are accurately modelled considering only an extinction term, without the need to consider scattering. This simplifies the radiative transfer equation to

$$I(\lambda) = I_{exo}(\lambda) \exp\left(\int_{s_0}^{s_1} k(\lambda, s) ds \right) \tag{3.5}$$

which, if the extinction due to other species is known, makes retrieval of k_{aer} straightforward. This provides excellent quality aerosol extinction measurements that are independent of particle size, and in the case of SAGE II at wavelengths of 385, 453, 525 and 1020 nm. Since $k_{\text{aer}} = n_{\text{aer}} \sigma_{\text{aer}}$ and n_{aer} is independent of wavelength, the change in extinction as a function of wavelength is dictated entirely

by the particle size distribution. The ratio, $k_{\rm aer}(\lambda_i)/k_{\rm aer}(\lambda_{\rm ref})$ then eliminates number density and is an indirect measurement of particle size. *Yue et al.* (1986) exploited this fact to derive unimodal lognormal particle size distributions from the SAGE II extinction measurements. This was done by combining the equations:

$$R_1 = \frac{k_{\rm aer}(\lambda = 385\,{\rm nm})}{k_{\rm aer}(\lambda = 1020\,{\rm nm})} = f_1(r_g, \sigma_g) \tag{3.6}$$

$$R_2 = \frac{k_{\rm aer}(\lambda = 525\,{\rm nm})}{k_{\rm aer}(\lambda = 1020\,{\rm nm})} = f_2(r_g, \sigma_g) \tag{3.7}$$

and using Mie theory to find r_g and σ_g which satisfy the measurement ratios R_1 and R_2. The problem with this approach is that quantities such as total particle number and mean radius are highly sensitive to the tails of the size distribution. *Thomason and Poole* (1992) found that other parameters such as total aerosol volume and surface area were much less sensitive to assumptions about the size distribution, and used principal component analysis to derive surface area density from the four extinction measurements.

Principal Component Analysis (PCA) was originally developed by *Pearson* (1901) as a method of deriving best fit parameters to multivariate data. He noted that in real-world situations, treating one variable as dependent and others as independent can be problematic and that the errors should be minimized for all parameters, not only the dependent one. This results in a minimization of perpendicular distances between the data and the linear model, creating the smallest possible variance from the best fit. PCA is then performed by determining the directions, or principal components, which maximize the variance and therefore leave the smallest amount unaccounted for after fitting. This is accomplished by first determining the covariance matrix, $\mathbf{C}$, of a data set, $\mathbf{X}$, which has zero mean. The eigenvectors, $\mathbf{u}$, of the covariance matrix are then arranged in the matrix $\mathbf{U}$ as

$$\mathbf{U} = (\mathbf{u}_1, \mathbf{u}_2, \cdots, \mathbf{u}_n)\,. \tag{3.8}$$

Similarly, the corresponding eigenvalues, l, are arranged in the diagonal matrix, $\mathbf{L}$

$$\mathbf{L} = \begin{pmatrix} l_1 & \cdots & 0 \\ \vdots & \ddots & \vdots \\ 0 & \cdots & l_n \end{pmatrix}. \tag{3.9}$$

The eigenvectors provide the components in which variance is maximized, while the eigenvalues provide the magnitude of the variance for that component. Transformation of the data, $\mathbf{X}$ into the coordinate system defined by $\mathbf{U}$, then provides a set of uncorrelated variables

$$\mathbf{Y}^{\rm T} = \mathbf{X}^{\rm T}\mathbf{U}\mathbf{L}^{-1/2}. \tag{3.10}$$

Because components with very small variance will carry very little information, the dimensions of **U** and **L** can be reduced by dropping eigenvectors which have sufficiently small eigenvalues. This technique is very useful in determining patterns in linear, but highly interdependent variables, as is the case with occultation extinction measurements.

Extinction can be written as a function of the Mie extinction efficiency, $Q_\lambda(r)$, integrated over the particle size distribution

$$k_{\text{aer}}(\lambda) = \int_0^\infty \frac{3Q_\lambda(r)}{4r} \frac{dV(r)}{dr} dr, \tag{3.11}$$

where $dV(r)/dr$ is the total volume of aerosol per unit radius between r and $r + dr$. The sensitivity of SAGE II extinction measurements to a particle with radius r and unit volume is then given by the extinction kernel

$$K(r) = \frac{3Q_\lambda(r)}{4r}. \tag{3.12}$$

Figure 3.5 shows the extinction kernels for the four SAGE II channels.

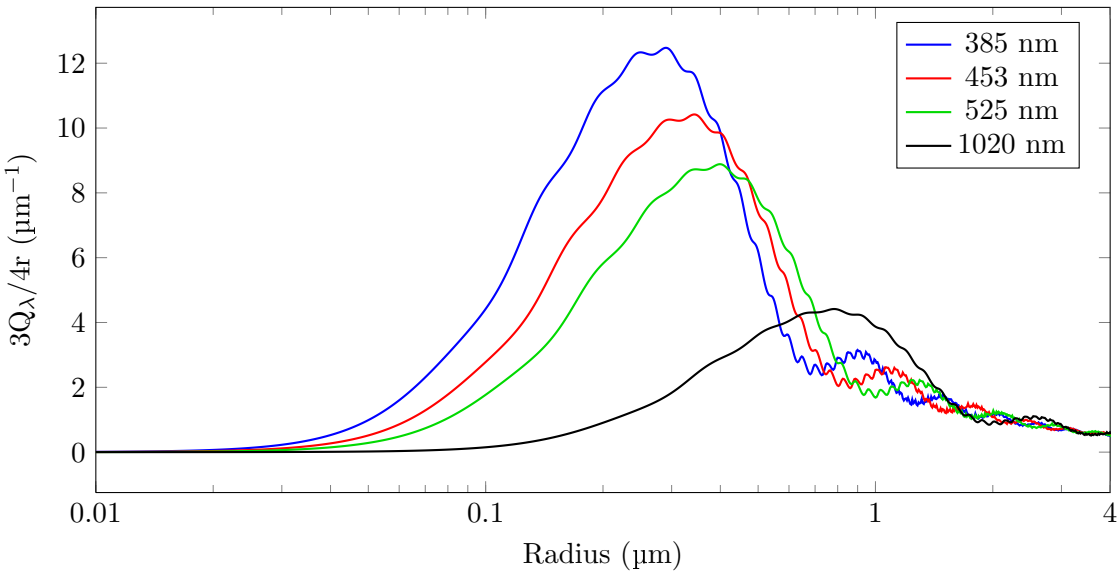

Figure 3.5: Extinction kernels, $3Q_\lambda(r)/4r$, at the four SAGE II wavelengths of 385, 453, 525 and 1020 nm.

Equation 3.11 cannot be directly inverted; however, *Twomey* (1977) noted that the volume element $dV(r)/dr$ can be rewritten as the linear combination of orthogonal functions, $\boldsymbol{\phi}(r)$:

$$\frac{dV(r)}{dr} = \sum_i a_i \phi_i(r) + \Psi_N(r), \tag{3.13}$$

where a are the coefficients that must be determined and $\Psi_N(r)$ accounts for any component of $dV(r)/dr$ that is orthogonal to $\boldsymbol{\phi}(r)$ and thus cannot be reconstructed. Substitution into Equa-

tion 3.11 then gives

$$k_{\text{aer}}(\lambda_i) = \int_0^\infty K_i(r) \sum_i a_i \phi_i(r) dr + \int_0^\infty K_i(r) \Psi_N(r) dr. \tag{3.14}$$

Principal component analysis can be applied to this problem using the covariance matrix

$$C_{ij} = \int_0^\infty K_i(r) K_j(r) dr. \tag{3.15}$$

Or in matrix form

$$\mathbf{C} = \mathbf{K}\mathbf{K}^{\mathrm{T}}. \tag{3.16}$$

This provides the orthogonal set of functions

$$\boldsymbol{\phi}^{\mathrm{T}} = \mathbf{K}^{\mathrm{T}}\mathbf{U}\mathbf{L}^{-1/2}. \tag{3.17}$$

This deviates slightly from the classic PCA due to the kernels which do not have a zero mean, resulting in the first principal component being biased towards the mean value. This is not necessarily problematic however, and when formulated in this manner shares many similarities with the spectral decomposition method employed by *Gilbert* (1971). Substituting into Equation 3.14 then yields

$$k_{\text{aer}}(\lambda_i) = \int_0^\infty K_i(r)(\mathbf{K}^{\mathrm{T}}\mathbf{U}\mathbf{L}^{-1/2}\mathbf{a}) dr + \int_0^\infty K_i(r) \Psi_N(r) dr. \tag{3.18}$$

The second integral term in Equation 3.18 is zero, due to the orthogonality of $\Psi_N(r)$ and $\boldsymbol{\phi}(r)$. Substituting the definition of $\mathbf{C}$ then gives

$$\mathbf{k}_{\text{aer}} = \mathbf{C}\mathbf{U}\mathbf{L}^{-1/2}\mathbf{a}, \tag{3.19}$$

Applying eigenvector decomposition to $\mathbf{C}$ allows Equation 3.19 to be inverted for determination of $\mathbf{a}$:

$$\mathbf{a} = \mathbf{L}^{-1/2}\mathbf{U}^{\mathrm{T}}\mathbf{k}_{\text{aer}}. \tag{3.20}$$

Finally, substitution into Equation 3.13, allows for the determination of the particle size distribution

$$\frac{dV(r)}{dr} = \mathbf{K}^{\mathrm{T}}\mathbf{U}\mathbf{L}^{-1}\mathbf{U}^{\mathrm{T}}\mathbf{k}_{\text{aer}}. \tag{3.21}$$

It is important to note that by defining $\boldsymbol{\phi}$ as a transform of $\mathbf{K}$, any portion of the particle size distribution that is orthogonal to $\mathbf{K}$ will not be retrieved, limiting the accuracy of this retrieval to when $\Psi_N(r)$ is small. Integral property P of the distribution can then be determined through the summation over M volume elements

$$P = \sum_{m=1}^{M} w_m v_m. \tag{3.22}$$

Here, $\mathbf{w}$ is a weighting matrix which converts volume to the desired quantity. For example if surface area density is required $w_m = 3/r_m$. Substitution into Equation 3.21 then yields the integral property in terms of the measured quantity, $\mathbf{k}$:

$$P = \sum_{m=1}^{M} w_m \sum_{i=1}^{N} \phi(r_m)_i a_i = \mathbf{w}\mathbf{K}^{\mathrm{T}}\mathbf{U}\mathbf{L}^{-1}\mathbf{U}^{\mathrm{T}}\mathbf{k}. \tag{3.23}$$

However, as noted above, if the eigenvalues of the covariance matrix are small, then little information is contained in the measurement and large error magnification occurs. To help minimize this, *Thomason et al.* (1997) rejected principal components which did not meet the criterion:

$$\frac{L_{ii}}{L_{\max}} \gg \epsilon^2. \tag{3.24}$$

Where ϵ is the mean relative error in the extinction measurement. This reduces nonphysical oscillations in the retrieval caused by noise with minimal loss of information. This provides integral properties of the particle size, such as total volume and surface area density without the need for *a priori* assumptions about the particle size distribution.

Other groups have applied different techniques to fit unimodal parameters to the SAGE II data including look-up tables (*Bingen et al.*, 2004) and optimal estimation (*Wurl et al.*, 2010), however all have relied on fitting the wavelength dependence of the extinction measurements. While both SAGE II and SME allow for novel techniques in the retrieval of aerosol particle size, both rely on accurate *a priori* measurements of the aerosol column, either in mass density or extinction, before particle size can be retrieved. Since OSIRIS measurements are inherently a product of extinction and the phase function, extinction and particle size retrievals are necessarily coupled, and a new inversion technique must be developed.

Chapter 4

Particle Size Information and Retrieval

This chapter focuses on the sensitivity of limb scatter measurements in general, and those of OSIRIS in particular, to sulphate aerosols, and the ability to retrieve particle size information. First, the measurements are explored using a simple linear approach to better understand the sources of information. Next, examination of the sensitivities is used to determine optimal wavelength choices and measurement vectors. With this knowledge the problem is examined from a linear perspective to determine what quantities can be retrieved, and a SAGE II style particle size retrieval is attempted. Limitations of this technique are overcome through exploration of the non-linear solution space, and finally, a retrieval technique is implemented to maximize the information obtained from simulated measurements.

4.1 Particle Size Information

Particle size affects how light is scattered in two ways, the phase function and the scattering cross section. While molecular scattering has a phase function that is symmetric about a 90° scattering angle, Θ, aerosols scatter light much more asymmetrically, with a strong forward scatter, and for larger particles a peak near 180° as well. The relative intensities of the forward and backward scatter peaks depend on particle size, so measurements of the phase function yield information about the particle size distribution. Figure 4.1 illustrates the different phase functions for typical lognormal aerosol size distributions and OSIRIS viewing geometries; note the large change in phase function between 60° and 120° and the log scale.

Particle size also dictates the total amount of light that will be scattered per particle. Scattering cross sections are inherently wavelength dependent, with Mie theory describing scattering based on the relative size of the particle to the wavelength of light. The integration of cross section over a wide range of particle sizes, such as a lognormal distribution, creates a relatively smooth wavelength

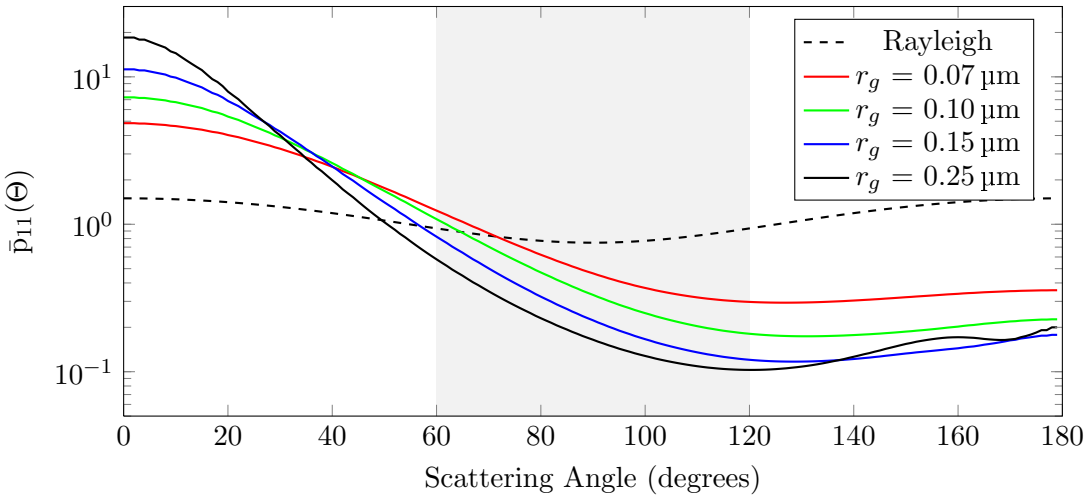

Figure 4.1: 750 nm Phase functions for four different lognormal particle size distributions as well as the Rayleigh background, all with mode width of 1.6. The range of possible OSIRIS scattering angles is shown in grey.

dependence that is often approximated by the Ångström exponent relationship (*Ångström*, 1964):

$$\frac{\sigma_{\text{aer}}(\lambda_1)}{\sigma_{\text{aer}}(\lambda_0)} = \left(\frac{\lambda_1}{\lambda_0}\right)^{-\alpha}. \tag{4.1}$$

This provides a simple linear relationship in log space (log extinction vs. log wavelength) and is often used to map extinction measurements from one wavelength to another. The exact value of α is dependent on the size of the particles with larger particles producing a smaller Ångström exponent. Figure 4.2 shows the wavelength dependence of cross section for a few typical size distributions as well as representative Ångström relationships.

These dependencies can be detected by OSIRIS through the comparison of multiple viewing geometries and multiple wavelengths. From Equation 2.16 the single scatter spectral radiance seen by the OSIRIS satellite at s_1 is

$$I(s_1, \hat{\Omega}_0) = \int_{s_0}^{s_1} F_0(\hat{\Omega}_0) e^{-\tau(\text{sun},s)} e^{-\tau(s,s_1)} k_{\text{scat}}(s) \text{p}(s,\Theta) ds. \tag{4.2}$$

Considering the single scatter approximation and an optically thin atmosphere where $e^{-\tau} \approx 1$, the spectral radiance contribution can be separated into the molecular and aerosol components and Equation 4.2 simplifies to

$$I(s_1, \hat{\Omega}_0) \approx F_0(\hat{\Omega}_0) \int_{s_0}^{s_1} \left[n_{\text{aer}}(s) \bar{\sigma}_{\text{aer}}(s) \bar{\text{p}}_{\text{aer}}(s,\Theta) + n_{\text{mol}}(s) \sigma_{\text{mol}}(s) \text{p}_{\text{mol}}(s,\Theta) \right] ds. \tag{4.3}$$

The spectral radiance contribution from the atmospheric "shells" is dominated by the shell at the tangent point, so for a horizontally homogenous atmosphere the spectral radiance due to aerosol is

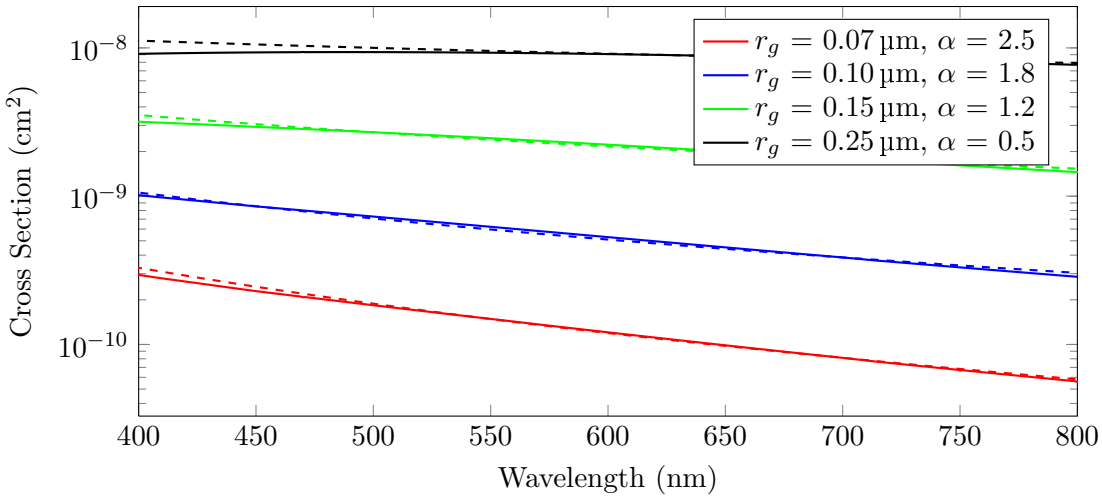

Figure 4.2: Scattering cross sections of a lognormal aerosol distribution as a function of wavelength (solid) with representative Ångström relationships (dashed). All distributions shown with mode width of 1.6.

approximately proportional to the triple product of aerosol number density, scattering cross section and the phase function

$$I_{\text{aer}}(s_1, \hat{\Omega}_0) \propto n_{\text{aer}} \bar{\sigma}_{\text{aer}} \bar{\text{p}}_{\text{aer}}(s, \Theta). \tag{4.4}$$

Equating the measured and modelled spectral radiances and taking a ratio of the two viewing geometries shows that the true phase function information is contained in the ratio of retrieved extinction, k_{ret}, and the *a priori* phase functions at the ascending and descending geometries

$$\left(\frac{\bar{\text{p}}(\Theta_{\text{asc}})}{\bar{\text{p}}(\Theta_{\text{des}})}\right)_{\text{true}} \approx \frac{k_{\text{ret}}(\Theta_{\text{asc}})}{k_{\text{ret}}(\Theta_{\text{des}})} \left(\frac{\bar{\text{p}}(\Theta_{\text{asc}})}{\bar{\text{p}}(\Theta_{\text{des}})}\right)_{a\,priori}. \tag{4.5}$$

The second piece of information available to OSIRIS is in the wavelength dependent extinction measurements. By comparing the measured and modelled spectral radiances at two different wavelengths the relation between retrieved aerosol extinction and the true particle size can be determined

$$\left(\frac{\lambda_1}{\lambda_2}\right)^{-\alpha_{\text{true}}} \left(\frac{\bar{\text{p}}(\lambda_1, \Theta)}{\bar{\text{p}}(\lambda_2, \Theta)}\right)_{\text{true}} \approx \frac{k_{\text{ret}}(\lambda_1)}{k_{\text{ret}}(\lambda_2)} \left(\frac{\bar{\text{p}}(\lambda_1, \Theta)}{\bar{\text{p}}(\lambda_2, \Theta)}\right)_{a\,priori}. \tag{4.6}$$

While Equation 4.5 and Equation 4.6 were derived for an optically thin atmospheric shell, and so cannot be applied directly to the OSIRIS measurements, this shows that there are two additional measurements of aerosol particle size contained in the OSIRIS data, and most importantly the source of that information.

4.1.1 OSIRIS Measurement Sensitivity

In the above analysis the normalization of the 750 nm spectral radiances by the 470 nm spectral radiances, as is done in the current extinction retrievals, was not taken into consideration. Ideally, as shown by *Bourassa et al.* (2007), spectral radiances at short wavelengths such as 470 nm are insensitive to aerosol and normalization only removes the effect of atmospheric density fluctuations. However, this is only an approximation, and in reality the 470 nm spectral radiances are a function of both aerosol extinction and particle size. The effect of normalization on the current extinction retrieval is minimal in the absence of density fluctuations, as it does not greatly affect the linearity of the solution space. This is not the case with particle size where normalization causes large non-linearities in the 750 nm measurement vector, particularly when measuring small aerosol particles. This is demonstrated in Figure 4.3, where the 750 nm measurement vectors (both normalized and unnormalized) for scan 6432012 were modelled for a range of extinctions and particle sizes. While the normalization simply scales the measurement vector as a function of extinction, it produces a more complicated measurement as a function of particle size.

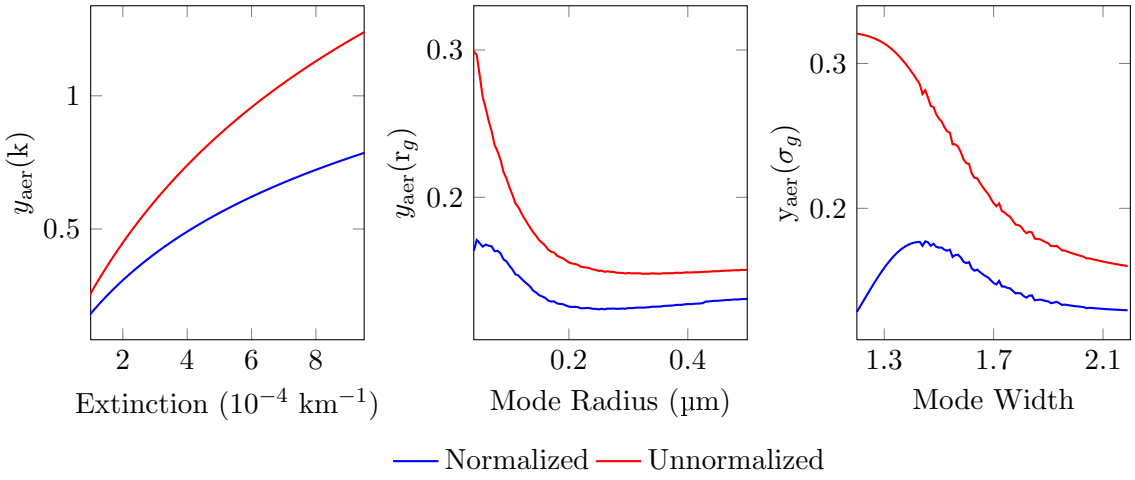

Figure 4.3: Simulated 750 nm measurement vectors at 25 km as a function of extinction (left), mode radius (middle) and mode width (right) for scan 6432012. Shown in blue is the measurement vector normalized with the 470 nm spectral radiances, and without this normalization in red.

Measurement vectors that are strongly non-linear are problematic as most techniques rely on the assumption of at least local linearity when moving around the solution space; slow convergence often results when this assumption is violated. Even more problematic is the tendency for non-linear functions to produce local minimums which the solution can fall into, requiring more

accurate *a priori* assumptions for this to be avoided. For these reasons it is best to leave the aerosol measurement vector unnormalized by a second wavelength when performing particle size retrievals.

To extract particle size information from the wavelength dependence of these measurement vectors, the variability in wavelength due to particle size must be considerably larger than the measurement noise. This variation can be explored by simulating the unnormalized aerosol measurement vector for multiple wavelengths and particle sizes, fully considering the effects of multiple scattering. This was done by assuming a bimodal particle size distribution and modelling the resulting OSIRIS spectral radiances and measurement vectors using SASKTRAN. The simulated spectral radiances were then used to retrieve the aerosol number density at 750 nm for two cases, the current unimodal assumption of 80 nm mode radius and 1.6 mode width, referred to as the "fine mode", and a unimodal distribution with the same surface area density and unit volume as the bimodal case. Figure 4.4 shows that the measurements vectors below approximately 800 nm provide almost no discrimination between particle sizes, and thus little to no additional information that could be used for particle size retrieval. However, measurement vectors at longer wavelengths begin to diverge; by up to 40% at 1.5 µm for the case studied here. While this precludes retrieving particle size with the optical spectrograph alone, the 750 nm measurement can be combined with the infrared imager measurements for at least one piece of particle size information.

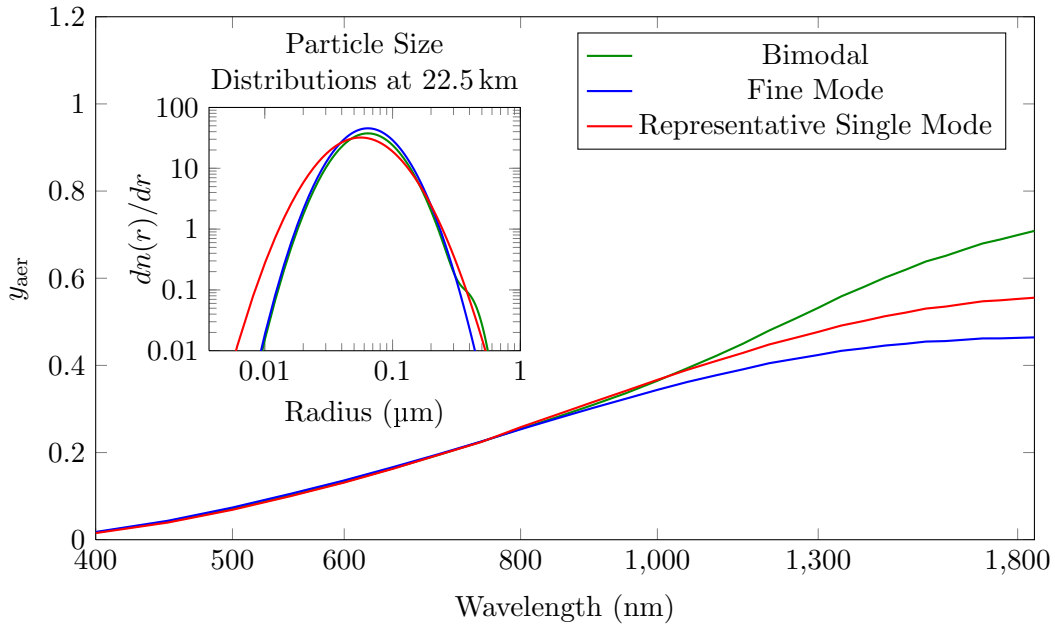

Figure 4.4: Modelled sensitivity of aerosol measurement vectors from scan 6432001 as a function of wavelength for three particle size distributions at 22.5 km. Shown in inset are the three size distributions.

The sensitivity of the aerosol measurement vectors as a function of scattering angle and particle size is shown in Figure 4.5 for the same atmospheric conditions used in Figure 4.4. The measurement vector at 750 nm is only weakly dependent on particle size, so provides little additional information. In comparison, the 1.53 µm measurement vector is strongly dependent on particle size over the range of OSIRIS geometries and so also provides particle size information.

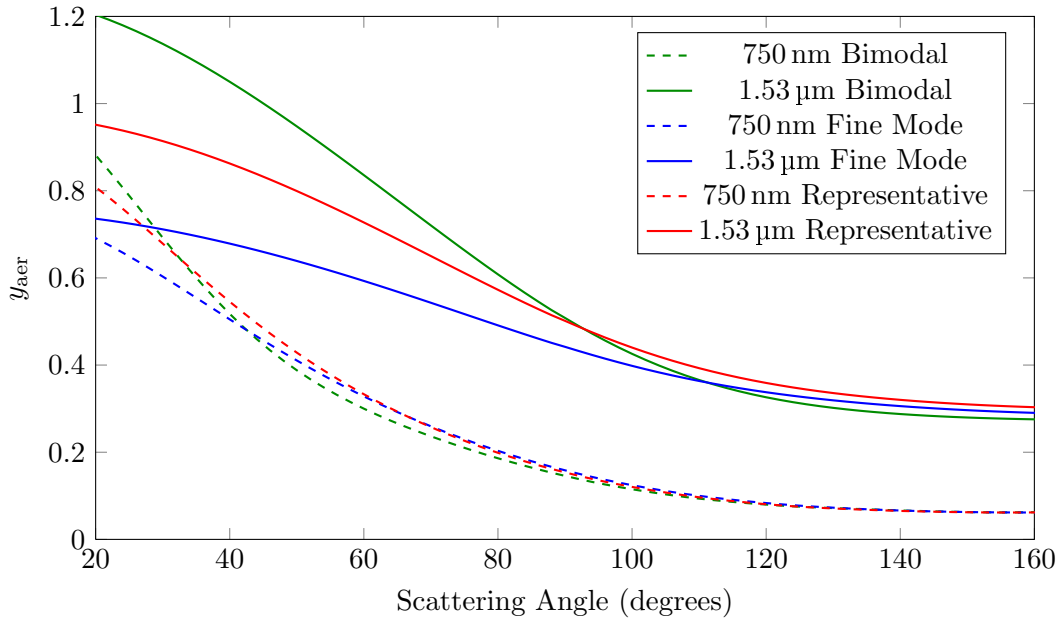

Figure 4.5: Modelled sensitivity of aerosol measurement vectors as a function of scattering angle for three particle size distributions, a bimodal lognormal ($r_g = 0.08/0.4\,\mu m$, $\sigma_g = 1.6/1.2$) shown in black, fine mode unimodal ($r_g = 0.08\,\mu m^3$, $\sigma_g = 1.6$) shown in blue and a second unimodal ($r_g = 0.077\,\mu m$, $\sigma_g = 1.75$) shown in red.

4.1.2 Particle Size Measurement Vectors

The analysis above showed that particle size information is available through both the wavelength dependence of the aerosol measurement vectors as well as the comparison of multiple viewing geometries. However, not all wavelengths and geometries were equally sensitive and optimizing a retrieval requires choosing measurement vectors that both maximize the sensitivity to the desired quantity and minimize the inversion time. As seen in Figure 4.4, measurement vectors at wavelengths less than approximately 800 nm show no discrimination in particle size, so including multiple short wavelength measurement vectors quickly increases inversion time with little benefit. Although including multiple NIR channels would be beneficial, only 1.26, 1.27 and 1.53 µm channels are available, with the two shorter channels contaminated by the oxygen emission bands that they were designed to

measure. Selection of wavelengths is then straightforward, with the 750 nm and 1.53 µm channels being used to construct two aerosol measurement vectors. The OSIRIS geometry also provides measurements of a forward and backscatter geometry of similar atmospheric conditions, one on the ascending and one on the descending node, providing an additional two measurement vectors for matched pair conditions. The new aerosol measurement vectors, y_k at a tangent altitude j are then:

$$y_{kj} = \ln\left(\frac{I(j,\lambda_k,\theta_k)}{I_{\text{Ray}}(j,\lambda_k,\theta_k)}\right) - \frac{1}{N_k}\sum_{j=m_k}^{m_k+N_k}\ln\left(\frac{I(j,\lambda_k,\theta_k)}{I_{\text{Ray}}(j,\lambda_k,\theta_k)}\right), \tag{4.7}$$

where λ is the wavelength, θ, the scattering angle and N high altitude measurements have been used for normalization. These are similar to the measurement vector used in the MART retrievals, shown in Equation 2.46, except they are unnormalized by the 470 nm measurements, and now include a wavelength and scattering angle dependence. The wavelengths and viewing geometries for a set of measurement vectors in a matched pair scan are shown in Table 4.1.

Table 4.1: Wavelengths and geometries used in the aerosol measurement vectors

Measurement Vector	Wavelength	Viewing Geometry
y_1	750 nm	Ascending
y_2	750 nm	Descending
y_3	1.53 µm	Ascending
y_4	1.53 µm	Descending

4.1.3 Measurement Vector Information Content

While the measurement vectors contain particle size information, both as a function of wavelength and scattering angle, these pieces of information are not independent, and the ability to derive multiple pieces of information depends on both the orthogonality of the measurement vectors and the instrument noise. *Twomey* (1977) explored a method of determining information content of a measurement set based on the orthogonality of the measurement kernels. Similar to the analysis done by *Thomason and Poole* (1992) in determining particle size properties from the SAGE II data, the analysis relies on the ability to write the measurement, y, as an integration over the kernel such as

$$y_k = \int_0^\infty K_k(r)\frac{dV(r)}{dr}dr. \tag{4.8}$$

For occultation measurements this equation is accurate due to the fact that the measurements are linear - addition of a particle of size r, does not affect the shape of the kernel, $K(r)$. This is not strictly true in limb measurements due to the effects of multiple scattering. Adding a particle of radius r will affect the amount of light that is scattered by other aerosol particles, changing $K(r)$ for all r. The applicability of this technique to OSIRIS measurements is then limited by the amount of aerosol-to-aerosol multiple scatter, and as this term increases Equation 4.8 becomes increasingly inaccurate. For low values of aerosol, however, this is a good approximation, and the analysis can yield important understanding about the information content of OSIRIS measurements. For clarity, the kernel can also be derived for a limb scatter measurement in an optically thin atmosphere. Here the spectral radiance due to aerosol particles is given by Equation 4.4, and the kernel can be written as:

$$K_k(r) = \frac{3}{4\pi r^3}\sigma_{\text{aer}}(\lambda_k, r)\text{p}(\Theta_k, \lambda_k, r). \tag{4.9}$$

The more accurate kernel, which includes multiple scatter terms, can be computed by modelling the OSIRIS measurement vectors for a range of monodisperse aerosol particles of radius r with constant aerosol volume density. This was done for a matched pair of scans and the kernels are shown in Figure 4.6. Also included are the single scatter kernels for comparison. Despite the approximations, agreement is quite good, with similar peaks and sensitivities.

While the shape of each measurement kernel is different there is still significant overlap of the kernels, indicating the interdependence of the measurements. Extracting information from highly interdependent measurements is difficult and extracting a unique piece of information from each measurement can require unrealistically high signal to noise. It is possible to assess the information content of a noisy measurement set based on the kernels using eigenvector analysis explored by *Twomey* (1977). In this analysis a measurement can be thought of as containing information if it cannot be predicted within error from other measurements. Predicting a measurement is possible if the kernel can be written as a linear combination of other kernels

$$K_k(r) = -a_k^{-1}\sum_{l\neq k} a_l K_l(r), \tag{4.10}$$

where, $K_k(r)$ is the predicted kernel as a function of particle radius. If the kernel $K_k(r)$ can be predicted, so too can the measurement since,

$$y_k = -a_k^{-1}\sum_{l\neq k} a_l \int K_l \frac{dV(r)}{dr} dr = -a_k^{-1}\sum_{l\neq k} a_l y_l. \tag{4.11}$$

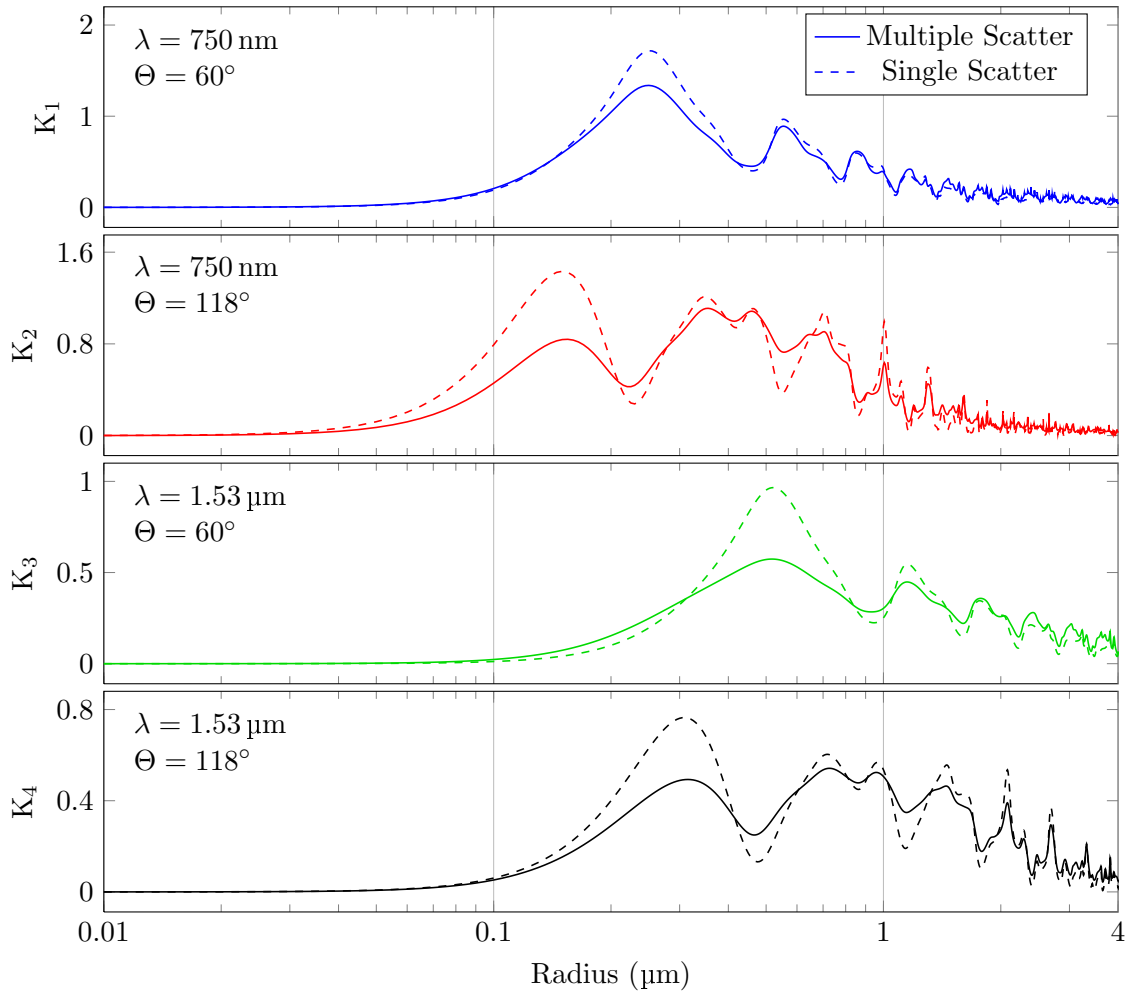

Figure 4.6: Simulated measurement vector kernels for the scans 12312061 and 12320026 at 22.5 km for a range of monodisperse particles with radius r. Area has been normalized to one for all kernels.

This is strictly true only if the k^{th} eigenvalue, L_{kk}, of the covariance matrix, $\mathbf{K}\mathbf{K}^{\mathrm{T}}$ is zero. However, if the eigenvalue is sufficiently small, then the measurement can be predicted within error. The number of independent measurements is then determined by the number of eigenvalues which exceed the threshold:

$$\sqrt{\frac{L_{kk}}{L_{\max}}} \gg \epsilon, \tag{4.12}$$

where ϵ is the relative measurement error. For the kernels shown in Figure 4.6 the eigenvectors are:

$$\begin{bmatrix} 0.5476 \\ 0.5876 \\ 0.4098 \\ 0.4323 \end{bmatrix}, \begin{bmatrix} -0.3629 \\ -0.4746 \\ 0.5581 \\ 0.5758 \end{bmatrix}, \begin{bmatrix} 0.7414 \\ -0.6457 \\ -0.1593 \\ 0.0895 \end{bmatrix}, \begin{bmatrix} -0.1368 \\ 0.1120 \\ -0.7037 \\ 0.6881 \end{bmatrix}, \tag{4.13}$$

with normalized eigenvalues:

$$1.000, 0.0807, 0.0425, 0.0144. \tag{4.14}$$

This translates to three pieces of information if the relative error in the measurements is significantly better than 20% and four pieces if the error is significantly better than 10%. It is important to note though, that three or more pieces of information does not guarantee the retrieval of the desired quantities relating to the aerosol particle size distribution. For example, from Figure 4.6 it is clear that the kernels are insensitive to particles much smaller than 100 nm in size, and thus no information about the number of these small particles is present in the measurements. The amount of particles below approximately 100 nm can only be determined through the sensitivity to larger particles and the assumed shape of the size distribution. More generally, the ability to derive a quantity, q, from the measurements is determined by whether or not q is in the null space of the kernels. If q can be written as

$$q = \int_0^\infty \Psi(r) \frac{dV(r)}{dr} dr, \tag{4.15}$$

then the accuracy of the retrieved quantity, $\hat{q}$, depends on the ability to write $\Psi(r)$ as a linear combination of the kernels. This can be seen from the equation:

$$q = \int_0^\infty \Psi(r) \frac{dV(r)}{dr} dr \approx \int_0^\infty \sum_k a_k K_k(r) \frac{dV(r)}{dr} dr = \sum_k a_k y_k. \tag{4.16}$$

If the substitution of $\Psi(r)$ with the kernels is possible, then measurements of q, can be obtained directly from y. Transforming the kernel into the principal components, $\boldsymbol{\phi}$, then allows $\Psi(r)$ to be built from a set of orthogonal functions. The principal components for the multiple scatter kernels shown in Figure 4.6 were computed using Equation 3.17 and are shown in Figure 4.7. The retrieved quantity, $\hat{q}$ can then be written as the sum of the principal components projected along $\Psi(r)$ and integrated over the particle size distribution

$$\hat{q} = \int_0^\infty \sum_k (\boldsymbol{\Psi} \cdot \boldsymbol{\phi_k}) \phi_k(r) \frac{dV(r)}{dr} dr. \tag{4.17}$$

The ability to retrieve real quantities from OSIRIS measurements is then given by how accurately $\Psi(r)$ can be approximated from the principal components. As an example $\Psi(r)$ can be determined for two quantities, extinction, k_{aer} and number density, n_{aer}. Written in integral form these are:

$$\begin{aligned} k_{\text{aer}} &= \int_0^\infty \frac{3}{4\pi r^3} \sigma_{\text{aer}}(\lambda, r) \frac{dV}{dr} dr, \\ n_{\text{aer}} &= \int_0^\infty \frac{3}{4\pi r^3} \frac{dV}{dr} dr. \end{aligned} \tag{4.18}$$

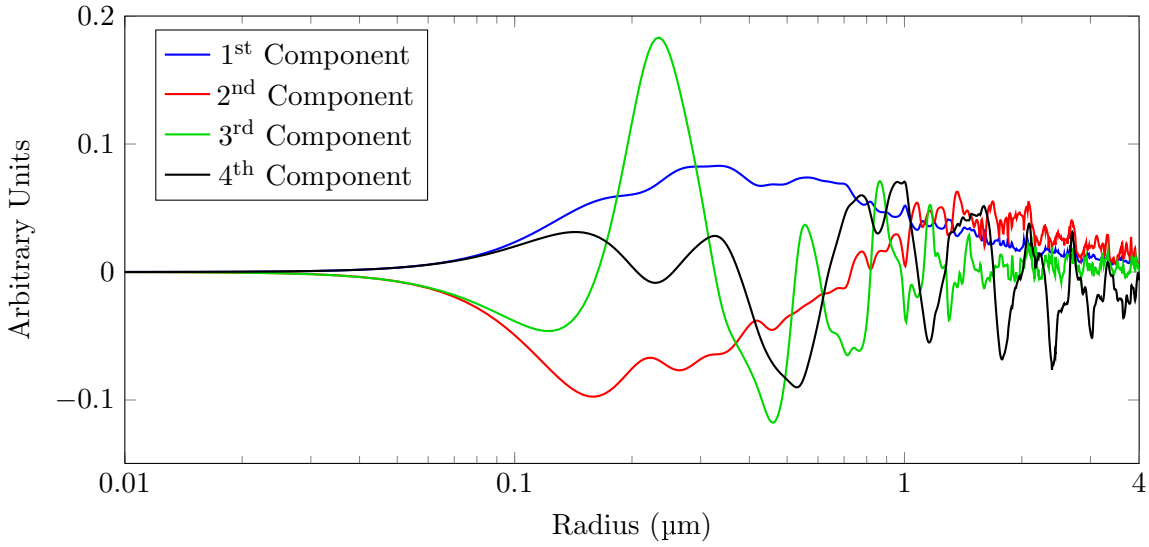

Figure 4.7: Principal components of the limb scatter kernels for the scans 12312061 and 12320026 at 22.5 km.

Providing,

$$\begin{aligned} \Psi_{k_{\text{aer}}}(r) &= \frac{3}{4\pi r^3}\sigma_{\text{aer}}(\lambda, r), \\ \Psi_{n_{\text{aer}}}(r) &= \frac{3}{4\pi r^3}. \end{aligned} \tag{4.19}$$

Results are shown in Figure 4.8. The $\Psi_{n_{\text{aer}}}(r)$ resulting from the number density is very poorly approximated by the measurement kernels, and consequently number density is essentially impossible to retrieve with almost any particle size distribution. Conversely, $\Psi_{k_{\text{aer}}}(r)$ is well approximated by the kernels above particle sizes of approximately 200 nm. This implies that if the majority of extinction is due to larger particles, OSIRIS measurements can determine extinction independent of the assumed size distribution. It is worth reiterating here that the function $\Psi_{k_{\text{aer}}}(r)$, which must be rebuilt using limb scatter kernels, is precisely the kernel for occultation measurements; illustrating the fundamental difference between the measurement types, and the reason for high quality occultation extinction measurements.

This result can be used to perform particle size retrievals similar to those done by *Thomason et al.* (1997) on the SAGE II data. While extinction itself is not a direct measurement of particle size, the kernels can be constructed to measure total volume, using $\Psi(r) = 1$. Equation 3.23 can then be rewritten in terms of the OSIRIS measurement vectors, yielding

$$\frac{dV(r)}{dr} = \mathbf{K}^{\mathrm{T}}\mathbf{U}\mathbf{L}^{-1}\mathbf{U}^{\mathrm{T}}\mathbf{y}. \tag{4.20}$$

The ability to retrieve a particle size distribution from this technique can be tested by modelling the

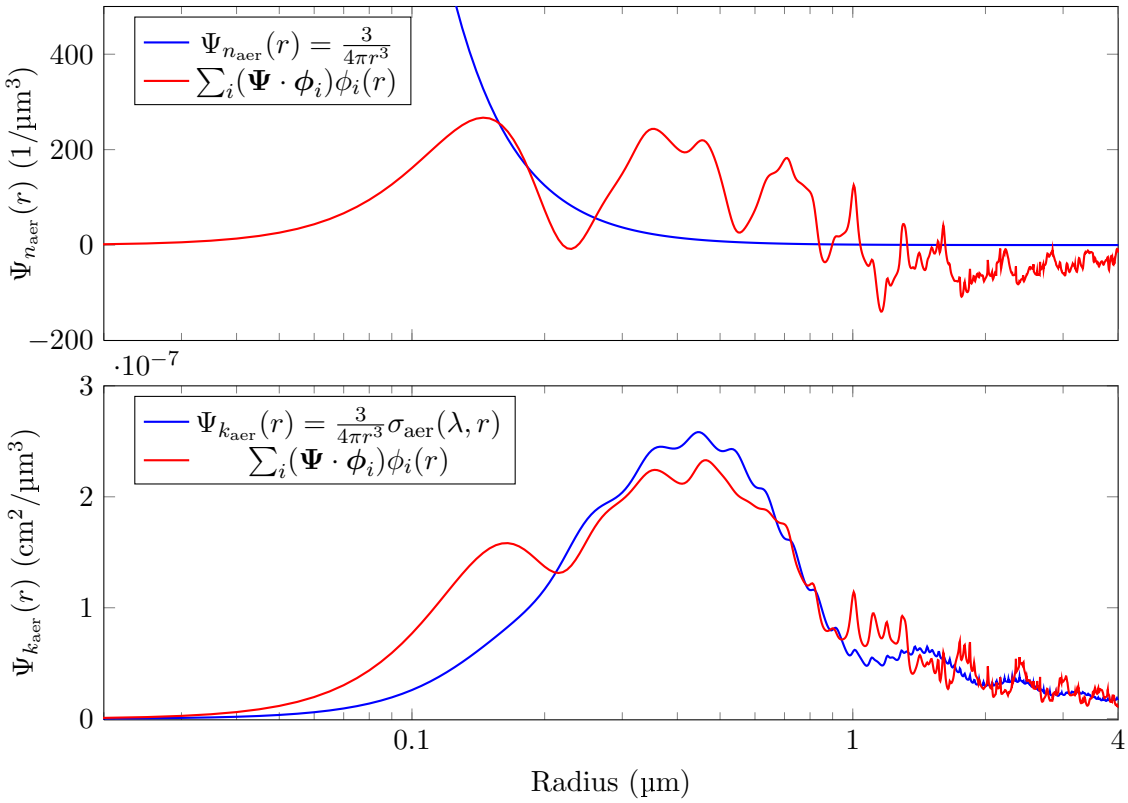

Figure 4.8: Ability of the limb scatter kernels to determine the extinction and number density for particles of radius r. Accurate retrievals are possible when $\Psi(r)$, shown in blue is well approximated by the linear sum of principal components, $\boldsymbol{\phi}$, shown in red.

measurement vectors and kernels in a single scatter atmosphere for a variety of particle size distributions, then inverting the simulated measurements using Equation 4.20. The reason for assuming a single scatter atmosphere for this test is that multiple scattering produces a nonlinear problem, with the kernels requiring calculation at each iteration. This quickly becomes infeasible, particularly when testing multiple scenarios and is unnecessary to see the advantages and limitations of the technique. Thus a single scatter approximation was used for nine different unimodal distributions, all with a total aerosol volume of 3.4x10^{-6} µm^3/cm^3; results are shown in Figure 4.9. As expected, distributions comprised primarily of particles smaller than 200 nm are poorly retrieved due to the insensitivity of the measurements at these sizes. Larger particles are more accurately retrieved; although high frequency oscillations are still present due to the nature of the kernels. Overall, error in the retrieved total volume is typically on the order of 50%, with much of this coming from the over or underestimation of small particles. Despite the error, the retrieved distributions still yield useful information on the shape and peak of the true distribution with no need for a priori assumptions.

While this type of analysis gives important clues to the information content of the OSIRIS

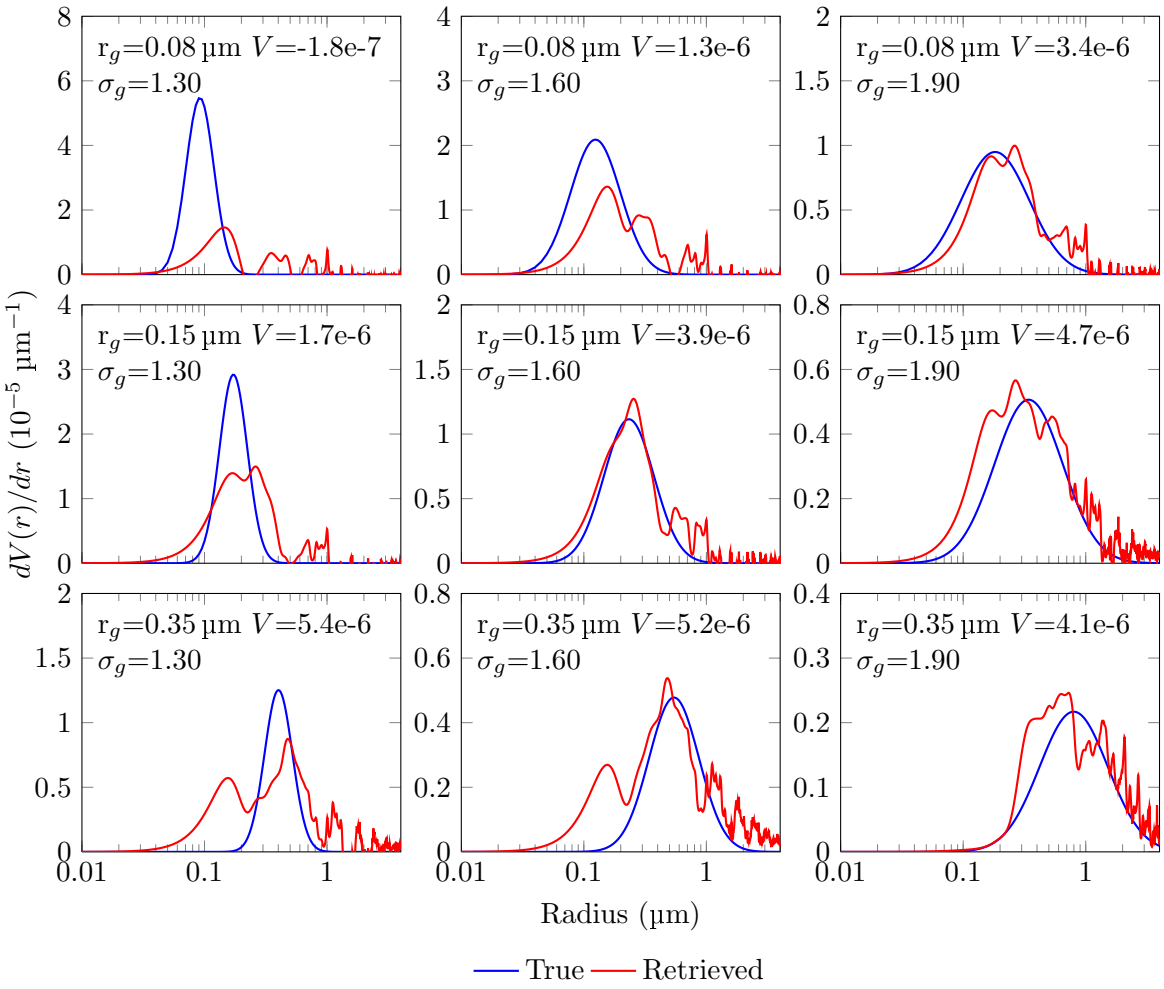

Figure 4.9: Particle size retrievals using the OSIRIS measurement kernels for nine unimodal lognormal distributions assuming a single scatter atmosphere. The true state is shown in blue and the retrieved state shown in red. True aerosol volume density is 3.4×10^{-6} µm^3/cm^3 for all tests with retrieved volume, V shown in panels in units of µm^3/cm^3.

measurements, and can be used as an inversion technique as seen in Figure 4.9, several drawbacks make it impractical for large scale retrievals.

1. Equation 4.8 is an increasingly poor approximation during periods of heightened aerosol loading, which increases aerosol-to-aerosol multiple scatter.
2. The kernels are computationally expensive, requiring the measurement vectors to be modelled at hundreds of aerosol particle sizes for each scan geometry and atmospheric parameter tested.
3. The kernels are insensitive to small particles, which can compose a large portion of the fine mode distribution, leading to large error in the retrieved extinction and particle size properties.
4. Retrieved distributions have unrealistic high frequency oscillations due to the nature of the kernels and the lack of constraints imposed on the retrievals.

For these reasons it is best to use the *a priori* knowledge about the shape of the aerosol distribution when performing retrievals. This allows for more physically realistic distributions as well as measurements of small particles and the incorporation of aerosol-to-aerosol scattering in the model. The ability to retrieve a size distribution of known shape with unknown parameters, is then determined by the sensitivity of the measurements to those parameters, rather than particles of a monodisperse size.

4.1.4 The Lognormal Solution Space

For a unimodal lognormal size distribution three parameters must be determined: number density (or extinction), mode radius, and mode width. The sensitivity, and difference in sensitivity, to these parameters by the four measurements dictates the accuracy with which they can be retrieved. The sensitivity can be tested by modelling the measurement vectors at a variety of particle sizes and extinctions. If variation of the measurement vectors is large, then sensitivity is good and retrievals are likely possible. In Figure 4.10 the measurement vectors of the matched pair scans 12312061 and 12320026 were simulated for a variety of unimodal lognormal distributions with constant extinction. In general, the 750 nm measurement vectors (y_1 and y_2) are systematically smaller than their 1.53 µm counterparts due to the aerosol scattering cross section that increases with shorter wavelengths much less rapidly than the Rayleigh scattering. Measurement vectors with backscatter geometries (y_2 and y_4) are also smaller due the phase function minimum that typically occurs around 120 degrees.

The measurement vectors are clearly sensitive to the lognormal parameters. However, the sensitivity is similar in all cases with the measurement vectors being approximately constant as mode

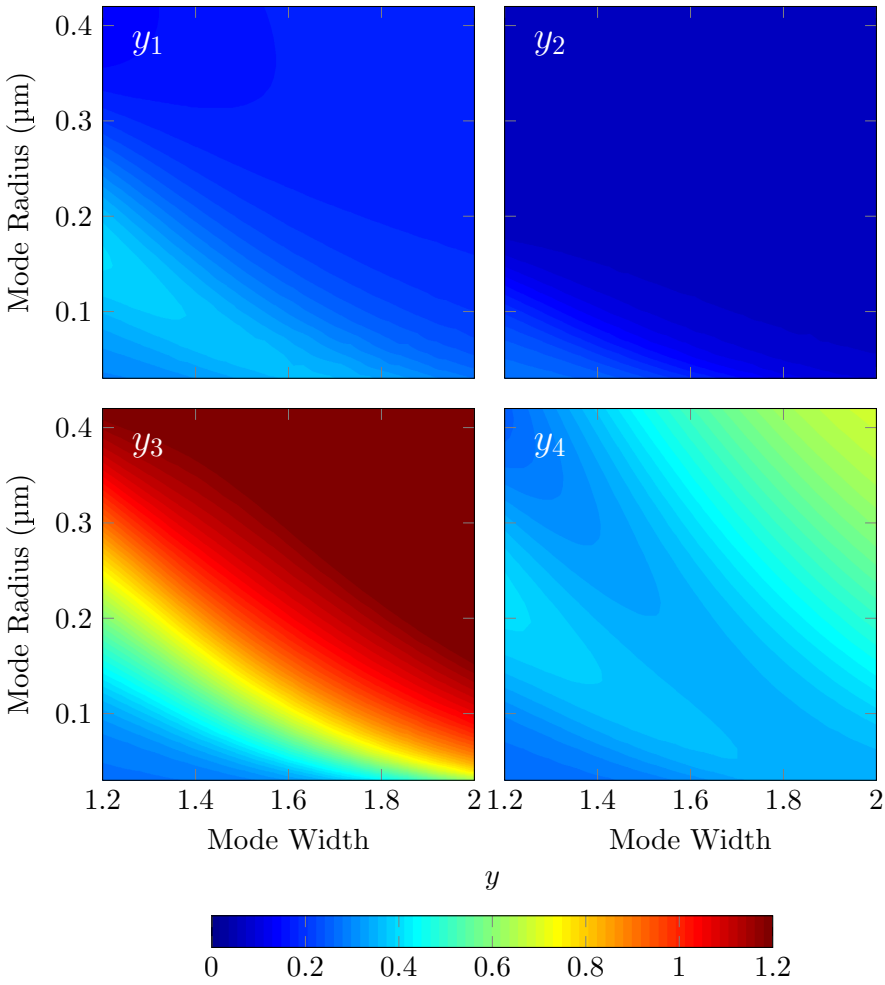

Figure 4.10: Modelled aerosol measurement vectors at 22.5 km as a function of particle size for the scans 12312061 (left column) and 12320026 (right column) at 750 nm (top row) and 1.53 µm (bottom row). 750 nm extinction at 22.5 km is constant at 5.4×10^{-4}.

width increases and radius decreases. This has the possibility of producing large regions of overlapping solutions, where all four measurement vectors agree over a range of particle sizes. The accuracy with which one can find the true solution depends largely on the precision of the measurement vectors, which dictates the uniqueness of the solution given some measurement noise. If the difference between the model and the measurement is less than the measurement error, $|F(\mathbf{x}, \tilde{\mathbf{b}}) - y| \leq \epsilon$, then no additional information is present. Any solution in which all measurement vectors are within error of the model is then valid. The problem can then be restated as minimizing the difference between the model and the measurement, also known as the residual, S. For aerosol retrievals this is minimizing the residual for all measurements at all altitudes

$$S(\mathbf{n}_{\text{aer}}, \mathbf{r}_{\mathbf{g}}, \boldsymbol{\sigma}_g) = \sum_k \sum_j \left(y_{kj} - F(\mathbf{n}_{\text{aer}}, \mathbf{r}_{\mathbf{g}}, \boldsymbol{\sigma}_g, \tilde{\mathbf{b}}) \right)^2 . \tag{4.21}$$

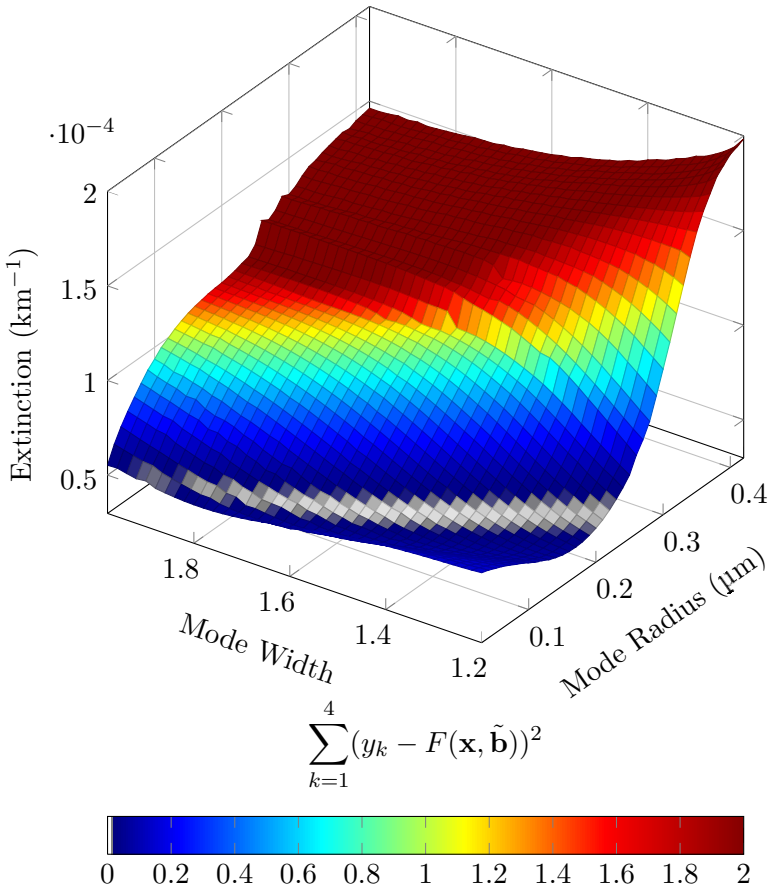

Figure 4.11: Solution space for matching pair 12312061 and 12320026 at 22.5 km with true extinction of 5.4×10^{-5} km^{-1}, mode radius of 0.08 µm, and mode width of 1.6.

Figure 4.11 shows the residual, S, at 22.5 km for a range of particle sizes and extinctions such that the 750 nm measurement vector of scan 12312061 is constant anywhere on the plane. This is equivalent to retrieving the extinction using a single measurement vector and given particle size distribution. Note that depending on the chosen distribution the retrieved extinction varies between approximately 0.4×10^{-5} and 2.0×10^{-5} km^{-1}. With measurement vector noise of 0.01 the solution is well constrained with extinction varying by less than 2% from the true solution. If noise is increased to 0.05, the extinction is still accurate to better than 10%. Particle size, however, can no longer be determined uniquely, and is constrained only to a wide line in the solution space.

This shows that even with relatively small amounts of measurement uncertainty multiple solutions still exist using these four measurement vectors. However, the extinction is much more constrained provided the true state is well approximated by a unimodal lognormal distribution. As well, although a unique particle size cannot be determined improved estimates are still possible. This result confirms much of the linear analysis performed in subsection 4.1.3, showing that while

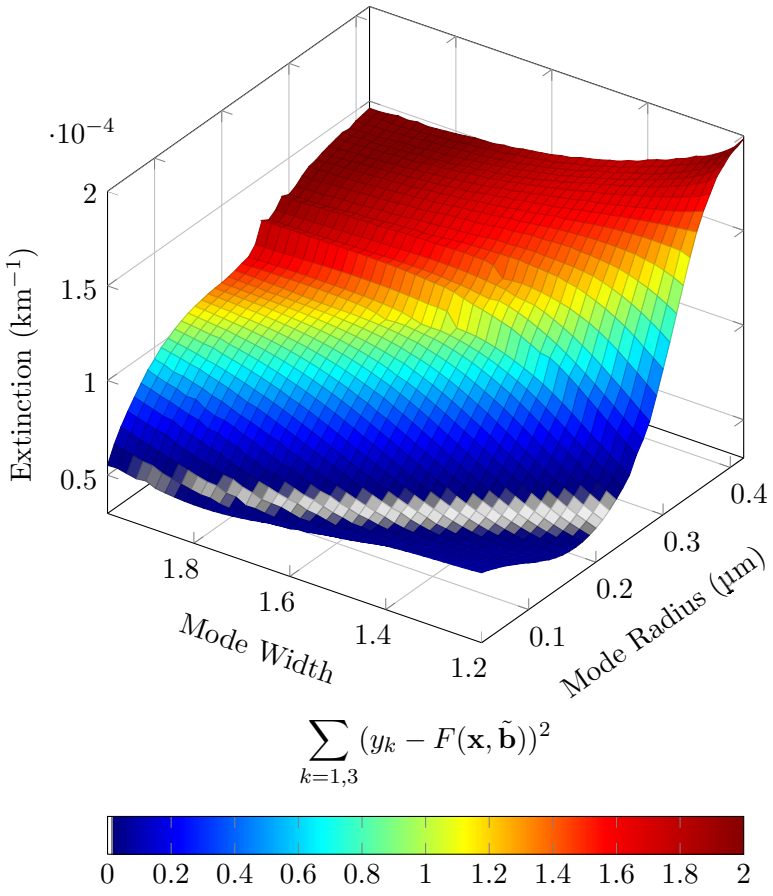

Figure 4.12: Solution space for scan 12312061 at 22.5 km using only 750 nm and 1.53 µm channels. True extinction of 5.4×10^{-5} km^{-1}, mode radius of 0.08 µm, and mode width of 1.6.

four measurements are made, deriving three particular quantities is not necessarily possible, and also that when combined these measurements are quite sensitive to the true extinction.

The fact that typically only two quantities can be derived from four measurements when the full non-linear system is considered implies that the measurements of the lognormal parameters are not independent. While reducing the amount of information retrievable from the system, it also suggests that the system might be well determined without the need for two scans in a single retrieval. Using matched pairs comes at several costs, most notably the limited amount of matched pairs that are available, especially in the later half of the mission, so retrieval on a scan-by-scan basis is certainly advantageous. While eliminating two measurements precludes retrieving all three unimodal parameters, the stability of extinction along the solution space minimum suggests an improved extinction is still possible. This is testable by remaking the solution space using only one geometry. If the solution is still constrained to a line of approximately constant extinction, then the retrieved extinction will be independent of the assumed mode width, or mode radius, provided at

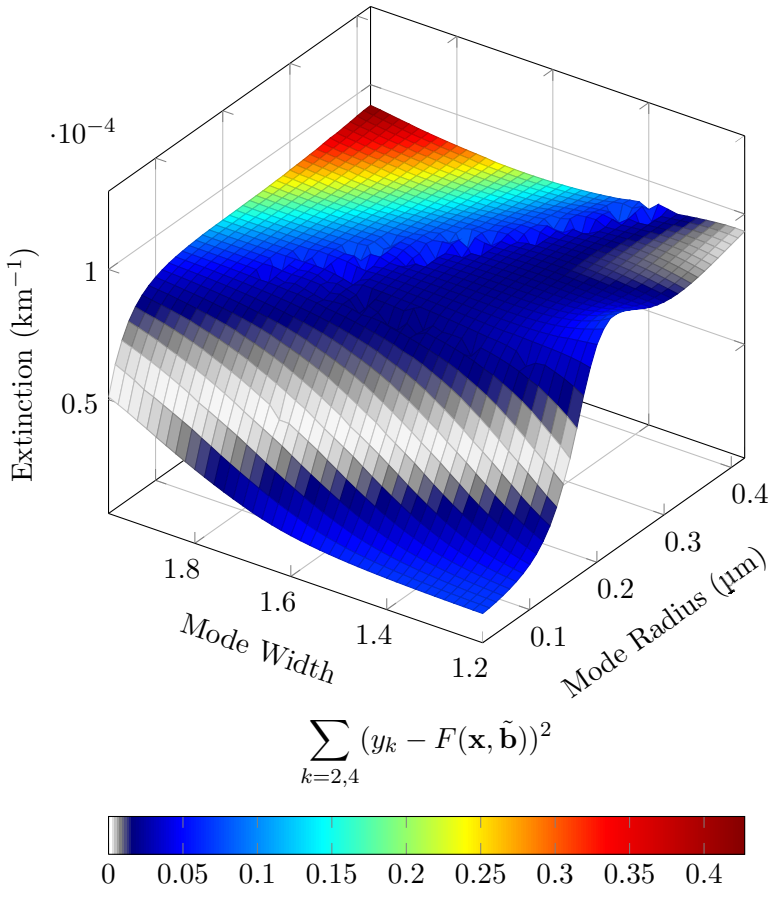

Figure 4.13: Solution space for scan 12320026 at 22.5 km using only 750 nm and 1.53 µm channels. True extinction of 5.4×10^{-5} km^{-1}, mode radius of 0.08 µm, and mode width of 1.6.

least one size parameter is retrieved. Shown in Figure 4.12 is the solution space for scan 12312061 treated independently.

The valid solution is now broader for a given noise threshold. Most importantly though, the valid solutions still lie on an approximately constant line of extinction. This is true for the backscatter case as well, and is shown in Figure 4.13. The solution space for this geometry has a much wider minimum due to the decreased sensitivity of the backscatter geometry. However, valid solutions lie along essentially the same line of approximately constant extinction as was seen in the forward scatter case. This implies that extinction can be retrieved without the need to determine both size parameters, for both forward and backscatter geometries, provided one size distribution parameter is retrieved.

Although retrieval of a mode width or mode radius parameter will yield a more accurate extinction value, the retrieved size parameter will be highly sensitive to the parameter that is chosen to be constant. For example, for the forward scatter geometry and atmospheric state described above

if the mode width is set to be 1.8, then a mode radius of approximately 0.05 µm would be retrieved. However, if the mode width was set to be 1.2 a much larger mode radius of 0.22 µm would be found. This is much the same problem as was initially encountered with number density, and was solved by converting number density to extinction which was much less sensitive to the assumed parameters. A similar method can be utilized to improve the determination of particle size by converting the retrieved parameter to an Ångström coefficient. The effect of this can be seen in Figure 4.14. The valid solutions for the forward scatter measurement are bounded by the solid white contours for a noise margin of 0.03. The dashed white contours are similar, showing the valid solutions for the backscatter measurement. The large overlap in the valid solutions is the reason a unique particle size cannot be determined.

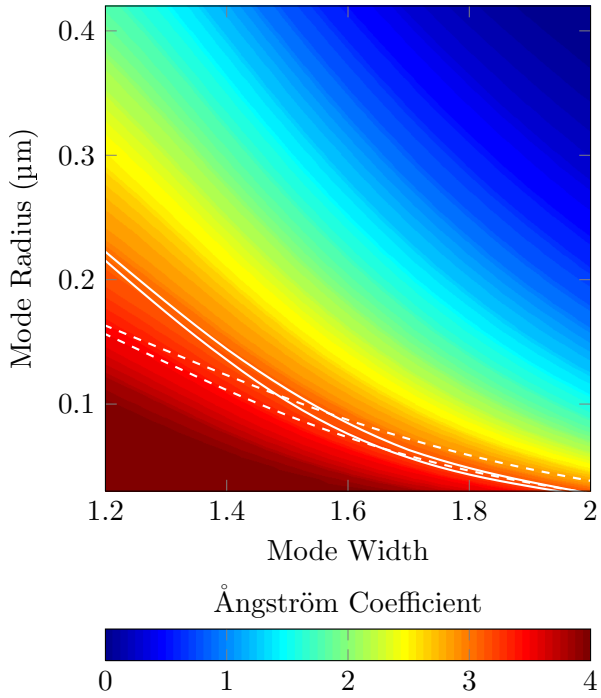

Figure 4.14: Ångström coefficient as a function of mode radius and mode width. The solid white contours denote valid solutions for the forward scatter measurements with dashed white contours showing valid solutions for the backscatter geometry, both with noise of 0.03.

Although the mode width varies by a factor of two, and the mode radius by nearly a factor of five the Ångström coefficient changes by only ±10% within the valid solutions, suggesting this is much less sensitive to the assumed size distribution parameter, and a more robust retrieval quantity. While it is less dependent on the assumed parameter it is still somewhat dependent on the solar geometry, as can be seen at smaller mode widths where the solutions begin to diverge, although again this effect is smaller compared to change in the mode radius. It is important to note that

while this analysis sheds light on the sensitivity of the measurement vectors to various parameters, it is difficult to infer the effects of coarse mode particles, altitude coupling, and changes in geometry from these limited solution spaces. For this, a full retrieval must be performed under a variety of conditions.

4.2 A Mode Radius Retrieval

With the goal of retrieving extinction and the Ångström coefficient, solving for the atmospheric state is equivalent to searching the solution space for the point which minimizes Equation 4.21 with the modification that one size parameter is assumed constant. While choice of the set parameter is somewhat arbitrary, the solution spaces provide information on the optimal choice. If mode radius is chosen any noise on the measurement can alter mode width by relatively large amounts, in addition, if the mode radius is chosen too far from the true state no solutions may exist. Conversely, if mode width is chosen, error in the measurement alters the mode radius by relatively small amounts; as well, practically any choice of mode width provides a valid solution. For these reasons it is best to set mode width and retrieve the mode radius. There are several possible methods for this; however, for multidimensional non-linear problems Levenberg-Marquardt is often the best, as it provides a good combination of speed and robustness. For this problem the Jacobian for a particular altitude, j, can be written

$$\mathbf{K}_j = \begin{pmatrix} \dfrac{\partial y_j(750\,\mathrm{nm})}{\partial r_g} & \dfrac{\partial y_j(750\,\mathrm{nm})}{\partial n_{\mathrm{aer}}} \\ \dfrac{\partial y_j(1.53\,\mu\mathrm{m})}{\partial r_g} & \dfrac{\partial y_j(1.53\,\mu\mathrm{m})}{\partial n_{\mathrm{aer}}} \end{pmatrix}. \tag{4.22}$$

Strictly speaking, the retrieval of mode radius and extinction is only two dimensional when altitude coupling is neglected, and the full Jacobian would include these coupling terms. This creates a much higher dimensional problem, and the computation time of the Jacobian quickly becomes unmanageable. Fortunately, for long wavelengths altitude coupling is minimal and inclusion of these terms is often unnecessary for convergence. Despite this, the effect of altitude coupling cannot be completely ignored in the formulation of the Levenberg-Marquardt solution, as it plays an important role in the determination of the damping factor, γ.

Ideally, the damping factor is calculated such that the step is taken within an approximately linear region of the solution space. *Marquardt* (1963), suggested assuming an initial $\gamma = \gamma_0$, calculating a step, and performing the iteration. If the residual is increased, the step is rejected and γ is increased by a factor of ν. This is repeated until the step improves the residual and the iteration is

kept. If the solution is improved sufficiently, γ can be reduced so the next iteration takes a larger step to decrease the number of iterations required for convergence. The difficulty in applying this technique to a coupled problem is that the residual for a particular altitude may increase due to coupling despite the solution moving closer to the true state. As well, calculating a damping factor based on the total residual may keep γ unnecessarily large for most altitudes, slowing convergence. This problem can be avoided by using a less rigorous determination of γ based on Marquardt's method, but with the relaxed constraint that the γ is only increased if the total residual increases past a certain point relative to the previous iteration. While this does not guarantee convergence, proper choice of this threshold can provide good results that are relatively robust and less affected by the altitude coupling. This can be further improved by initializing the aerosol profile using a MART retrieval on one of the measurement vectors. While any measurement vector will provide a good estimate the 750 nm measurement provides the best signal to noise so it is used for the initialization. The retrieval then proceeds as follows:

1. Determine the aerosol profile using the *a priori* particle size estimate and a MART retrieval on the 750 nm measurement.
2. Calculate the Jacobian based on the current estimate.
3. Determine the improved mode radius and extinction estimate at each altitude using the Levenberg-Marquardt algorithm.
4. (a) If the increase in the total residual is more than 2% reset the atmospheric state to the previous iteration, and set $\gamma = \gamma \cdot 10$.
   (b) If the total residual is reduced by more than a factor of five keep the step and set $\gamma = \gamma/2$.
   (c) If the solution has converged, stop.
   (d) Otherwise, proceed to step 2.

Another benefit of using a Jacobian based search is the ease of convergence testing. Minimums are defined by the slope equalling zero, so the norm of the Jacobian provides a clear test for the flatness of the solution space at the current iteration. As well, the size of the current step can be tested to see that progress towards a solution is being made, or a set limit of iterations has been exceeded. The convergence limits for the code tested here are given in Table 4.2, and convergence is said to be satisfied if any of the limits are met for all retrieved altitudes.

An example retrieval was performed by simulating OSIRIS measurement using SASKTRAN for typical atmospheric conditions with results shown in Figure 4.15, along with every second iteration

Table 4.2: Levenberg Marquardt convergence limits

Jacobian Norm	Step Size	Total Residual	Iteration Limit
10^{-5}	0.01%	10^{-4}	20

of the process. All atmospheric parameters except number density and mode radius were assumed to be correct for this test including the mode width of 1.6. Additionally, no noise was added to the simulated measurements. The geometry of this scan was chosen to have a scattering angle of 61° and a zenith angle of 72°. The *a priori* profile is the value retrieved using the MART technique and is the starting point for the Levenberg-Marquardt iterations. After ten iterations both extinction and mode radius have been retrieved with very little error above 15 km. Below 15 km the mode radius is overestimated by up to 10% due to the insensitivity of the measurement vectors at these altitudes.

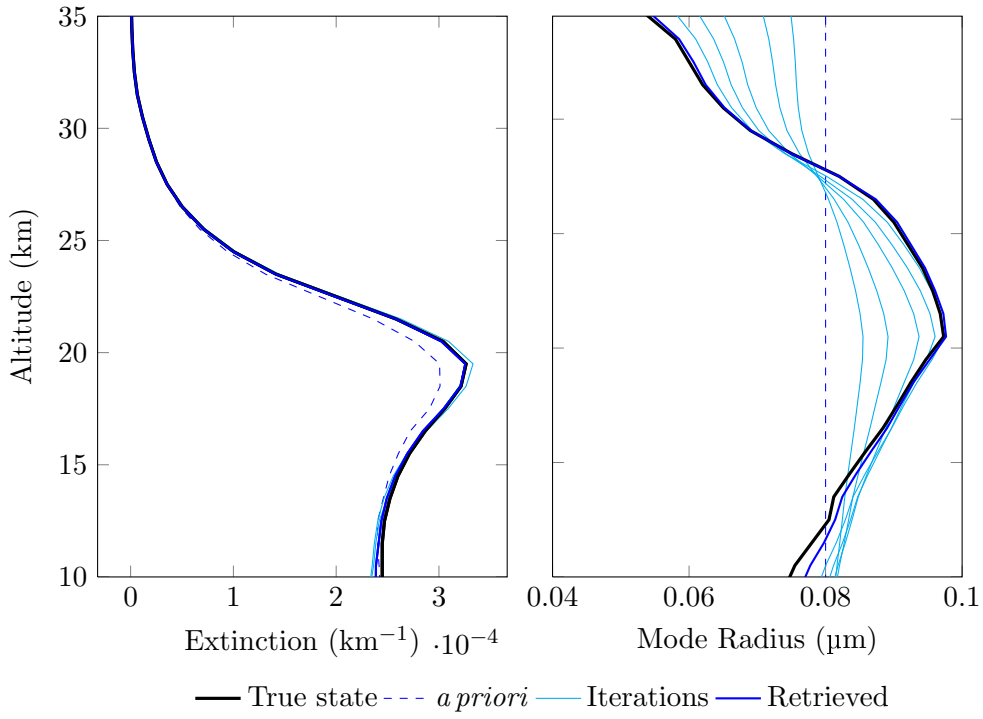

Figure 4.15: Example retrieval using simulated data. Retrieved extinction profile shown on the left and retrieved mode radius shown on the right. True state is shown in black with iterations shown in light blue and final retrieved value shown in dark blue. The *a priori* state is the result obtained using a MART retrieval with $r_g = 0.08\,\mu m$ and σ_g=1.6.

4.3 Retrieval Error

Although the solution spaces and example retrieval shown previously give an indication of the error of the retrieved aerosol parameters due to measurement noise and the algorithm itself, a more rigorous analysis is worth investigation. Several factors can introduce error and *Rodgers* (2000) broke the error involved in an atmospheric inversion into four components, each of which are discussed briefly below.

4.3.1 Forward Model Error

Forward model error results from the inaccuracies in the modelled measurements, due primarily to simplifications when solving the radiative transfer equation. Modelling limb scatter measurements is inherently a trade off between computational accuracy and computational time, and while great care has been taken to minimize the error, inevitably the model is merely an approximation to the physical system. For example, atmospheric refraction is not taken into consideration and causes an apparent shift of the tangent height. Near the ground, where atmospheric density is rapidly increasing, this effect is largest, causing a downward shift of approximately 2 km. However, the error rapidly decreases with altitude, approximately scaling with the atmospheric pressure (*Haley and Brohede*, 2007). More notable approximations involved in SASKTRAN are the assumptions of a horizontally homogenous atmosphere and computation of the diffuse profile at limited zenith angles. However, considerable care has been taken to minimize these errors, and SASKTRAN compares favorably to other radiative transfer models (*Bourassa*, 2007).

4.3.2 Measurement Error

Perhaps the most straightforward error is due to instrument noise propagating through the forward model into the retrieved quantity. This error can be broken into two components, a random error, δy_R, due to the measurement noise that is uncorrelated between altitudes and a systematic error, δy_S, due to the high altitude calibration that is entirely correlated between altitudes. The random error in the measurement vector y_k at altitude j can be determined from error in the spectral radiance measurement as

$$\delta y_{R_{kj}} = \frac{\delta I_j(\lambda_k)}{I_j(\lambda_k)}. \tag{4.23}$$

Since the high altitude normalization results in a shift of the measurement vector based on the spectral radiance measurements at high altitudes, the systematic error is the same for all altitudes

and given by

$$\delta y_{S_k} = \frac{1}{N}\sqrt{\sum_{j=m}^{m+N} \frac{\delta I_j^2(\lambda_k)}{I_j^2(\lambda_k)}}. \tag{4.24}$$

Following the error analysis by *Barlow* (1989, chap. 4.4) the random and systematic errors are independent and thus the total variance of a measurement vector at altitude j is simply the quadrature sum of both errors

$$\delta y_{kj}^2 = \delta y_{R_{kj}}^2 + \delta y_{S_k}^2. \tag{4.25}$$

The covariance of the errors can be found similarly, however the random errors will cancel, leaving only the squared systematic terms. The error covariance matrix, $\mathbf{S}_\epsilon$, for wavelength k can then be written

$$\mathbf{S}_{\epsilon_k} = \begin{pmatrix} \delta y_{R_{k1}}^2 + \delta y_{S_k}^2 & \cdots & \delta y_{S_k}^2 \\ \vdots & \ddots & \vdots \\ \delta y_{S_k}^2 & \cdots & \delta y_{R_{kj}}^2 + \delta y_{S_k}^2 \end{pmatrix}. \tag{4.26}$$

The measurement error for the optical spectrograph and infrared imager is quite different due to the measurement techniques. As the optical spectrograph is scanned vertically the exposure time can be increased, resulting in approximately the same number of photons being counted with each exposure; resulting in noise that increases only slightly with altitude, ranging from approximately 0.5-1% of the total signal. The IR channels image the entire vertical profile simultaneously, resulting in considerable noise at higher altitudes, typically on the order of 5%. This is exacerbated by the fact that approximately half the signal at the reference altitudes is from stray light, further increasing the relative error. Fortunately, the imager takes multiple profiles for each optical spectrograph scan, often 30 or more, which can be collapsed into an average profile to greatly reduce the error. Despite this averaging, error in the infrared channel still exceeds that of the optical spectrograph, with typical measurement vectors and errors shown in Figure 4.16.

The magnification of measurement vector error in the retrieved product can be determined by computing the gain matrix, $\mathbf{G}$, which maps a measurement vector to a particular atmospheric state

$$\hat{\mathbf{x}} = \mathbf{G}\mathbf{y}. \tag{4.27}$$

The error in $\hat{\mathbf{x}}$ resulting from the error in $\mathbf{y}$ is then

$$\delta\hat{\mathbf{x}} = \mathbf{G}\delta\mathbf{y}. \tag{4.28}$$

Note that this formulation linearizes the problem about the atmospheric state, $\hat{\mathbf{x}}$, and so is only valid for that particular state and if perturbations to $\hat{\mathbf{x}}$ due to measurement noise remain in an

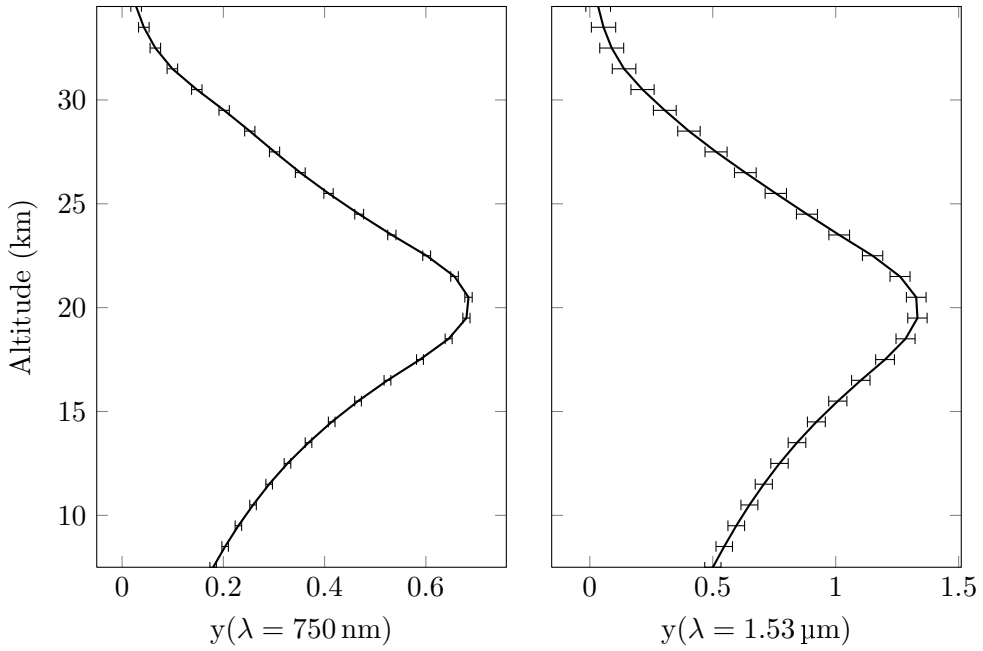

Figure 4.16: Measurement vectors shown with typical noise margins. Left panel is the 750 nm measurement and right panel is the 1.53 µm measurement after averaging of multiple profiles.

approximately linear region. Elements of the gain matrix can be computed numerically by using a measurement vector to retrieve an atmospheric state, then perturbing one element of the measurement vector and re-retrieving the state. Formulated this way $\mathbf{G}$ can be expressed as the derivative

$$\mathbf{G} = \frac{\partial \hat{\mathbf{x}}}{\partial \mathbf{y}}. \tag{4.29}$$

Figure 4.17 shows the gain matrices computed for the 750 nm measurement vector. For this computation a forward scatter geometry was chosen with a zenith angle of 89° and a scattering angle of 61° with the same aerosol profile as shown in Figure 4.15. The atmospheric state was retrieved before and after the measurement vector was perturbed by 3% at a single altitude to compute each column of $\mathbf{G}$. Fluctuations in the retrieved profile are highly localized to the altitude which is perturbed, with an increase in the 750 nm measurement vector resulting in an increase in extinction and decrease in particle size. Similarly, the gain matrix for the 1.53 µm measurement vector is shown in figure Figure 4.18.

The covariance matrix of the measured quantity is then

$$\mathbf{S}_m = \mathbf{G}\mathbf{S}_\epsilon\mathbf{G}^{\mathrm{T}}. \tag{4.30}$$

Although $\mathbf{S}_m$ may have significant off diagonal elements due to the non-diagonal nature of both $\mathbf{S}_\epsilon$

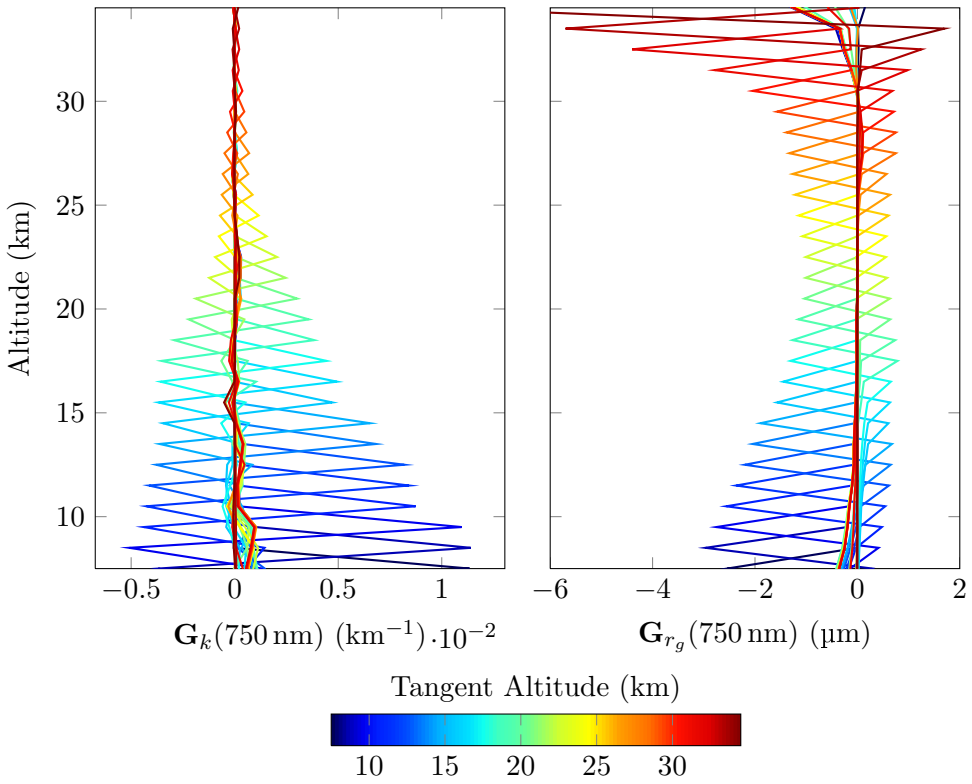

Figure 4.17: Gain Matrices for the 750 nm measurement vector.

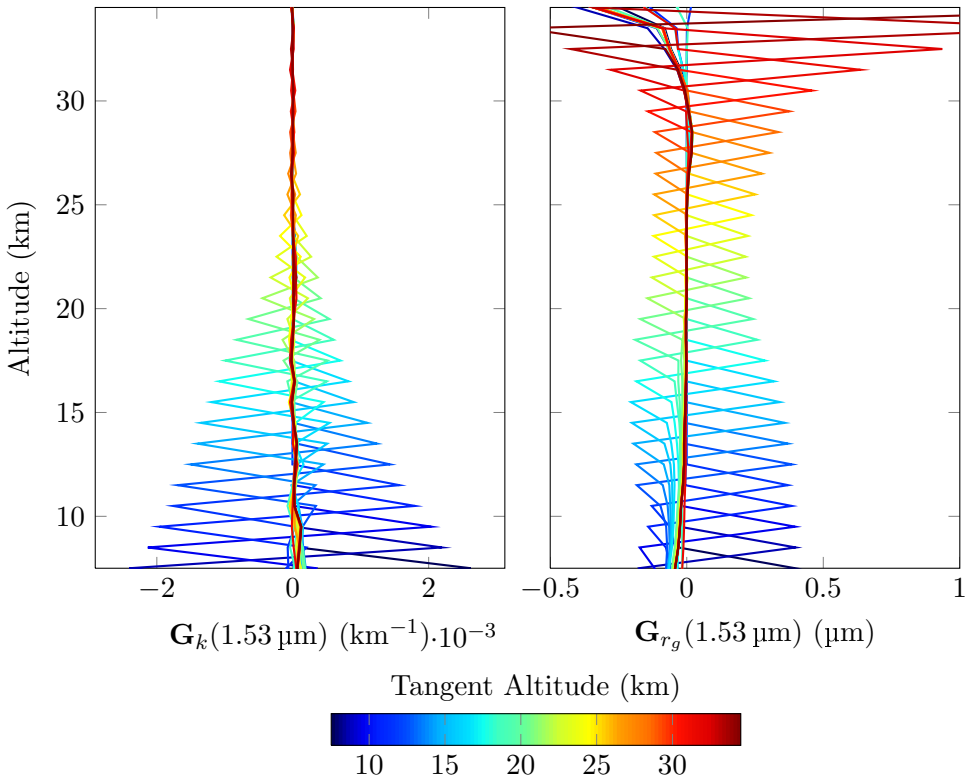

Figure 4.18: Gain Matrices for the 1.53 µm measurement vector.

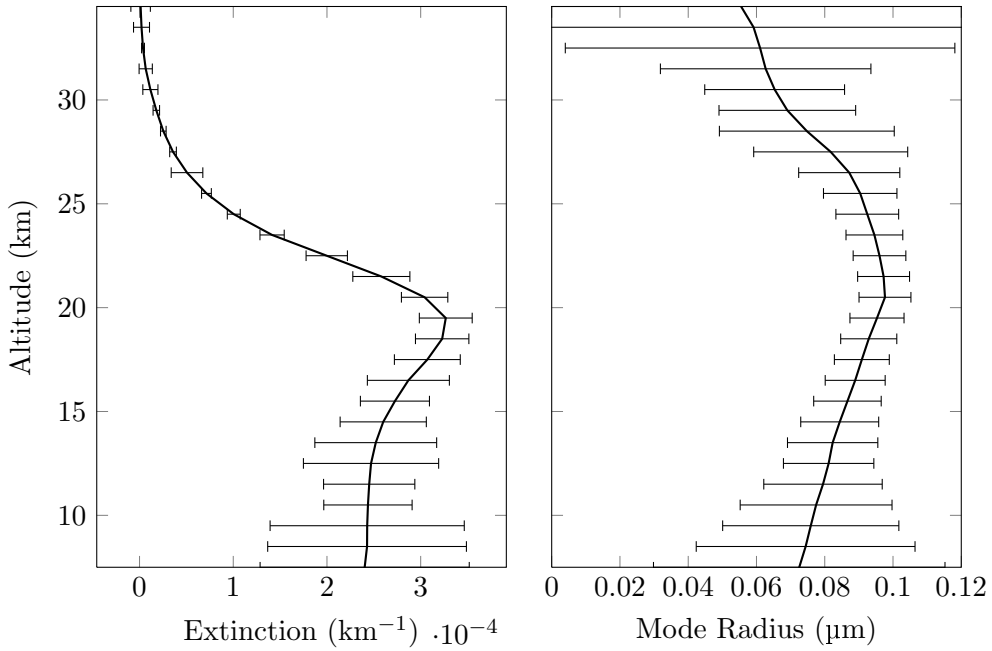

Figure 4.19: Error in the retrieval due to typical measurement noise.

and $\mathbf{G}$, these terms are difficult to quantify in terms of the real error associated with the retrieved quantities. For this reason the variance of each parameter, given by the diagonal elements of $\mathbf{S}_m$, is often used. Figure 4.19 shows the retrieved values of extinction and mode radius with these errors, given by the square root of the variance. At low altitudes the atmosphere is becoming optically thick, particulary at 750 nm, and small amounts of noise leads to large changes in the retrieved quantities. At higher altitudes the aerosol signal is small compared to the atmospheric signal and noise, particularly that due to the infrared imager, begins to dominate the retrievals, with errors exceeding 100% near 35 km.

4.3.3 Smoothing Error

Smoothing error results from the fact that measurements are not of a single point, but smoothed by an averaging kernel. Fluctuations in the true state with a higher resolution than the averaging kernel are thus undetectable, or largely so, and contribute to measurement error. This can be seen from computation of the averaging kernel, $\mathbf{A}$, which determines the change in the retrieved state for a change in the true state, or

$$\mathbf{A} = \frac{\partial \hat{\mathbf{x}}}{\partial \mathbf{x}}. \tag{4.31}$$

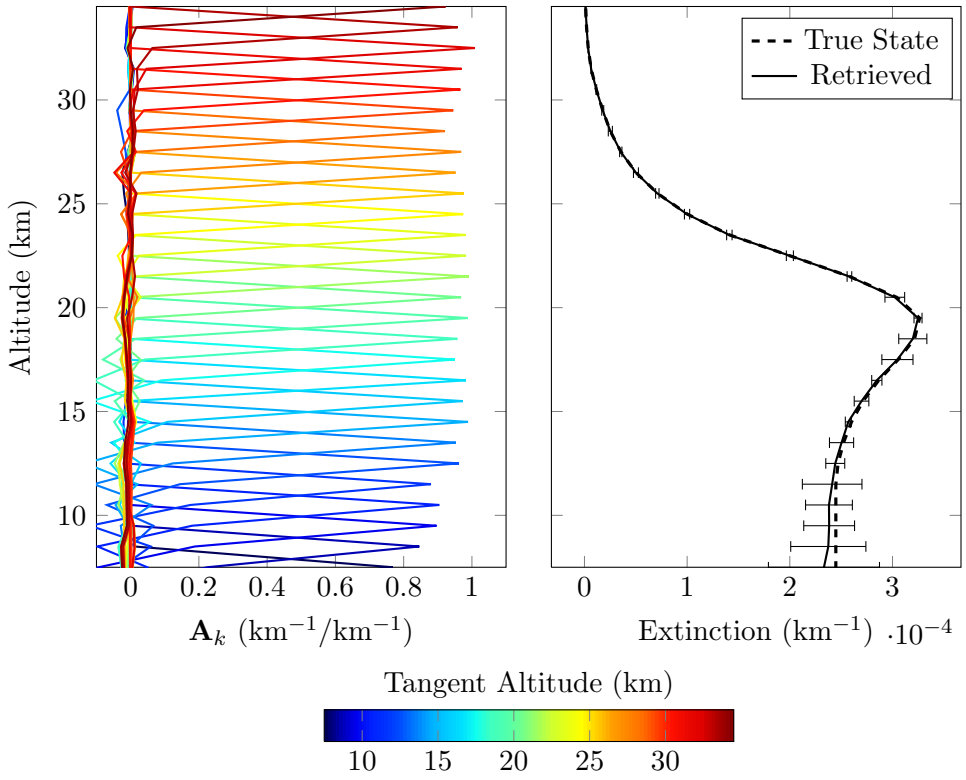

Figure 4.20: Extinction averaging kernel, $\mathbf{A}_k$ is shown in the left panel. The true and retrieved extinction profiles are shown in the left panel with error bars displaying the uncorrelated smoothing error.

The magnitude of the smoothing error, $\boldsymbol{\epsilon}_s$, is then

$$\boldsymbol{\epsilon}_s = (\mathbf{A} - \mathbf{I})(\mathbf{x} - \mathbf{x}_a). \tag{4.32}$$

The magnitude of the error is dependent on how sensitive the retrieval is to a perturbation of a single altitude, but also how much the retrieved profile must be shifted from the *a priori* state. The averaging kernels for the geometry studied in the previous section were computed by successively perturbing the atmospheric state variable at a particular altitude and performing an extinction and mode radius retrieval. Figure 4.20 shows the averaging kernel for a 3% perturbation to the extinction in the left panel. Except at very low altitudes the averaging kernel is very nearly the identity matrix, indicating a small smoothing error. The right panel shows the true and retrieved profiles with uncorrelated smoothing error. The uncorrelated smoothing error is calculated as the diagonal elements of $(\mathbf{A} - \mathbf{I})$ multiplied by the difference between the *a priori* and retrieved states, $(\mathbf{x} - \mathbf{x}_a)$. For this calculation the *a priori* extinction profile is assumed to be zero, as the MART retrieval has its own smoothing error and little is known about the shape and magnitude of the true extinction. This creates a typical smoothing error of less than 5% for most altitudes, although this

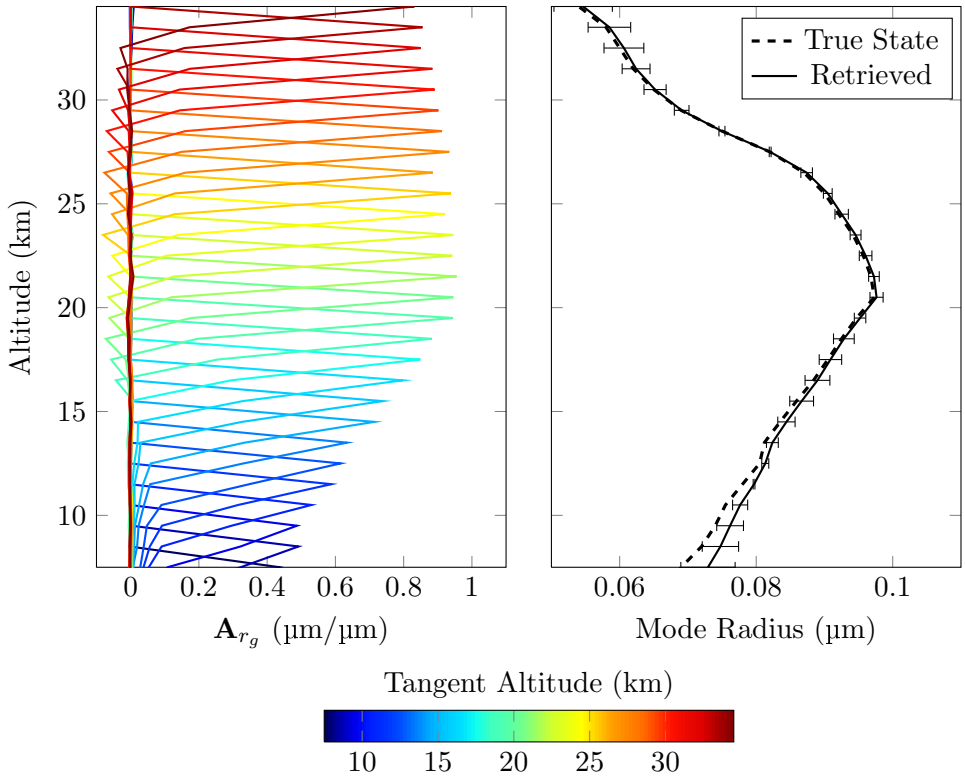

Figure 4.21: Mode radius kernel, $\mathbf{A}_{r_g}$ shown in the left panel. The true and retrieved mode radius profiles are shown in the left panel with error bars displaying the uncorrelated smoothing error.

increases to more than 10% below 10 km.

Figure 4.21 shows the same picture for the smoothing error in the retrieved mode radius. This averaging kernel is a much poorer approximation to the identity matrix with altitudes below 20 km exhibiting significant smoothing. However, due to the better *a priori* estimate the mode radius smoothing error is still limited to less than 5%.

4.3.4 Model Parameter Error

Another error in the retrieved quantities is due to incorrect assumptions about the other atmospheric parameters. While these include everything from temperature and pressure profiles to ozone concentrations, the two that have the largest affect on the particle size retrieval are the albedo and the particle size assumptions.

Currently, albedo is retrieved at 675 nm by modelling the OSIRIS signal at the normalization altitude for several different albedo values. The albedo is then found through linear interpolation between the two values which produce the closest modelled spectral radiance to the OSIRIS signal.

The albedo signal looks very similar to that of aerosol with a broad spectral response and general increase in the measured spectral radiance, thus retrieving albedo correctly is important for accurate aerosol retrievals. Currently, the albedo at 750 nm is taken to be the same as that at 675 nm. While vegetation can have a sharp change in reflectance near these wavelengths, known as the red edge (*Horler et al.*, 1983), typical geographic features do not (*Gao et al.*, 2002; *Grenfell et al.*, 1994; *Knyazikhin et al.*, 1998; *McLinden et al.*, 1997), and extrapolation of albedo over 75 nm provides good results.

The albedo retrieval technique implemented at 675 nm works well, unfortunately it cannot be extended to the infrared imager due to lack of an absolute calibration. A brief discussion of possible solutions to this is discussed in Appendix A; however, the current solution is the assumption that albedo is unchanged from 675 nm to 1.53 µm. While this assumption is certainly incorrect to some degree, it is further complicated by the presence of a water vapour absorption band at 1.44 µm which extends slightly into the 1.53 µm detector's range. At stratospheric altitudes the water vapour mixing ratio is small, approximately 5 ppm (*Chiou et al.*, 1997), limiting the error in spectral radiance to less than that of measurement noise. At low altitudes, water vapour can compose a substantial portion of the atmosphere, on the order of 1%, and ignoring water vapour is no longer valid. While retrievals are not performed at these low altitudes, upwelling radiation in the water absorption bands will be systematically reduced, causing a reduction in the apparent albedo when compared to wavelengths outside of the absorption band. This likely leads to a systematic overestimation of the 1.53 µm albedo, although the amount will vary depending on atmospheric and ground conditions.

The magnitude of this error on the retrieved parameters can be determined in a similar fashion to the other error quantities through the formula

$$\boldsymbol{\epsilon}_b = \mathbf{G}\mathbf{K}_b(\mathbf{b} - \hat{\mathbf{b}}). \tag{4.33}$$

However, unlike measurement noise and smoothing errors, the error in albedo may be large, and the assumption that the forward model remains linear in the region of interest may be violated. A more accurate estimate of the error can be obtained by simulating retrievals with incorrect albedo values. Figure 4.22 shows the retrieved extinction and mode radius values for three cases where the true 1.53 µm albedo is 0.0, 0.5 and 1.0, while the assumed albedo is constant at 0.5. Both the true and assumed albedos for the 750 nm measurements are constant at 0.5 as well. The geometry of this scan was chosen to have a zenith angle of 72° and a scattering angle of 119° creating a

relatively large albedo contribution to the total signal. If the true albedo is underestimated the measurement vector is systematically too large, leading to an increase of both particle size and extinction. For the geometry and cases tested the error due to incorrect albedo is approximately 15% for extinction and 30% for mode radius near the peak aerosol concentrations. The effect is also non-linear, with overestimation causing a larger error in both retrieved extinction and mode radius than underestimation. Note that this is close to a worst case, with albedo error of forward geometries for the same atmospheric conditions limited to less than 5% for both parameters.

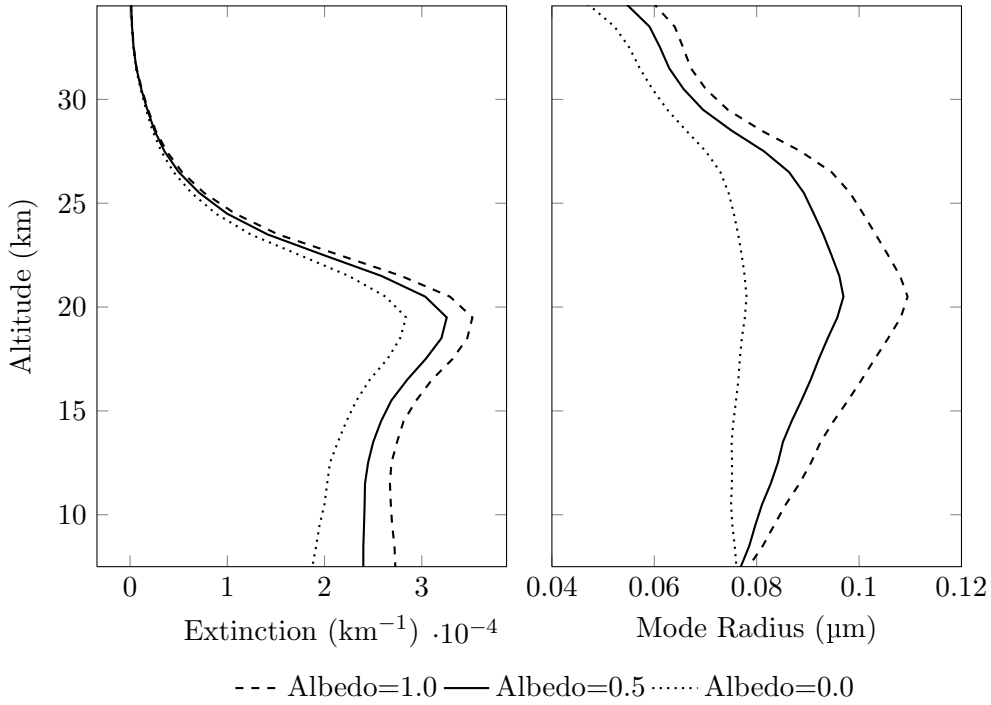

Figure 4.22: Error in the retrieval due to assumption that albedo is constant with wavelength.

The error, in percent of retrieved value, due to these terms is summarized in Figure 4.23, with the total error shown as the quadrature sum of the error components. At altitudes above 30 km and below 15 km error begins to dominate the signal, with virtually all of the error due to measurement noise. In the bulk of the aerosol layer this error reduces to approximately 10% for both retrieved quantities. The error budget is primarily due to the 1.53 µm measurements, which are approximately 5-10 times noisier than the 750 nm measurements. If error in the retrieved quantity is hoped to be reduced, more accurate infrared measurement are needed.

The error due to incorrect assumptions about the particle microphysics is more difficult to quantify in this manner, due to the number of variables and possible values involved. However, it

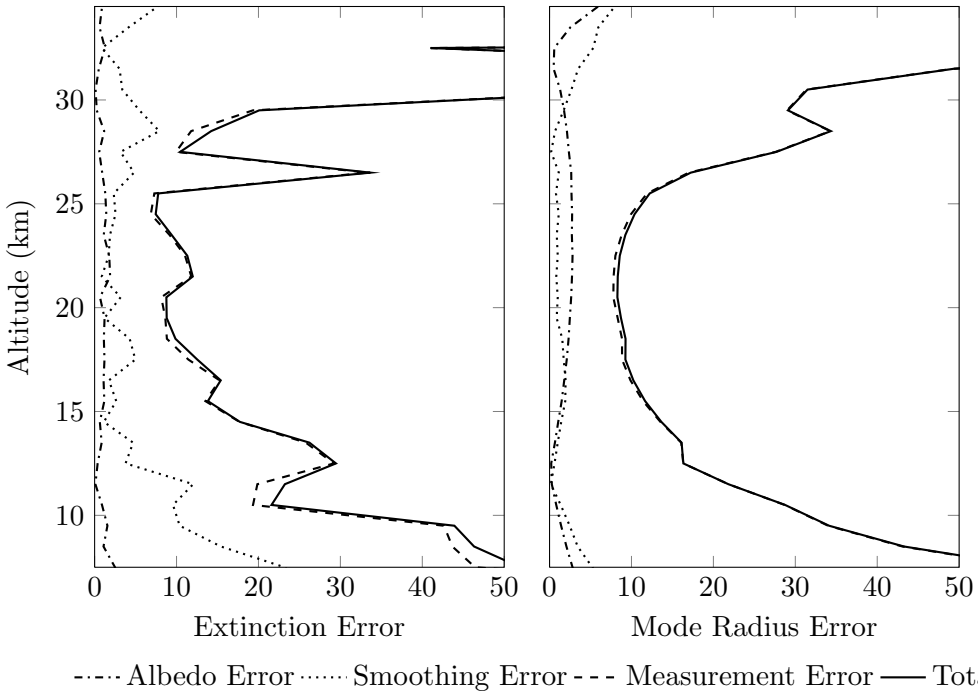

Figure 4.23: Total error in the retrieved quantities due to albedo, smoothing and measurement error contributions.

remains an important factor in determining the quality of the retrievals and the amount of error can be gauged by studying the retrieval of an atmospheric state where the microphysical assumptions have been violated. To test reasonably worst-case scenarios the simulated atmosphere was assumed to be largely bimodal at lower altitudes, with coarse particles contributing approximately 50% of the overall extinction. The coarse mode fraction was decreased with altitude to simulate the sedimentation of larger particles, leading to an extinction due almost entirely to fine particles by 30 km. The fine mode parameters were also assumed incorrectly for the retrievals, with exact parameters given in Table 4.3. Retrieval of this extinction profile was attempted for two different OSIRIS scan geometries with results shown in Figure 4.24. The MART retrieval, shown in red, with an assumed mode radius of 80 nm and mode width of 1.6 systematically underestimates the true extinction at low altitudes due to the inclusion of large particles, but is more accurate at high altitudes where the fine mode dominates, despite lognormal parameters that differ from the true state. The coupled retrieval of both mode radius and extinction, shown in blue, provides substantially better results, with only a slight underestimation of the true extinction.

The second retrieved quantity, mode radius, can then be converted to an Ångström exponent. Figure 4.25 shows the retrieved Ångström coefficients for the same two cases studied above. While

Table 4.3: Lognormal size parameters used in the simulated retrievals

Mode	MART Retrieval	Coupled Retrieval	True State
Fine Mode	$r_g = 80\,\text{nm}$ $\sigma_g = 1.60$	r_g = retrieved $\sigma_g = 1.60$	$r_g = 90\,\text{nm}$ $\sigma_g = 1.75$
Course Mode	None in model	None in model	$r_g = 400\,\text{nm}$ $\sigma_g = 1.20$

the retrieved quantities are typically too large, both indicate that the *a priori* particle size used in the MART retrieval is too small and move to correct the problem by adding larger particles. The dependence on geometry and *a priori* assumptions however, make the error in this parameter larger than that of the retrieved extinction. This is particularly true near 20 km altitudes where the coarse mode particles account for more than half of the total extinction.

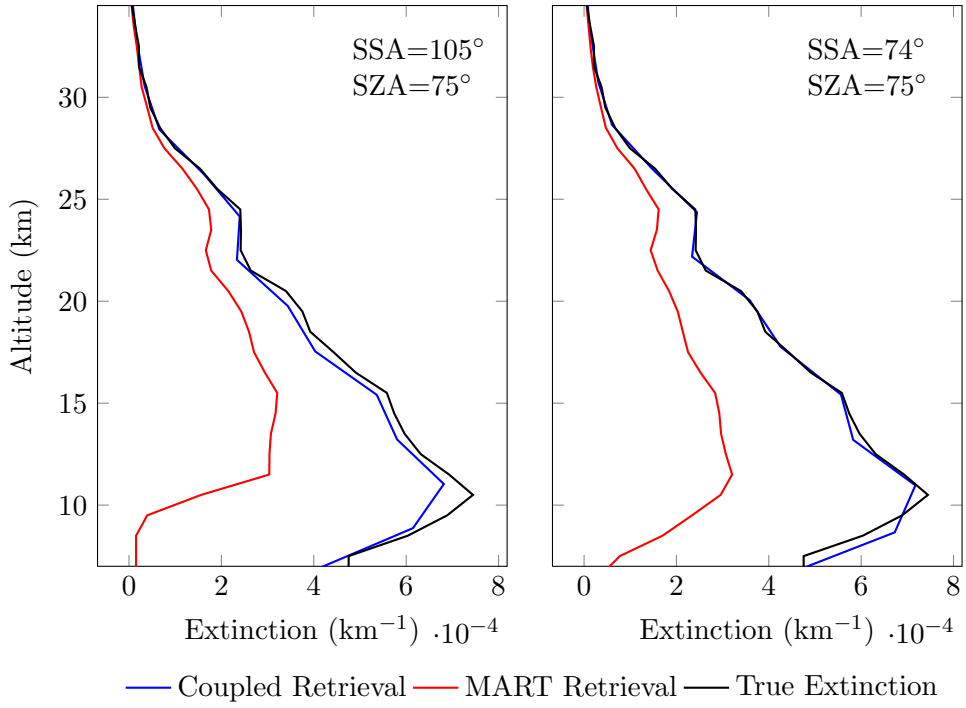

Figure 4.24: Two simulated retrievals comparing the coupled extinction and mode radius technique (blue) and MART (red) for two geometries. True state is heavily bimodal with the true extinction shown in black.

This analysis can be extended to test a wider range of geometries by simulating several hundred OSIRIS scans. This allows for a wide range of scattering and zenith angles as well as testing

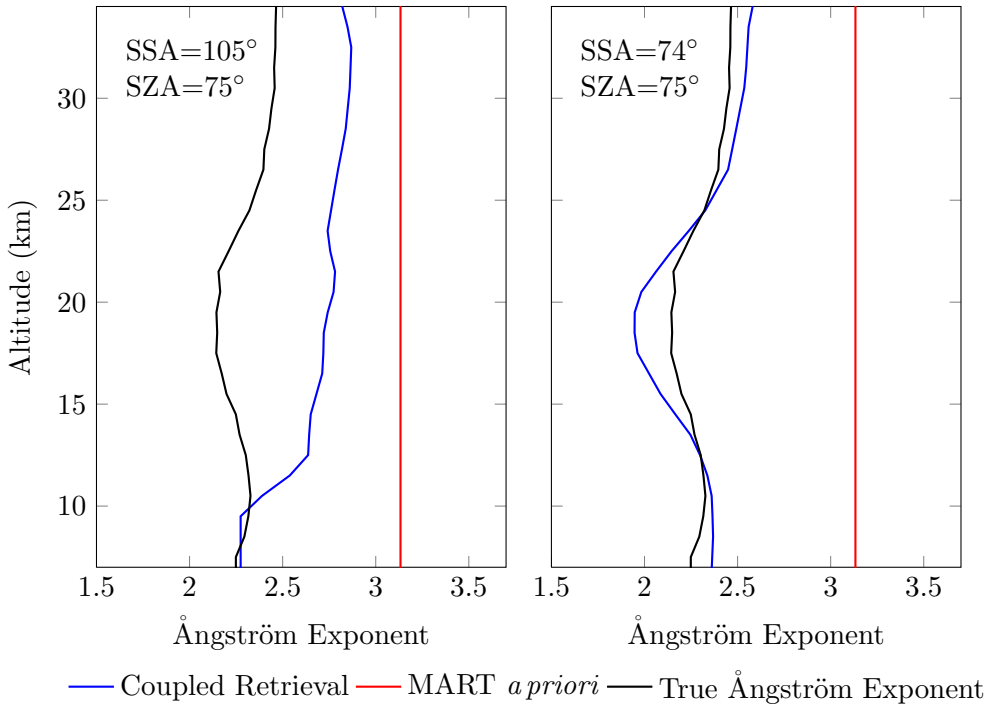

Figure 4.25: Comparison of the true and retrieved Ångström coefficients using the mode radius technique. The assumed Ångström coefficient used for the MART retrievals is shown in red for comparison.

real geometries where problems have presented in the past (see Section 3.1). Using the same atmospheric state as the simulation described in Table 4.3 both MART and coupled techniques were used to retrieve the extinction profiles for 765 OSIRIS geometries. The percent difference between the retrieved and true states is shown in Figure 4.26. Again, the MART retrieval systematically underestimates the extinction for all geometries by up to 40%, with a clear dependence on the scattering angle. Retrieving mode radius with extinction removes much of the bias, although some dependence on scattering angle is still apparent, with typical errors in the 10-20% range.

4.4 Conclusions

Through exploitation of the Odin orbit, it is possible to derive four aerosol measurement vectors at each tangent altitude. However, the information added by incorporating matching pair scans into a single measurement is small, and difficult to access even for reasonable instrument noise. While this makes determination of three aerosol parameters difficult to impossible, the behavior of the solution space yields the possibility of using only one geometry and two wavelengths to retrieve an improved extinction quantity coupled with a particle size parameter. By assuming a unimodal lognormal size

distribution with a set mode width, searching the solution space with the Levenberg-Marquardt can yield greatly improved extinctions, as well as information on particle size, although this quantity is biased by both incorrect size distribution assumptions and measurement geometry.

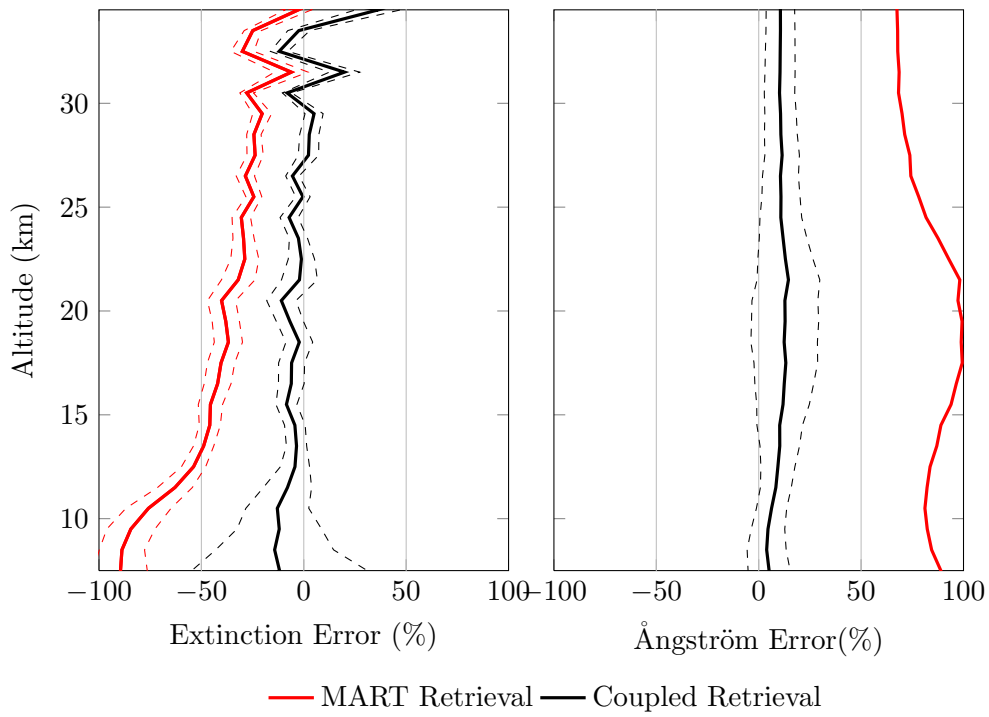

Figure 4.26: Error in the retrieved parameters under a variety of simulated measurement conditions when the true atmospheric state is bimodal. Error using the coupled extinction and mode radius retrieval are shown in black with dashed lines showing the standard deviation. MART results are shown in red for comparison.

Chapter 5

Results

In chapter 4 a technique was determined to retrieve both mode radius and extinction provided a unimodal distribution with a set mode width was assumed. In simulations this produced an improved aerosol extinction product as well as information on particle size when the mode radius was converted to an Ångström coefficient. To provide a suitable wavelength range and sensitivity the analysis utilized the 750 nm channel of the optical spectrograph and the 1.53 µm channel in the Infrared Imager. While the optical spectrograph measurements are currently of high caliber and used for numerous retrieved products, the Infrared Imager has not been used in an operational sense, and suffers from calibration, stray light and altitude registration issues. While many of these problems have been tackled previously with large degrees of success (*Bourassa*, 2003), stray light and altitude registration still pose a problem for aerosol retrievals. The detailed correction of these issues is covered in Appendix A and allows for the use of the 1.53 µm infrared channel in the aerosol retrieval. For reference, Figure 5.1 illustrates the difference in 1.53 µm measurement vectors before and after stray light removal. Before removal, stray light dominates the signal above 33 km, causing a low reference altitude and small measurement vector, so much so that below 17 km the measurement vector becomes negative. This implies that so much aerosol is present the atmosphere has become optically thick and the signal has fallen below that of the modelled Rayleigh scattering, a physically implausible scenario for background loading conditions and stratospheric altitudes measured at infrared wavelengths. After stray light removal the measurement vector is much more physically realistic, with a large reference altitude range and reasonable magnitude.

With stray light removed the aerosol retrievals can proceed and an example of the retrieval process is shown in Figure 5.2. This shows measured and modelled measurement vectors for scan 42109018. Using the a priori particle size the 1.53 µm measurement vector is systematically too large, despite good agreement with the 750 nm measurement vector. To correct this the algorithm decreases both the mode radius and extinction until both modelled values match the measurements. The retrieved values for this scan are shown in Figure 5.3. The retrieved mode radius is a typical

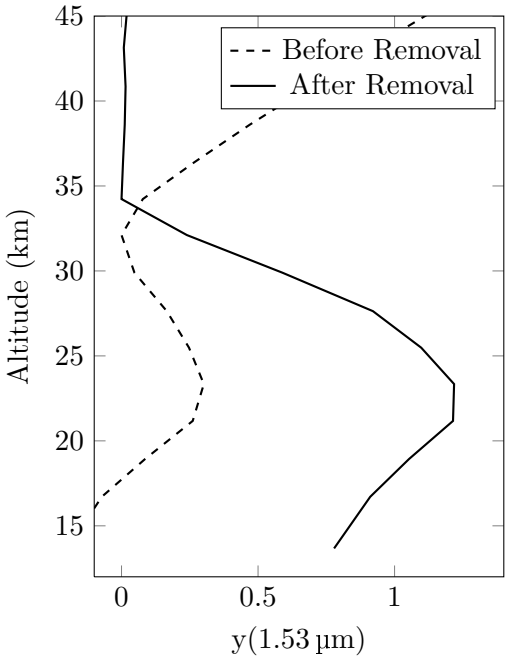

Figure 5.1: 1.53 µm measurement vector before stray light removal shown as dashed line, and after stray light removal shown as solid line for scan 42109018.

result with generally decreasing particle size with altitude. This results in a decrease in the retrieved extinction by 10-25% depending on the altitude.

The problems in the operational aerosol retrievals due to particle size were apparent from the comparisons done in chapter 3, and presented in a systematic difference in the retrievals based on measurement geometry (Figure 3.2), a seasonal enhancement not measured by SAGE II and CALIPSO (Figure 3.3), and a slight bias in the SAGE III comparisons in 2005 (Figure 3.4). Any improved retrieval must therefore correct these issues to be considered successful. The sections below discuss the results of this technique applied to OSIRIS data, both to the retrieved extinction and particle size.

5.1 Particle Size Retrieval

Determination of the quality of the retrieved particle size can be tested through comparison with other data sets. While high accuracy of this quantity is not expected, due to the assumptions about the size distribution and the dependence on measurement geometry, qualitative agreement between large scale features such as those appearing after volcanic eruptions should be apparent. Particle size measurements, particularly on a large scale, are not regularly produced, with one of the most

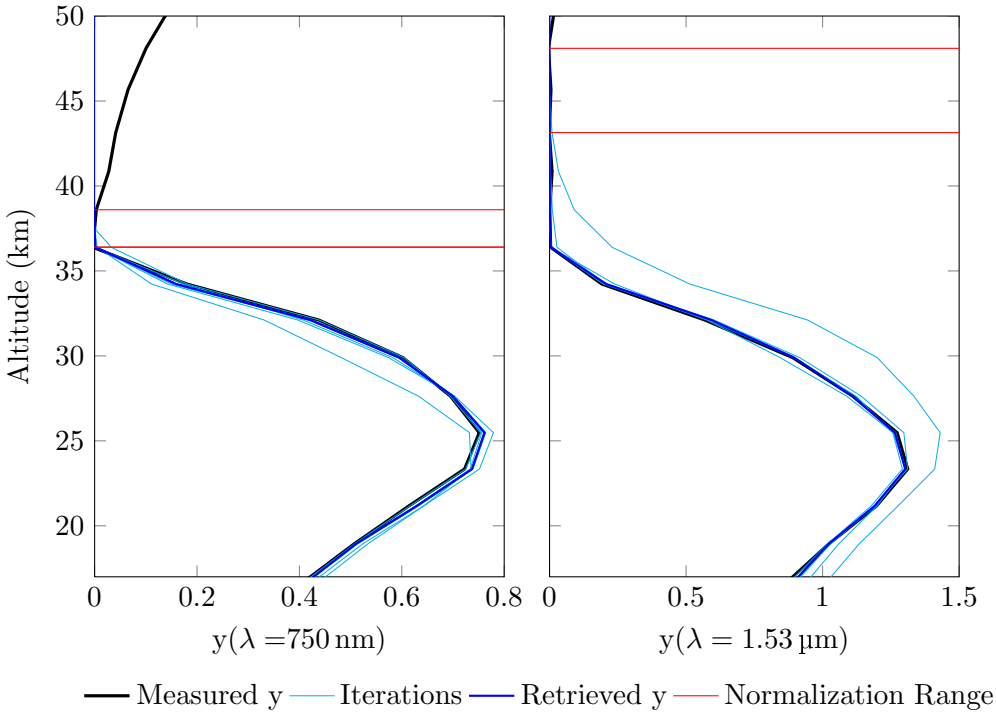

Figure 5.2: Example of the retrieved and measured vectors for scan 42109018.

comprehensive data sets coming from SAGE II. SAGE II produced high quality measurements for the duration of its lifetime with the 525 and 1020 nm channels agreeing well with SAGE III, with typical uncertainties less than 15% for the majority of the aerosol layer (*Yue et al.*, 2005).

SAGE II was launched in 1985, and continued operating until mid 2005, providing approximately three years of overlap with the OSIRIS mission. This period also contains two volcanic eruptions: Mts. Ruang and Reventador in 2003, and Mt. Manam in 2005, providing a good test of the OSIRIS particle size retrieval. Figure 5.4 shows the retrieved Ångström coefficients in 45 day averages from the SAGE II and OSIRIS satellites in the tropics for 2002 through 2005. In general both show an Ångström coefficient increasing with altitude. This is expected as larger particles tend to sediment to lower altitudes. Somewhat counter-intuitive however, is the increase in Ångström coefficients after the Ruang/Reventador and Manam eruptions. This suggests a decrease in particle size despite an increase in extinction. One possible explanation for this may be due to the relatively small size of the eruptions causing an increase in SO_2 concentrations and nucleation particulate without a large decrease in the mean free path of the particles; essentially enhancing nucleation to a larger degree than coagulation.

Although large scale features agree qualitatively, OSIRIS retrieves a systematically higher Ångström coefficient, particularly at lower altitudes. Some of this discrepancy is due to the differences in wave-

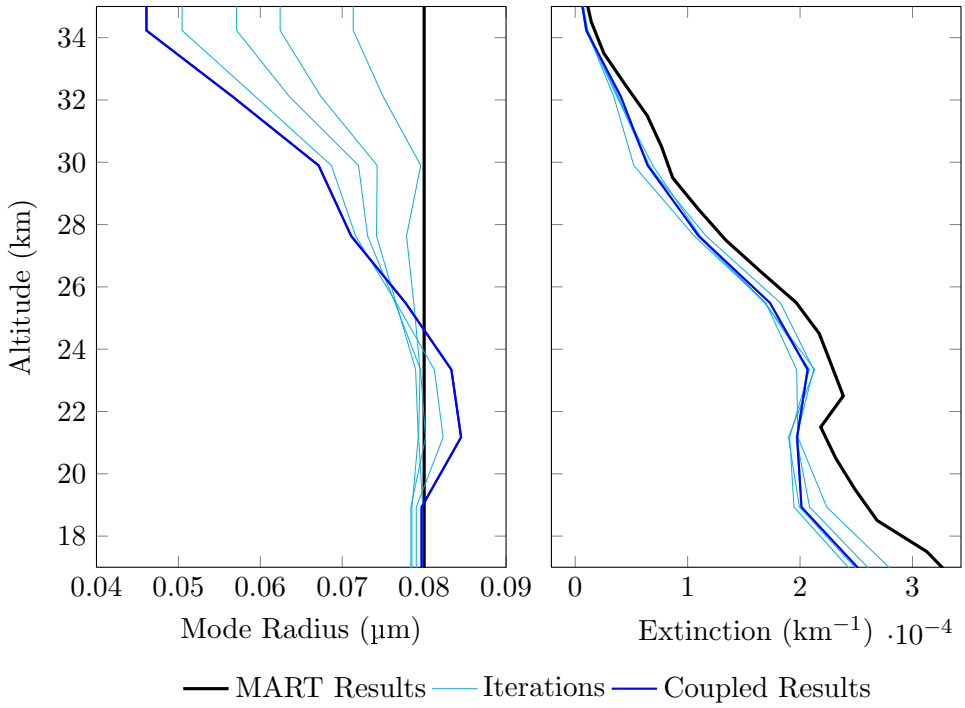

Figure 5.3: Example of the retrieved parameters for scan 42109018.

length between the two satellites. The longer OSIRIS wavelengths become optically thick at much lower altitudes, increasing sensitivity. Also, although extinction is an approximately linear function of wavelength (in log space) this is not strictly true and causes a dependency of the Ångström coefficient on the wavelengths chosen. Figure 5.5 shows the Ångström coefficient as a function of particle radius based on the SAGE II and OSIRIS wavelengths. For very small particles ($r \lesssim 100$ nm) the Ångström coefficients of both wavelength ranges approach the Rayleigh limit of four, indicating that at high altitudes, where particles are expected to be small, agreement should be good, as is the case. For larger particles ($r \lesssim 1$ µm) however, the 525/1020 nm ratio is considerably smaller than the 750/1530 nm ratio, indicating that where larger particles are present the Ångström coefficient derived from SAGE II should be systematically smaller than those from OSIRIS. While the wavelength difference accounts for much of the discrepancy some is likely due to the particle size assumptions, including the choice of a unimodal lognormal distribution and particular mode width. Overall though, the agreement suggests the use of the 1.53 µm measurements in the retrieval greatly improves the sensitivity to particle size, providing at least qualitative information on the Ångström coefficient.

As a second comparison of the SAGE II and OSIRIS particle size retrievals, the circulation and evolution of the volcanic particles can be examined through zonal averages before and after

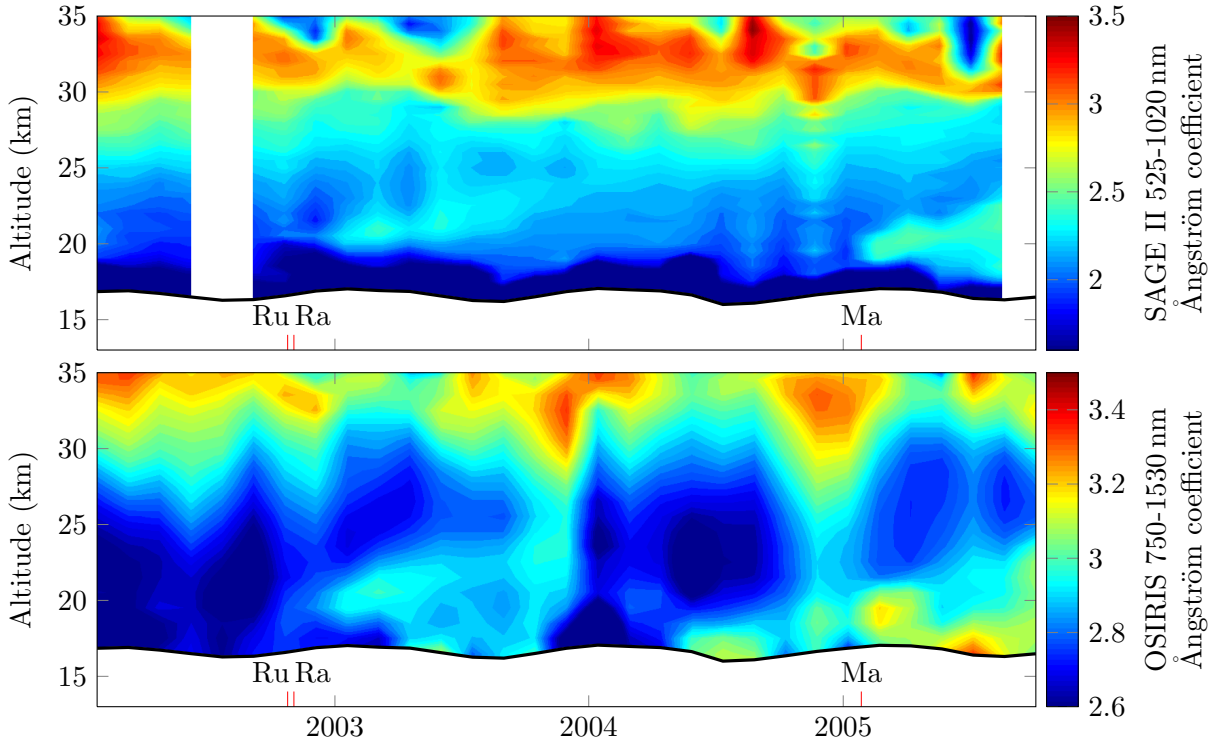

Figure 5.4: Comparison of the retrieved Ångström coefficients from SAGE II in the top panel, and OSIRIS in the bottom panel. Tropopause is denoted by the black line.

the Mt. Manam eruption. Manam is located at 5° South and erupted on January 27th, 2005, injecting ash and SO_2 up to 22 km in altitude (*Carn et al.*, 2008; *Clerbaux et al.*, 2008). As seen in Figure 5.6, before the eruption a relatively smooth picture of particle size develops with larger particles present at lower altitudes and near the tropics. After the eruption SAGE II measures a thin band of smaller particles in the tropics near the upper altitudes of the aerosol plume. Although OSIRIS Ångström measurements also see a decrease in particle size after the eruption, this plume of small particles has a larger vertical extent, stretching to the tropopause. This is similar to the previous comparison, in which enhancements were seen at lower altitudes and is likely due to both the difference in wavelengths of the two instruments as well as the decreased vertical resolution of OSIRIS compared to SAGE II.

Also visible in the OSIRIS measurements is a shift in the Ångström coefficients near the mid latitudes. This is likely caused by the incorrect particle size assumptions, which present in a systematic shift in the retrieved Ångström coefficient dependent upon the viewing geometry. Although unfortunate, this behavior is expected both from the solution space analysis and the simulated retrievals.

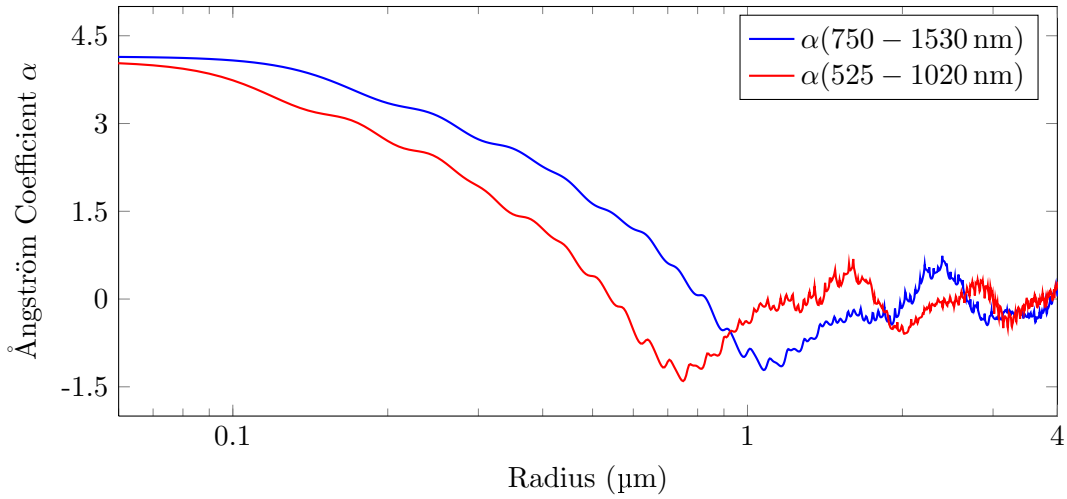

Figure 5.5: Ångström coefficient as a function of particle radius for the SAGE II and OSIRIS wavelengths.

5.2 The Scattering Angle Dependence

One of the main tests that suggested a particle size problem was the comparison of retrieved extinction values at similar locations and times but different scattering angles. Figure 5.7 shows the daily averaged 750 nm extinction ratio from 10°N to 10°S retrieved using the MART method and the coupled particle size/extinction technique from 2002 through 2009. To improve the computation time, only every 10^{th} scan was processed. While the scattering angle dependence is clear when particle size is assumed, it is almost completely removed when particle size is folded into the retrieval. While a small amount of yearly variation still exists, this may now be due to physical changes in the stratosphere rather than a scattering angle dependence. As well, the improved agreement between ascending and descending node measurements verifies that little information is left to be extracted by comparison of these two geometries. Although much of the systematic bias has been removed from this data set, each individual measurement now appears noisier. This is due to the inclusion of the infrared data which has considerable noise even after relative calibration and stray light removal.

5.3 SAGE III Recomparison

The accuracy and precision of the retrieved extinction using the new technique can be tested against the SAGE III data set. Using the same coincident criteria and set of scans as in Figure 3.4 the difference between SAGE III and the new and old retrieval techniques is shown in Figure 5.8.

The particle size retrieval removes much of the low altitude bias, particularly in 2005, after the Mt. Manam eruption. However, the increased noise is also apparent in the increased standard deviation, particularly at higher altitudes.

5.4 Extinction Ratio Time Series

The particle size and thus scattering angle dependence also exhibited in the extinction time series, particularly when compared to the similar SAGE II/CALIPSO measurements. Figure 5.9 shows the 10 day average extinction ratio retrieved from 10°N to 10°S using the MART and coupled techniques; again every 10^{th} scan was used. The major tropical eruptions are labeled as well as the Australian wildfires (Vi*). The large enhancements occurring at the beginning of 2005, 2008 and 2009 are now gone. As well, the earlier years now agree much better with the SAGE II time series shown in Figure 3.3. The extinction ratio is generally higher at lower altitudes near the tropopause, this is primarily due to the lower bound of the MART technique which as has not yet been incorporated in the coupled retrieval, resulting in high altitude clouds being included in the retrieval. While clouds are the primary driver of this low altitude enhancement the inclusion of the 1.53 µm channel also allows for the retrieval of higher aerosol concentrations before the atmosphere becomes optically thick and retrievals fail. This may bias the MART technique to lower aerosol values to a larger degree than the coupled retrievals which incorporates the longer wavelength. This affect is most noticeable at lower altitudes where the thicker neutral atmosphere is already approaching optically thick values and likely contributes to the larger extinction seen near the tropopause.

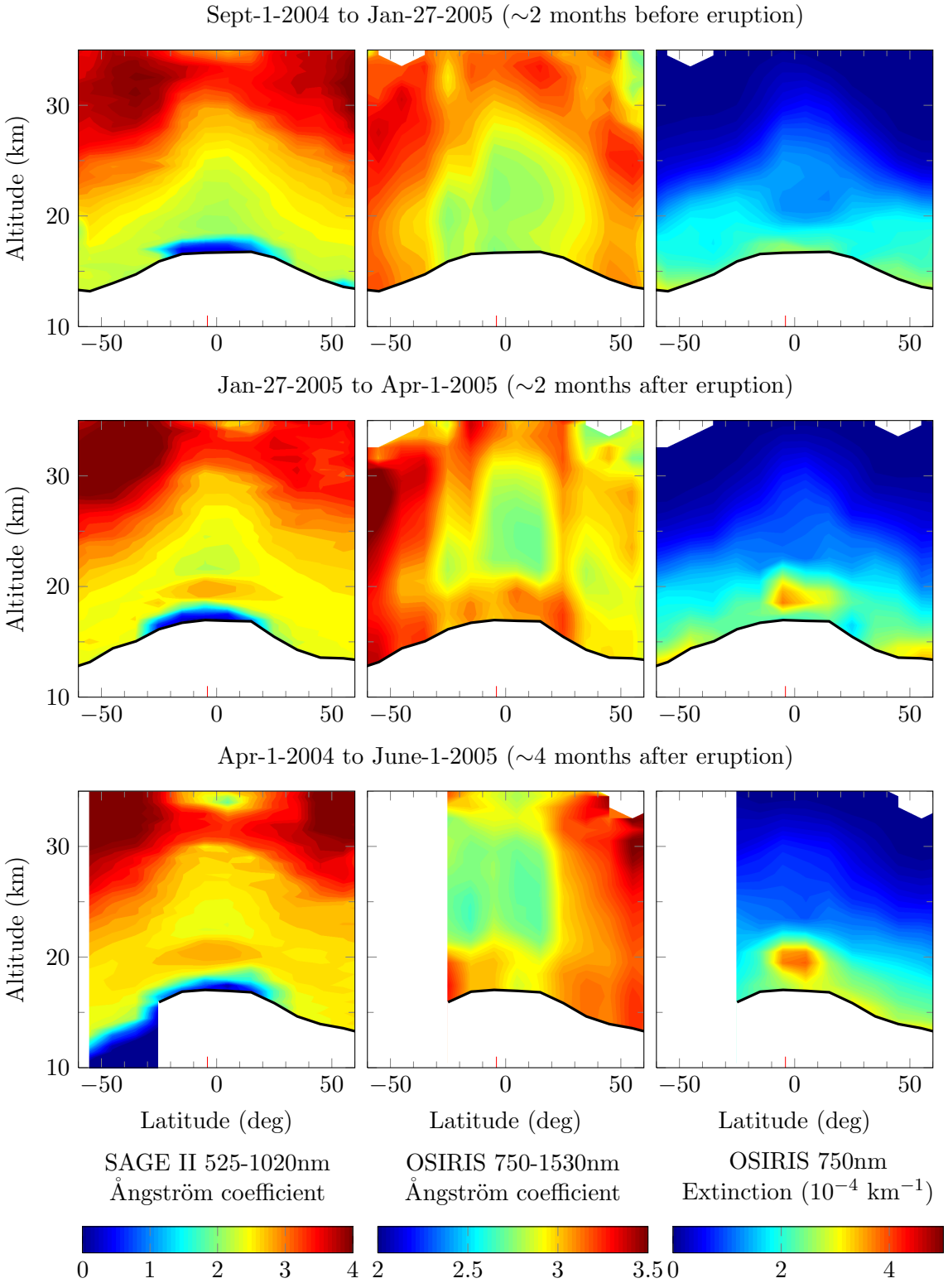

Figure 5.6: SAGE II Ångström coefficients retrieved before and after the Mt. Manam eruption shown in left column. Center column is the Ångström coefficients retrieved by OSIRIS for the same time periods. Shown in the right column are 750 nm extinction values retrieved by OSIRIS.

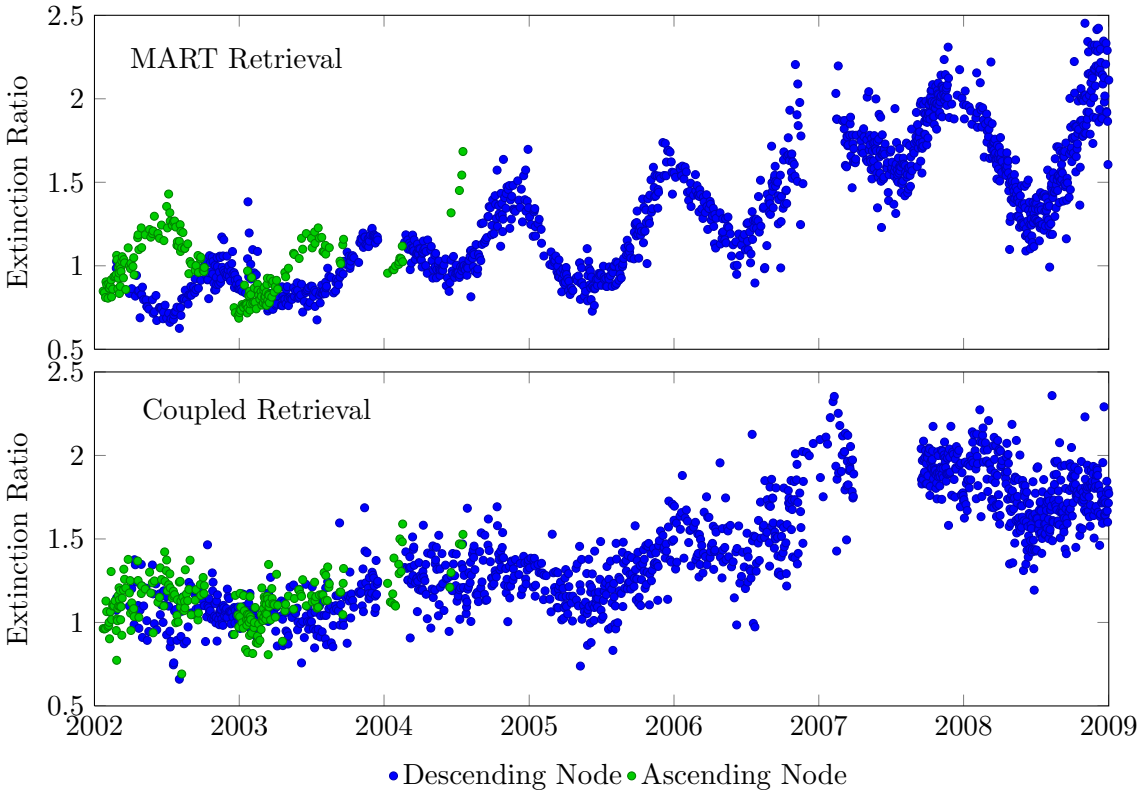

Figure 5.7: Daily averaged extinction ratio between 10°S and 10°N between 23 and 28 km. Results from the MART retrieval are shown in the top panel with coupled mode radius and extinction retrieval shown in the bottom panel.

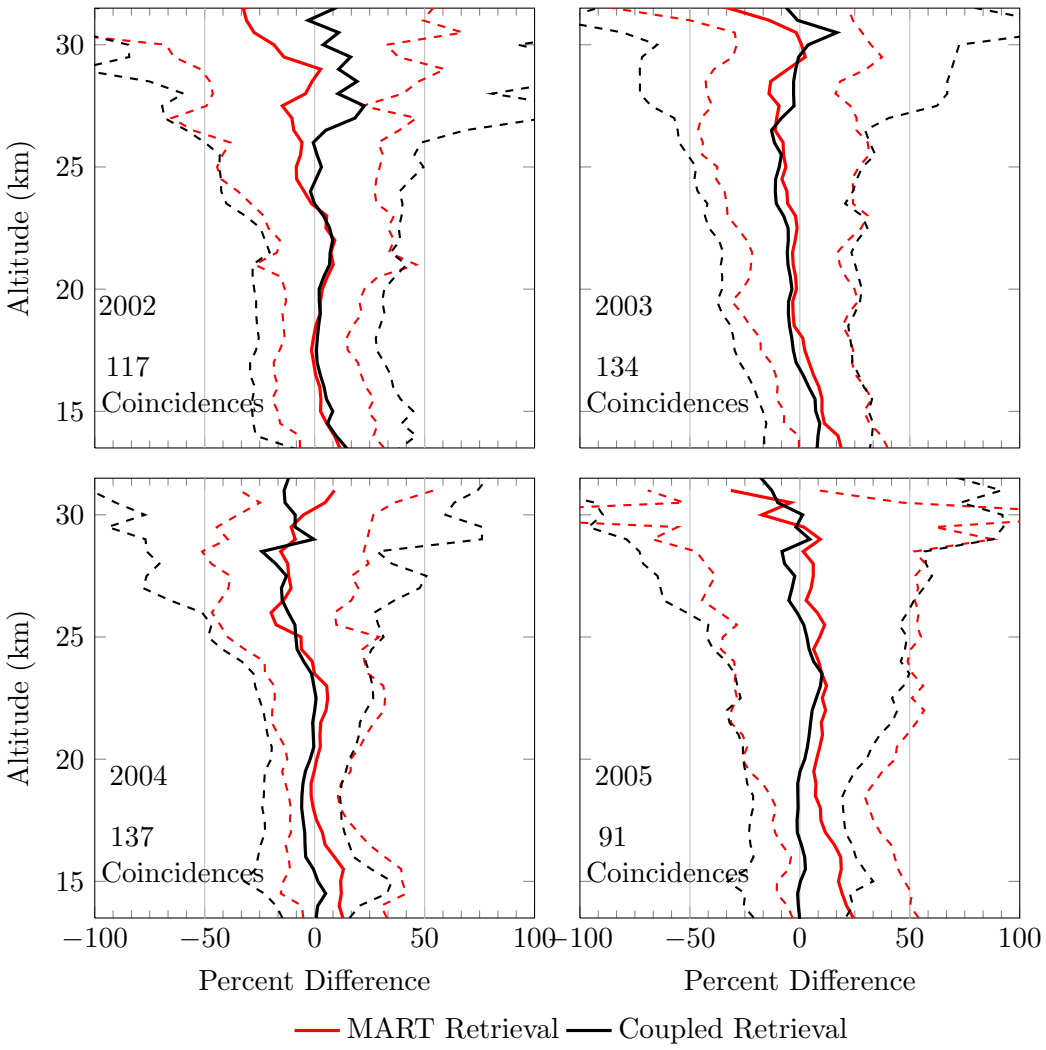

Figure 5.8: Comparison of SAGE III and OSIRIS aerosol retrievals for yearly coincident measurements. Percent difference are shown as solid lines with standard deviation shown as dashed. MART retrievals are shown in red with coupled retrievals shown in black.

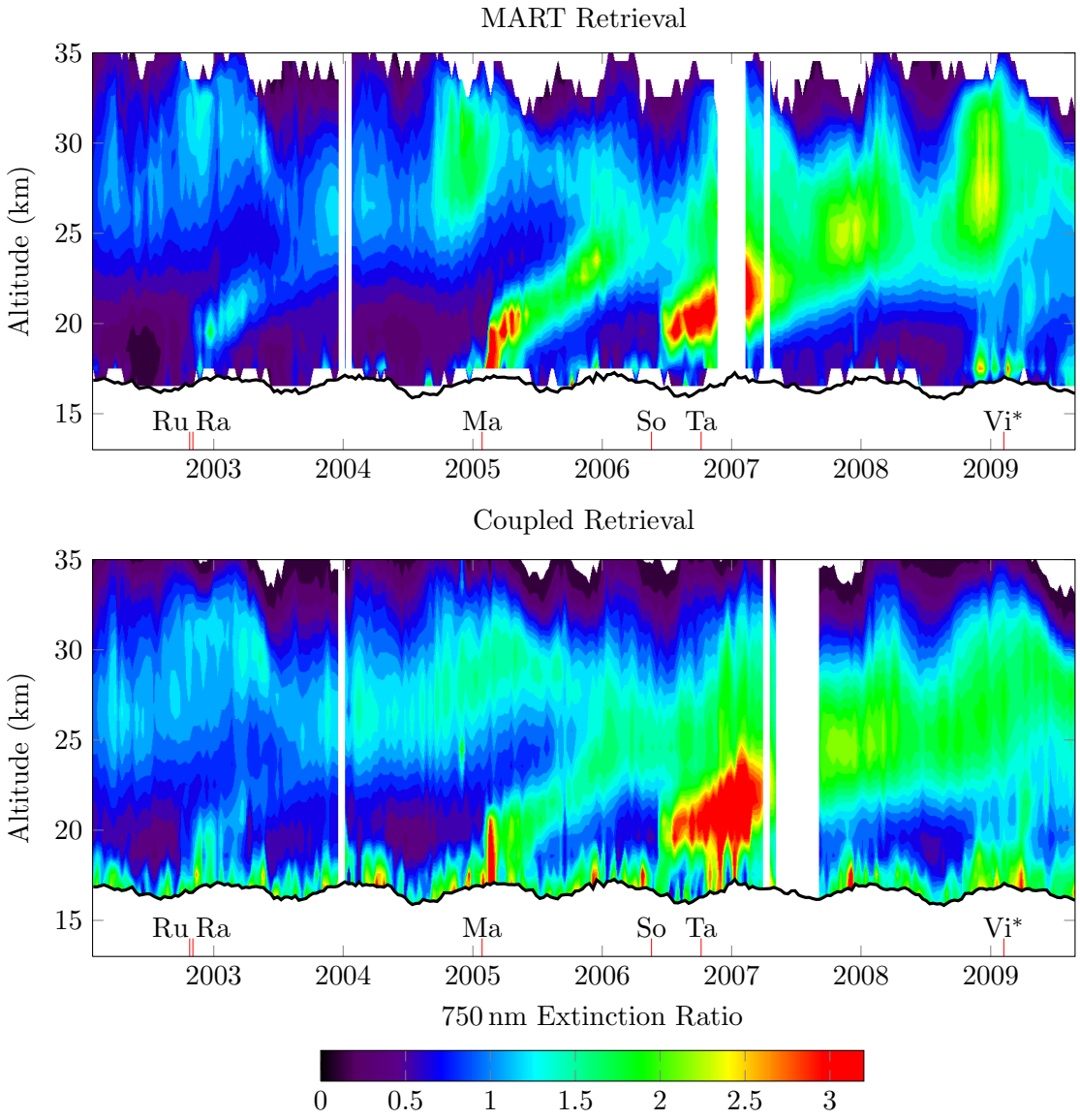

Figure 5.9: Comparison tropical extinction ratio time series using the old (top) and new (bottom) methods of retrieval. Tropopause is denoted by the black line.

Chapter 6

Conclusions

Global measurements of atmospheric extinction have been taken by numerous satellites, providing important information about the amount and evolution of stratospheric sulphate particles, particularly during the highly variable periods after volcanic eruptions. These measurements have been crucial in improving the understanding of Earth's radiative balance and the understanding of stratospheric dynamics and chemistry. In particular, limb scatter measurements have provided the opportunity to measure extinction with greater coverage than ever before. This opportunity, however, has come at the cost of increased reliance on particle size assumptions, resulting in biases in the retrieved extinction quantities. This work has focused on improving the state of the particle size assumptions using limb scatter measurements to derive particle size, both for an improved understanding of aerosol microphysics and the improved retrieval of dependent quantities such as extinction.

The information content of limb scatter measurements was examined through simulations of the OSIRIS aerosol measurement vectors, both as a function of scattering angle and wavelength. This work showed that the optical spectrograph has little sensitivity to measuring particle size, both when multiple wavelengths or multiple geometries are included. Above approximately 800 nm however, the measurements are increasingly sensitive to particle size, yielding information both as a function of wavelength and viewing geometry. The number of independent pieces of aerosol information that can be derived from OSIRIS measurements was studied by linearizing the radiative transfer problem to determine the orthogonality of the measurements. Using this linear analysis the sensitivity to different integral properties was also explored, and it was found that combining two matched pair limb measurements at 750 nm and 1.53 µm produced robust extinction values, particularly when particles are large. Analysis of the unimodal lognormal solution space using simulated measurements confirmed this sensitivity to extinction even when only one geometry was used. As well, combining measurements at these two wavelengths produced improved sensitivity to particle size, although not enough to determine a unimodal lognormal distribution uniquely.

With this information from the linear and solution space analyses, an algorithm was developed using the 750 nm and 1.53 µm measurements to couple the retrieval of aerosol number density with mode radius, assuming a lognormal size distribution with a constant mode width. While the retrieved mode radius is dependent upon the microphysical assumptions, conversion to the Ångström coefficient minimizes this dependence and produces particle size retrievals that, while still biased by assumptions, provide information on the true particle size that was not previously available to OSIRIS. Perhaps most importantly, the retrieval of a particle size parameter produces improved measurement of the aerosol extinction coefficient. This is evidenced by the improved comparisons with SAGE II, CALIPSO and SAGE III measurements, as well as the removal of biases caused by changes in viewing geometry.

This approach shows a definite improvement of the biases involved in the retrieval of stratospheric aerosol and the next step will be to implement this retrieval technique on the full set of OSIRIS measurements. While a coupled retrieval of particle size and extinction improves the accuracy of the retrieved extinction, it comes at the cost of decreased precision due to the noisier infrared data set. One possible solution to this problem is to process the data set with the new particle size algorithm to create a mode radius database that is averaged over several scans. The database can then be used as the *a priori* particle size assumption for MART retrievals using only the more precise 750 nm channel. This would allow for an improved particle size estimate while still reducing the noise involved in using the infrared channel.

A second improvement worth consideration is the estimate of the mode width parameter. The current use of a constant mode width provides reasonable results when particle size is converted to the Ångström coefficient. However, more accurate estimation of this parameter based on balloon flights and other satellite measurements may help to improve results and remove some of the biases in the retrieved Ångström coefficient.

References

Ångström, A. (1964), The parameters of atmospheric turbidity, *Tellus*, *16*, 64–75.

Andreae, M. O., and P. J. Crutzen (1997), Atmospheric aerosols: Biogeochemical sources and role in atmospheric chemistry, *Science*, *276*, 1052–1058, doi:10.1126/science.276.5315.1052.

Andrews, D. G., J. R. Holton, and C. B. Leovy (1987), *Middle Atmosphere Dynamics*, Academic Press Inc.

Baker, D. J., and A. T. Stair, Jr. (1988), Rocket measurements of the altitude distributions of the hydroxyl airglow, *Phys. Scr.*, *37*, 611–622, doi:10.1088/0031-8949/37/4/021.

Baldwin, M. P., M. Dameris, and T. G. Shepherd (2007), How will the stratosphere affect climate change?, *Science*, *316*, 1576–1577, doi:10.1126/science.1144303.

Barlow, R. J. (1989), *Statistics: A Guide to the Use of Statistical Methods in the Physical Sciences*, Wiley.

Barth, C. A., D. W. Rusch, R. J. Thomas, G. H. Mount, G. J. Rottman, G. E. Thomas, R. W. Sanders, and G. M. Lawrence (1983), Solar Mesosphere Explorer - Scientific objectives and results, *Geophys. Res. Lett.*, *10*, 237–240, doi:10.1029/GL010i004p00237.

Bauman, J. J., P. B. Russell, M. A. Geller, and P. Hamill (2003), A stratospheric aerosol climatology from SAGE II and CLAES measurements: 2. Results and comparisons, 1984-1999, *J. Geophys. Res.*, *108*, 4383, doi:10.1029/2002JD002993.

Bingen, C., D. Fussen, and F. Vanhellemont (2004), A global climatology of stratospheric aerosol size distribution parameters derived from SAGE II data over the period 1984-2000: 1. Methodology and climatological observations, *J. Geophys. Res.*, *109*, D06,201, doi:10.1029/2003JD003518.

Bourassa, A. E. (2003), The Characterization and Calibration of the OSIRIS Infrared Imager.

Bourassa, A. E. (2007), Stratospheric aerosol retrieval from OSIRIS limb scattered sunlight spectra, Ph.D. thesis, University of Saskatchewan.

Bourassa, A. E., D. A. Degenstein, R. L. Gattinger, and E. J. Llewellyn (2007), Stratospheric aerosol retrieval with optical spectrograph and infrared imaging system limb scatter measurements, *J. Geophys. Res.*, *112*, D10,217, doi:10.1029/2006JD008079.

Bourassa, A. E., L. A. Rieger, N. D. Lloyd, and D. A. Degenstein (2011), Odin-OSIRIS stratospheric aerosol data product and SAGE III intercomparison, *Atmos. Chem. Phys. Discuss.*, *11*, 25,785–25,811, doi:10.5194/acpd-11-25785-2011.

Bovensmann, H., J. P. Burrows, M. Buchwitz, J. Frerick, S. Noël, V. V. Rozanov, K. V. Chance, and A. P. H. Goede (1999), SCIAMACHY: Mission Objectives and Measurement Modes, *J. Atmos. Sci*, *56*, 127–150, doi:10.1175/1520-0469(1999)056⟨0127:SMOAMM⟩2.0.CO;2.

Brock, C. A., P. Hamill, J. C. Wilson, H. H. Jonsson, and K. R. Chan (1995), Particle Formation in the Upper Tropical Troposphere: A Source of Nuclei for the Stratospheric Aerosol, *Science*, *270*, 1650–1653, doi:10.1126/science.270.5242.1650.

Carn, S. A., A. J. Krueger, N. A. Krotkov, K. Yang, and K. Evans (2008), Tracking volcanic sulfur dioxide clouds for aviation hazard mitigation., *Nat. Haz.*, *51*, 325–343, doi:10.1007/s11069-008-9228-4.

Carslaw, K. S., B. Luo, and T. Peter (1995), An analytic expression for the composition of aqueous HNO_3-H_2SO_4 stratospheric aerosols including gas phase removal of HNO_3, *Geophys. Res. Lett.*, *22*, 1877–1880, doi:10.1029/95GL01668.

Chahine, M. I. (1972), A General Relaxation Method for Inverse Solution of the Full Radiative Transfer Equation., *J. Atmos. Sci*, *29*, 741–747, doi:10.1175/1520-0469(1972)029⟨0741:AGRMFI⟩2.0.CO;2.

Chahine, M. T. (1970), Inverse Problems in Radiative Transfer: Determination of Atmospheric Parameters., *J. Atmos. Sci.*, *27*, 960–967, doi:10.1175/1520-0469(1970)027⟨0960:IPIRTD⟩2.0.CO;2.

Chandrasekhar, S. (1960), *Radiative Transfer*, Dover, New York.

Chiou, E. W., M. P. McCormick, and W. P. Chu (1997), Global water vapor distributions in the stratosphere and upper troposphere derived from 5.5 years of SAGE II observations (1986-1991), *J. Geophys. Res.*, *102*, 19,105–19,118, doi:10.1029/97JD01371.

Chu, W. P., and M. P. McCormick (1979), Inversion of stratospheric aerosol and gaseous constituents from spacecraft solar extinction data in the 0.38-1.0-micron wavelength region, *Appl. Opt.*, *18*, 1404–1413, doi:10.1364/AO.18.001404.

Clerbaux, C., P.-F. Coheur, L. Clarisse, J. Hadji-Lazaro, D. Hurtmans, S. Turquety, K. Bowman, H. Worden, and S. A. Carn (2008), Measurements of SO_2 profiles in volcanic plumes from the NASA Tropospheric Emission Spectrometer (TES), *Geophys. Res. Lett.*, *35*, L22807, doi:10.1029/2008GL035566.

Deshler, T., M. E. Hervig, D. J. Hofmann, J. M. Rosen, and J. B. Liley (2003), Thirty years of in situ stratospheric aerosol size distribution measurements from Laramie, Wyoming (41°N), using balloon-borne instruments, *J. Geophys. Res.*, *108*, 4167, doi:10.1029/2002JD002514.

Dittman, M. G., E. Ramberg, M. Chrisp, J. V. Rodriguez, A. L. Sparks, N. H. Zaun, P. Hendershot, T. Dixon, R. H. Philbrick, and D. Wasinger (2002), Nadir ultraviolet imaging spectrometer for the NPOESS Ozone Mapping and Profiler Suite (OMPS), *Society of Photo-Optical Instrumentation Engineers*, *SPIE Conference Series*, vol. 4814, edited by W. L. Barnes, 111–119.

Dutton, E. G., P. Reddy, S. Ryan, and J. J. DeLuisi (1994), Features and effects of aerosol optical depth observed at Mauna Loa Hawaii: 1982-1992, *J. Geophys. Res.*, *99*, 8295–8306, doi:10.1029/93JD03520.

Eisinger, M., and J. P. Burrows (1998), Tropospheric sulfur dioxide observed by the ERS-2 GOME instrument, *Geophys. Res. Lett.*, *25*, 4177–4180, doi:10.1029/1998GL900128.

Elsner, J. B., A. B. Kara, and M. A. Owens (1999), Fluctuations in North Atlantic Hurricane Frequency., *J. Climate*, *12*, 427–437, doi:10.1175/1520-0442(1999)012⟨0427:FINAHF⟩2.0.CO;2.

Eparvier, F. G., D. W. Rusch, R. T. Clancy, and G. E. Thomas (1994), Solar Mesosphere Explorer satellite measurements of el Chichon stratospheric aerosols. 2: Aerosol mass and size parameters, *J. Geophys. Res.*, *99*, 20,533, doi:10.1029/94JD01841.

Gao, F., Y. Jin, C. B. Schaaf, and A. H. Strahler (2002), Bidirectional NDVI and atmospherically resistant BRDF inversion for vegetation canopy, *IEEE Trans. Geosci. Remote Sens.*, *40*, 1269–1278, doi:10.1109/TGRS.2002.800241.

Gilbert, J. F. (1971), Ranking and Winnowing Gross Earth Data for Inversion and Resolution, *Geophys. J.*, *23*, 125–128.

Graf, H.-F., J. Feichter, and B. Langmann (1997), Volcanic sulfur emissions: Estimates of source strength and its contribution to the global sulfate distribution, *J. Geophys. Res.*, *102*, 10,727–10,738, doi:10.1029/96JD03265.

Granqvist, C. G., and R. A. Buhrman (1976), Ultrafine metal particles, *J. Appl. Phys.*, *47*, 2200–2219, doi:10.1063/1.322870.

Grenfell, T. C., S. G. Warren, and P. C. Mullen (1994), Reflection of solar radiation by the Antarctic snow surface at ultraviolet, visible, and near-infrared wavelengths, *J. Geophys. Res.*, *99*, 18,669–18,684, doi:10.1029/94JD01484.

Haley, C. S., and S. Brohede (2007), Status of the Odin/OSIRIS stratospheric O3 and NO2 data products, *Can. J. Phys.*, *85*, 1177–1194, doi:10.1139/p07-114.

Hamill, P., E. J. Jensen, P. B. Russell, and J. J. Bauman (1997), The Life Cycle of Stratospheric Aerosol Particles., *Bull. Am. Meteorol. Soc.*, *78*, 1395–1410, doi:10.1175/1520-0477(1997)078⟨1395:TLCOSA⟩2.0.CO;2.

Hansen, J. E., and L. D. Travis (1974), Light scattering in planetary atmospheres, *Space Sci. Rev.*, *16*, 527–610, doi:10.1007/BF00168069.

Hayasaka, T., Y. Meguro, Y. Sasano, and T. Takamura (1998), Stratification and Size Distribution of Aerosols Retrieved from Simultaneous Measurements with Lidar, a SunPhotometer, and an Aureolemeter, *Appl. Opt.*, *37*, 961–970, doi:10.1364/AO.37.000961.

Hofmann, D. J., and S. Solomon (1989), Ozone destruction through heterogeneous chemistry following the eruption of El Chichon, *J. Geophys. Res.*, *94*, 5029–5041, doi:10.1029/JD094iD04p05029.

Hoinka, K. P. (1997), The tropopause; discovery, definition and demarcation, *Meteorol. Z.*, *6*, 281–303.

Holton, J. R., P. H. Haynes, M. E. McIntyre, A. R. Douglass, R. B. Rood, and L. Pfister (1995), Stratosphere-troposphere exchange, *Rev. Geophys.*, *33*, 403–439, doi:10.1029/95RG02097.

Horler, D. N. H., M. Dockray, and J. Barber (1983), The red edge of plant leaf reflectance, *Int. J. Remote Sens.*, *4*, 273–288, doi:10.1080/01431168308948546.

Jones, A., and R. Gattinger (1963), The seasonal variation and excitation mechanism of the 1.58 μm 1Δ g-3Σ g - Twilight airglow band, *Planet. Space Sci.*, *11*, 961 – 975, doi:10.1016/0032-0633(63)90123-5.

Jumelet, J., S. Bekki, C. David, and P. Keckhut (2008), Statistical estimation of stratospheric particle size distribution by combining optical modelling and lidar scattering measurements, *Atmos. Chem. Phys.*, *8*, 5435–5448.

Junge, C. E., C. W. Chagnon, and J. E. Manson (1961), A World-wide Stratospheric Aerosol Layer, *Science*, *133*, 1478–1479, doi:10.1126/science.133.3463.1478-a.

Kacenelenbogen, M., M. A. Vaughan, J. Redemann, R. M. Hoff, R. R. Rogers, R. A. Ferrare, P. B. Russell, C. A. Hostetler, J. W. Hair, and B. N. Holben (2011), An accuracy assessment of the CALIOP/CALIPSO version 2/version 3 daytime aerosol extinction product based on a detailed multi-sensor, multi-platform case study, *Atmos. Chem. Phys.*, *11*, 3981–4000, doi:10.5194/acp-11-3981-2011.

Kiehl, J. T., and B. P. Briegleb (1993), The relative roles of sulfate aerosols and greenhouse gases in climate forcing, *Science*, *260*, 311–314, doi:10.1126/science.260.5106.311.

Kiss, L. B., J. Söderlund, G. A. Niklasson, and C. G. Granqvist (1999), New approach to the origin of lognormal size distributions of nanoparticles, *Nanotechnology*, *10*, 25–28, doi:10.1088/0957-4484/10/1/006.

Knyazikhin, Y., J. V. Martonchik, R. B. Myneni, D. J. Diner, and S. W. Running (1998), Synergistic algorithm for estimating vegetation canopy leaf area index and fraction of absorbed photosynthetically active radiation from MODIS and MISR data, *J. Geophys. Res.*, *103*, 32,257–32,276, doi:10.1029/98JD02462.

Lacis, A., J. Hansen, and M. Sato (1992), Climate forcing by stratospheric aerosols, *Geophys. Res. Lett.*, *19*, 1607–1610, doi:10.1029/92GL01620.

Levenberg, K. (1944), A method for the solution of certain non-linear problems in least squares, *Quart. Appl. Math.*, *2*, pp. 164–168.

Llewellyn, E., and B. Solheim (1978), The excitation of the infrared atmospheric oxygen bands in the nightglow, *Planet. Space Sci.*, *26*, 533 – 538, doi:10.1016/0032-0633(78)90044-2.

Llewellyn, E., N. D. Lloyd, D. A. Degenstein, R. L. Gattinger, S. V. Petelina, A. E. Bourassa, J. T. Wiensz, E. V. Ivanov, I. C. McDade, B. H. Solheim, J. C. McConnell, C. S. Haley, C. von Savigny, C. E. Sioris, C. A. McLinden, E. Griffioen, J. Kaminski, W. F. J. Evans, E. Puckrin, K. Strong, V. Wehrle, R. H. Hum, D. J. W. Kendall, J. Matsushita, D. P. Murtagh, S. Brohede, J. Stegman, G. Witt, G. Barnes, W. F. Payne, L. Piche, K. Smith, G. Warshaw, D. L. Deslauniers, P. Marchand, E. H. Richardson, R. A. King, I. Wevers, W. McCreath, E. Kyrola, L. Oikarinen, G. W. Leppelmeier, H. Auvinen, G. Megie, A. Hauchecorne, F. Lefevre, J. de La Noe, P. Ricaud, U. Frisk, F. Sjoberg, F. von Scheele, and L. Nordh (2004), The OSIRIS instrument on the Odin spacecraft, *Can. J. Phys.*, *82*, 411–422, doi:10.1139/p04-005.

Lloyd, N. D., and E. J. Llewellyn (1989), Deconvolution of blurred images using photon counting statistics and maximum probability, *Can. J. Phys.*, *67*, 89–94.

Marquardt, D. W. (1963), An algorithm for least-squares estimation of nonlinear parameters, *J. Soc. Ind. Appl. Math.*, *11*, pp. 431–441.

McCormick, M. P., W. P. Chu, L. R. McMaster, P. Hamill, T. J. Swissler, and T. J. Pepin (1979), Satellite studies of the stratospheric aerosol, *Bull. Am. Meterol. Soc.*, *60*, 1038–1046.

McCormick, M. P., L. W. Thomason, and C. R. Trepte (1995), Atmospheric effects of the Mt Pinatubo eruption, *Nature*, *373*, 399–404, doi:10.1038/373399a0.

McKeen, S. A., S. C. Liu, and C. S. Kiang (1984), On the chemistry of stratospherics SO2 from volcanic eruptions, *J. Geophys. Res.*, *89*, 4873–4881, doi:10.1029/JD089iD03p04873.

McLinden, C. A., J. C. McConnell, E. Griffioen, C. T. McElroy, and L. Pfister (1997), Estimating the wavelength-dependent ocean albedo under clear-sky conditions using NASA ER 2 spectroradiometer measurements, *J. Geophys. Res.*, *102*, 18,801–18,811, doi:10.1029/97JD01079.

McLinden, C. A., J. C. McConnell, C. T. McElroy, and E. Griffioen (1999), Observations of Stratospheric Aerosol Using CPFM Polarized Limb Radiances, *J. Atmos. Sci.*, *56*, 233–240, doi:10.1175/1520-0469(1999)056⟨0233:OOSAUC⟩2.0.CO;2.

Mie, G. (1908), Contributions to the optics of turbid media, particularly of colloidal metal solutions (translated from german), *Ann. Phys. (Leipszig)*, *25*, 377–445.

Müller, D., U. Wandinger, and A. Ansmann (1999), Microphysical Particle Parameters from Extinction and Backscatter Lidar Data by Inversion with Regularization: Theory, *Appl. Opt.*, *38*, 2346–2357, doi:10.1364/AO.38.002346.

Oberbeck, V. R., E. F. Danielsen, K. G. Snetsinger, G. V. Ferry, W. Fong, and D. M. Hayes (1983), Effect of the eruption of El Chichon stratospheric aerosol size and composition, *Geophys. Res. Lett.*, *10*, 1021–1024, doi:10.1029/GL010i011p01021.

Oikarinen, L., E. Sihvola, and K. E. (1999), Multiple scattering radiance in limb-viewing geometry, *J. Geophys. Res.*, *104*, 31,26131,274, doi:10.1029/1999JD900969.

Pearson, K. (1901), Pearson, k. 1901. on lines and planes of closest fit to systems of points in space., *Philos. Mag.*, *2*, 559–572.

Rault, D. F., and P. Xu (2011), The OMPS Limb Profiler instrument, *AGU Fall Meeting Abstracts*, p. A179.

Renard, J.-B., J. Ovarlez, G. Berthet, D. Fussen, F. Vanhellemont, C. Brogniez, E. Hadamcik, M. Chartier, and H. Ovarlez (2005), Optical and physical properties of stratospheric aerosols from balloon measurements in the visible and near-infrared domains. III. Presence of aerosols in the middle stratosphere, *Appl. Opt.*, *44*, 4086–4095, doi:10.1364/AO.44.004086.

Robock, A. (2000), Volcanic eruptions and climate, *Rev. Geophys.*, *38*, 191–220, doi:10.1029/1998RG000054.

Rodgers, C. D. (2000), *Inverse methods for atmospheric sounding: theory and practice*, World Scientific.

Rosen, J. M. (1971), The Boiling Point of Stratospheric Aerosols., *J. Appl. Meteorol.*, *10*, 1044–1045, doi:10.1175/1520-0450(1971)010⟨1044:TBPOSA⟩2.0.CO;2.

Russell, P. B., and M. P. McCormick (1989), SAGE II aerosol data validation and initial data use - An introduction and overview, *J. Geophys. Res.*, *94*, 8335–8338, doi:10.1029/JD094iD06p08335.

Schutz, B. E., H. J. Zwally, C. A. Shuman, D. Hancock, and J. P. DiMarzio (2005), Overview of the ICESat Mission, *Geophys. Res. Lett.*, *32*, L21S01, doi:10.1029/2005GL024009.

Solomon, S., J. S. Daniel, R. R. Neely, J. P. Vernier, E. G. Dutton, and L. W. Thomason (2011), The Persistently Variable Background Stratospheric Aerosol Layer and Global Climate Change, *Science*, doi:10.1126/science.1206027.

Thomas, G. E., B. M. Jakosky, R. A. West, and R. W. Sanders (1983), Satellite limb-scanning thermal infrared observations of the El Chichon stratospheric aerosol - First results, *Geophys. Res. Lett.*, *10*, 997–1000, doi:10.1029/GL010i011p00997.

Thomason, L., and T. Peter (2006), Assessment of stratospheric aerosol properties (asap), *Tech. rep.*, WMO/ICSU/IOC World Climate Research Programme.

Thomason, L. W., and L. R. Poole (1992), Use of Stratospheric Aerosol Properties as Diagnostics of Antarctic Vortex Processes, *J. Geophys. Res.*, *98*, 23,003/23,012, doi:10.1029/93JD02461.

Thomason, L. W., and G. Taha (2003), SAGE III aerosol extinction measurements: Initial results, *Geophys. Res. Lett.*, *30*, 1631, doi:10.1029/2003GL017317.

Thomason, L. W., L. R. Poole, and T. Deshler (1997), A global climatology of stratospheric aerosol surface area density deduced from Stratospheric Aerosol and Gas Experiment II measurements: 1984-1994, *J. Geophys. Res.*, *102*, 8967–8976, doi:10.1029/96JD02962.

Thomason, L. W., J. R. Moore, M. C. Pitts, J. M. Zawodny, and E. W. Chiou (2010), An evaluation of the SAGE III version 4 aerosol extinction coefficient and water vapor data products, *Atmos. Chem. Phys.*, *10*, 2159–2173.

Tsvetsinskaya, E. A., C. B. Schaaf, F. Gao, A. H. Strahler, R. E. Dickinson, X. Zeng, and W. Lucht (2002), Relating MODIS-derived surface albedo to soils and rock types over Northern Africa and the Arabian peninsula, *Geophys. Res. Lett.*, *29*, 1353, doi:10.1029/2001GL014096.

Turco, R. P., R. C. Whitten, and O. B. Toon (1982), Stratospheric aerosols: Observation and theory, *Rev. Geophys.*, *20(2)*, 233–279, doi:10.1029/RG020i002p00233.

Twomey, S. (1977), *Introduction to the Mathematics of Inversion In Remote Sensing and Indiret Measurements*, Elsevier Scientific Publishing Company.

Vaughan, M. A., S. A. Young, D. M. Winker, K. A. Powell, A. H. Omar, Z. Liu, Y. Hu, and C. A. Hostetler (2004), Fully automated analysis of space-based lidar data: an overview of the CALIPSO retrieval algorithms and data products, *Society of Photo-Optical Instrumentation Engineers (SPIE) Conference Series*, *Society of Photo-Optical Instrumentation Engineers (SPIE) Conference Series*, vol. 5575, edited by U. N. Singh, 16–30, doi:10.1117/12.572024.

Vernier, J. P., L. W. Thomason, J. P. Pommereau, A. Bourassa, J. Pelon, A. Garnier, A. Hauchecorne, L. Blanot, C. Trepte, D. Degenstein, and F. Vargas (2011), Major influence of tropical volcanic eruptions on the stratospheric aerosol layer during the last decade, *Geophys. Res. Lett.*, *38*, L12,807, doi:10.1029/2011GL047563, Copyright 2011 American Geophysical Union.

von Savigny, C., C. S. Haley, C. E. Sioris, I. C. McDade, E. J. Llewellyn, D. Degenstein, W. F. J. Evans, R. L. Gattinger, E. Griffioen, E. Kyrölä, N. D. Lloyd, J. C. McConnell, C. A. McLinden, G. Mégie, D. P. Murtagh, B. Solheim, and K. Strong (2003), Stratospheric ozone profiles retrieved from limb scattered sunlight radiance spectra measured by the OSIRIS instrument on the Odin satellite, *Geophys. Res. Lett.*, *30*, 1755, doi:10.1029/2002GL016401.

Wandinger, U., A. Ansmann, J. Reichardt, and T. Deshler (1995), Determination of stratospheric aerosol microphysical properties from independent extinction and backscattering measurements with a Raman lidar, *Appl. Opt.*, *34*, 8315, doi:10.1364/AO.34.008315.

Waugh, D. W., and T. M. Hall (2002), Age of Stratospheric Air: Theory, Observations, and Models, *Rev. Geophys.*, *40*, doi:10.1029/2000RG000101.

Wiensz, J. T., A. E. Bourassa, N. D. Lloyd, A. Wiacek, R. V. Martin, and D. A. Degenstein (2012), Photon conservation in scattering by large ice crystals with the SASKTRAN radiative transfer model, *J. Quant. Spectrosc. Radiat. Transfer*, *113*, 582 – 593, doi:10.1016/j.jqsrt.2012.02.007.

Winker, D. M., W. H. Hunt, and M. J. McGill (2007), Initial performance assessment of CALIOP, *Geophys. Res. Lett.*, *341*, L19,803, doi:10.1029/2007GL030135.

Wiscombe, W. J. (1980), Improved Mie scattering algorithms, *Appl. Opt.*, *19*, 1505–1509, doi: 10.1364/AO.19.001505.

Wurl, D., R. G. Grainger, A. J. McDonald, and T. Deshler (2010), Optimal estimation retrieval of aerosol microphysical properties from SAGE˜II satellite observations in the volcanically unperturbed lower stratosphere, *Atmos. Chem. Phys.*, *10*, 4295–4317.

Yue, G. K., M. P. McCormick, and W. P. Chu (1986), Retrieval of composition and size distribution of stratospheric aerosols with the SAGE II satellite experiment, *J. Atmos. Oceanic Technol.*, *3*, 371–380, doi:10.1175/1520-0426(1986)003⟨0371:ROCASD⟩2.0.CO;2.

Yue, G. K., C.-H. Lu, and P.-H. Wang (2005), Comparing aerosol extinctions measured by Stratospheric Aerosol and Gas Experiment (SAGE) II and III satellite experiments in 2002 and 2003, *J. Geophys. Res.*, *110*, D11,202, doi:10.1029/2004JD005421.

Appendix A

Improving the Infrared Imager Data Set

Originally, the infrared imaging system was designed to measure oxygen singlet delta and OH Meinel band emissions, occurring at 1.27 µm and 1.53 µm respectively. The excited states of O_2 and OH, leading to these emissions are created through reactions with ozone (*Jones and Gattinger*, 1963; *Llewellyn and Solheim*, 1978), and provide important information on the chemistry and temperature of the mesosphere. Most important for the retrieval of aerosol is the OH Meinel band at 1.53 µm which has a peak altitude near 87 km with a thickness of approximately 10 km (*Baker and Stair*, 1988). Although the peak occurs well above the aerosol layer this feature has been used in the calibration of the OSIRIS data, and because even lower altitude measurements look though the layer, it is important to consider when dealing with measurements above 60 km.

The infrared imaging system is composed of three co-aligned single lens imagers measuring wavelengths of 1.26, 1.27 and 1.53 µm. Terminating each imager is a 128 pixel InGaAs photodiode array which takes a vertical profile of the atmosphere with each exposure. The vertical profiles span approximately 120 km exposing the detectors to an atmosphere with density changes of several orders of magnitude. Not including emission bands, this exposes the photodiodes to photons with an equally large range of intensities. Unsurprisingly, this greatly exceeds the sensitivity of the detectors, causing pixels at low altitudes to saturate and pixels at high altitudes to measure no physical signal at all. Each exposure then has a hard low altitude threshold where the photon count exceeds the detector limit and a soft upper limit where non-physical signals such as dark current, calibration issues and stray light begin to dominate the physical signal. Although the lower limit cannot be helped the upper limit can be improved through careful consideration and removal of the non-physical signals.

A great deal of work has been done to characterize the dark current and relative calibration of the infrared imager with large success (*Bourassa*, 2003). Despite this, the 1.53 µm channel remains difficult to use due to substantial amounts of light reaching the detectors that is not from the optical line of sight. Although present in all optical instruments to some degree, the stray light plaguing the infrared imager is particularly bad, especially at altitudes above 20-30 km, where it often composes the majority of the measured signal. While this completely excludes measurement of the OH band during the day, it also precludes using the 1.53 µm channel for additional aerosol information as the 25-35 km altitude range is needed for normalization. Although all infrared channels suffer from this stray light problem, the need for the 1.53 µm channel is of primary concern for aerosol, and thus the techniques described here, while hopefully applicable to all channels, are only considered for the 1.53 µm measurements.

A.1 Stray Light Removal

After calibration and dark current removal, a typical scan looks like that shown in Figure A.1, where each profile is an image from the detector array as Odin scans through the atmosphere. Three distinct signals are present in this scan. First, at altitudes below 20 km, is the true atmospheric signal with a steep exponential decay and "bump" around 20 km likely due to aerosol scattering. Above this, from approximately 30 to 80 km is a much more gradual exponential likely due to atmospherically scattered stray light. Finally, at higher altitudes is a signal which increases in intensity with altitude and is present only on the top 30 usable pixels (#70-100), and is thought to

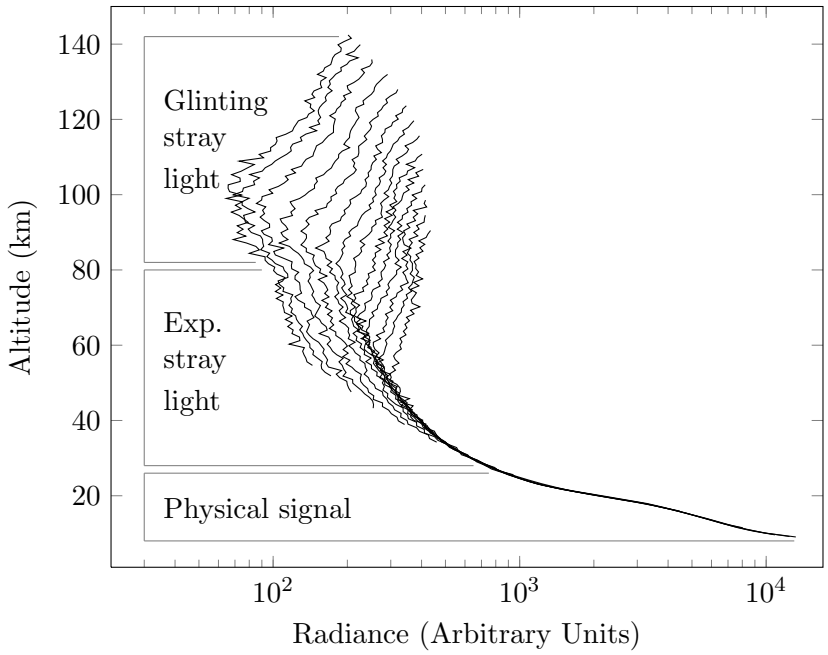

Figure A.1: Images from the 1.53 µm channel for one Odin scan after relative calibration and dark current removal but before stray light removal. Every 3rd image shown for clarity as well as the approximate ranges of the dominant signals.

be due to light glinting off of an edge of a baffle or the satellite.

A.1.1 Exponential Stray Light

The exponential stray light is the easiest to categorize, and is thus removed first. Before this however, the profiles are normalized at 41 km. Although this requires discarding any image that begins above the normalization altitude it eliminates the systematic shift in radiance as the optical axis increases in altitude and still provides data as high as 130 km. The choice of normalization altitude is as high as possible to maximize the number of images, but also low enough to ensure no glinting light is included in the normalization. Once normalized each image is fit with an exponential curve above 55 km excluding any data between 65-85 km and above pixel 70 so as not to include OH Meinel band emissions or glinting light in the fit. These fits are averaged to obtain the *a priori* exponential stray light. While this is a good estimate, the true atmospheric signal causes a slight overestimation of the stray light. To account for this the 1.53 µm signal is modelled using SASKTRAN and the slope of the exponential is adjusted such that after removal the modelled and measured signals have the same slope between 35 and 55 km. This process is shown in Figure A.2; the normalized data is shown in the left panel with the exponential fit shown in red. The right panel shows the 1.53 µm data after the exponential stray light has been removed.

A.1.2 Glinting Stray Light

Once removal of the exponential component has been finished the glinting component can be more easily categorized. Unfortunately, there is no reason for glinting light to follow a well behaved curve such as an exponential, and so a fourth order polynomial has been chosen to fit the glinting light. This was chosen to minimize the degrees of freedom while still being able to fit the complicated

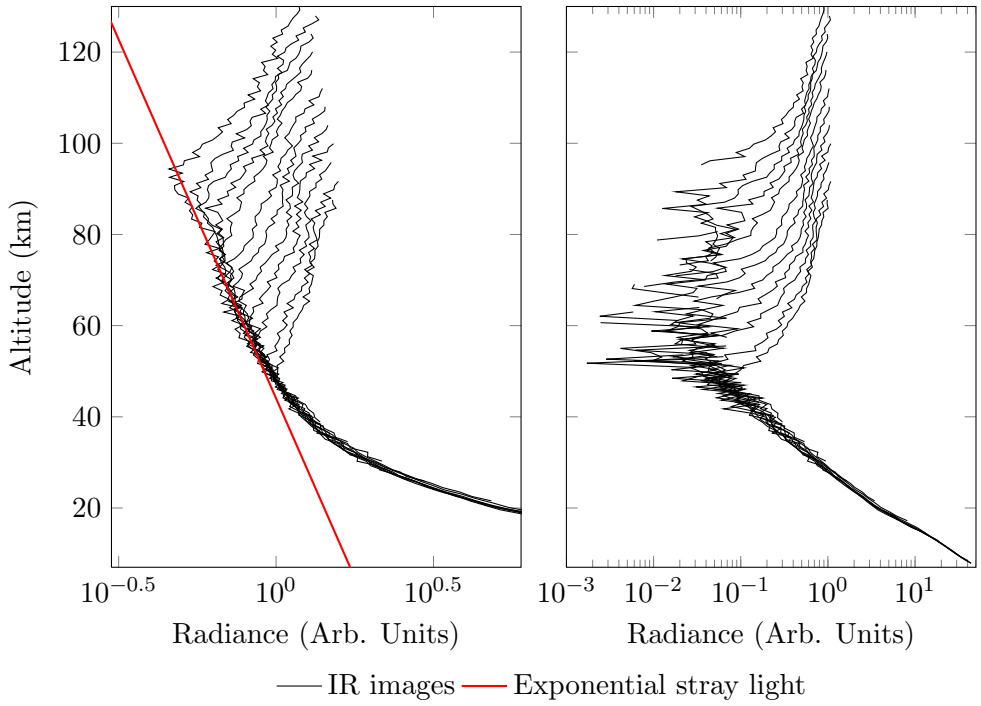

Figure A.2: Example of the exponential stray light removal process.

signal. Fortunately, the glinting signal is systematic across all images in a scan, and so all images can be fit accurately with a single polynomial, maximizing the number of data points for the high order fit. This is done by taking data from all images from pixel 70 to 100 that is not between 65 and 85 km and normalizing by the value at pixel 90. This has the effect of "stacking" the images so a single polynomial can be fit to all images simultaneously. The polynomial is then unnormalized by the value of pixel 90 and subtracted from the data to remove the glinting component of stray light. This process is shown in Figure A.3; the data with exponential stray light removed is shown in the left panel with the polynomial fit shown in red. The right panel shows the 1.53 µm data after the glinting stray light has been removed with the average profile shown in blue.

A.1.3 Results

The 1.53 µm channel now exhibits much more physically realistic behavior. Altitudes below 60 km now show an exponential profile down to approximately 20 km where enhancement due to clouds or aerosols is present. This suggests the exponential fit is working well, and provides a good quality reference altitude for normalization in the aerosol retrievals. The OH Meinel band emission is also clearly visible at 80 km whereas before it was almost completely covered by stray light, indicating the glinting stray light has been well characterized. Although individual images have substantial amounts of noise above 40 km this is expected due to nature of the infrared imager, and by combining all images from a scan into a single profile this noise can be greatly reduced.

Extending this technique to several orbits of data shows the extent of the stray light problem as well as the quality of the stray light removal technique. Figure A.4 shows the 1.53 µm data before and after stray light removal for daytime scans over the course of three orbits. The majority of the signal above 50 km has been removed, leaving only a faint signal around 80 km due to the OH Meinel band emissions. Although some of the "∨" shape remains, where the signal at a given

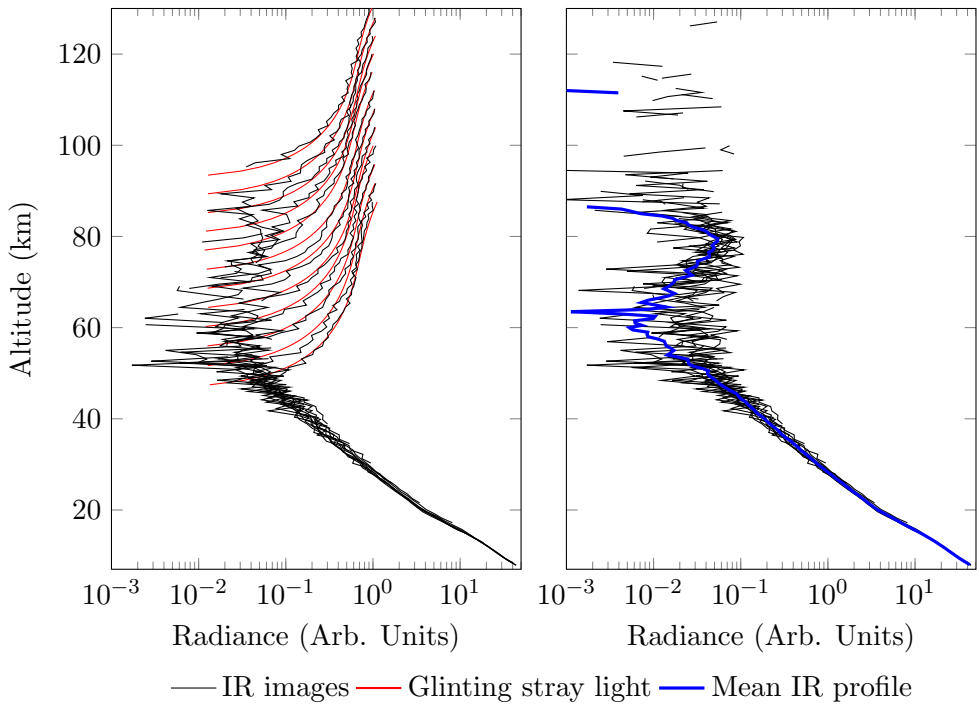

Figure A.3: Example of the glinting stray light removal process.

altitude rises and falls as Odin scans up and down, this effect has also been greatly reduced. This is particularly true for altitudes below 50 km

A.2 Altitude Registration

In addition to stray light the infrared imager also suffers from absolute altitude calibration problems. Relative altitude calibration of each pixel has been performed previously through use of the OH Meinel band emissions which occur consistently near the same altitude. As Odin scans through the emission layer each pixel should see a peak brightness at the same altitude; averaging over many thousands of scans then allows for a relative altitude calibration of each pixel by matching the peak brightness altitudes. While this is highly beneficial and eliminates the need to calibrate each pixel's altitude separately, the OH band peak is not well defined enough to calibrate the altitude absolutely, and so a new technique must be used. Aerosol structures in the stratosphere often have well defined layers, with one or more peaks at various altitudes. While the precise ratio between 1.53 µm and 750 nm measurements is dictated by particle size, the shape of the extinction profiles is highly correlated, with peaks occurring at the same altitudes. This is evidenced by the SAGE III measurements shown in Figure A.5. Panel (a) shows the 755 nm and 1.55 µm extinction measurements from a single SAGE III scan; panel (b) shows the same measurements averaged between 40°N and 50°N for all of 2004. No systematic altitude shift between the wavelengths is apparent, suggesting it is possible to calibrate the 1.53 µm channel using the aerosol features in the 750 nm measurements.

With the knowledge that the peak altitude of the aerosol measurement is approximately constant across wavelengths, multiple 750 nm measurements can be compared to 1.53 µm measurements to see the extent of the altitude shift. This was done for 25 scans spanning the length of the OSIRIS mission with well defined vertical features, and it was found that the infrared altitude needs a

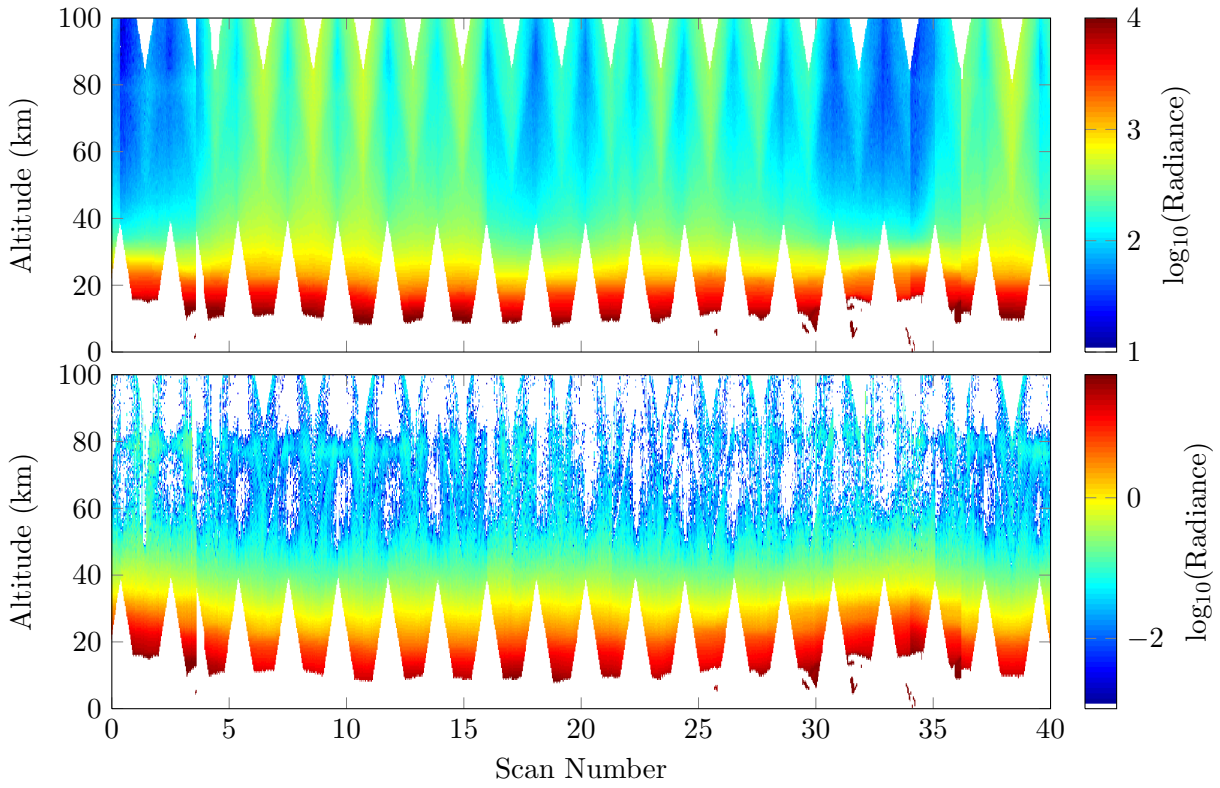

Figure A.4: Infrared images before stray light removal shown in top panel and after stray light removal shown in bottom panel.

1.75 km upward shift to be consistent with the optical spectrograph measurements. Figure A.6 shows the results of the vertical shift on two scans not used in the calibration, the first from 2002 and the second from 2009. While limited data was used for this calibration, the consistency of the necessary shift suggests it remains constant for the duration of the mission.

A.3 Future Work

Although this work has provided a much improved 1.53 µm channel, more work is yet to be done. Of primary concern is the lack of an absolute calibration. While it is possible to perform aerosol retrievals without this, due to the high altitude normalization that is performed, it eliminates the ability to retrieve the scene albedo at 1.53 µm. This is an important quantity for aerosol retrievals, and the current solution of extending the 675 nm albedo quantity to IR wavelengths undoubtedly adds error to the retrievals. One possible technique to perform an absolute calibration is to retrieve albedo over areas with well known IR reflectivity such as the Saharan desert (*Tsvetsinskaya et al.*, 2002). Calibration can then be performed by searching for the calibration parameter that yields retrieved albedos matching the known values. The current problem with this technique is the stray light removal requires normalization of the measurements at 41 km to remove the radiance shift with optical axis altitude. This normalization is different for each scan, changing the calibration parameter and making the technique above inapplicable. One possible solution is to disregard images at high altitudes, making this normalization unnecessary. While this removes much of the higher altitude information it may be necessary for an absolutely calibrated channel.

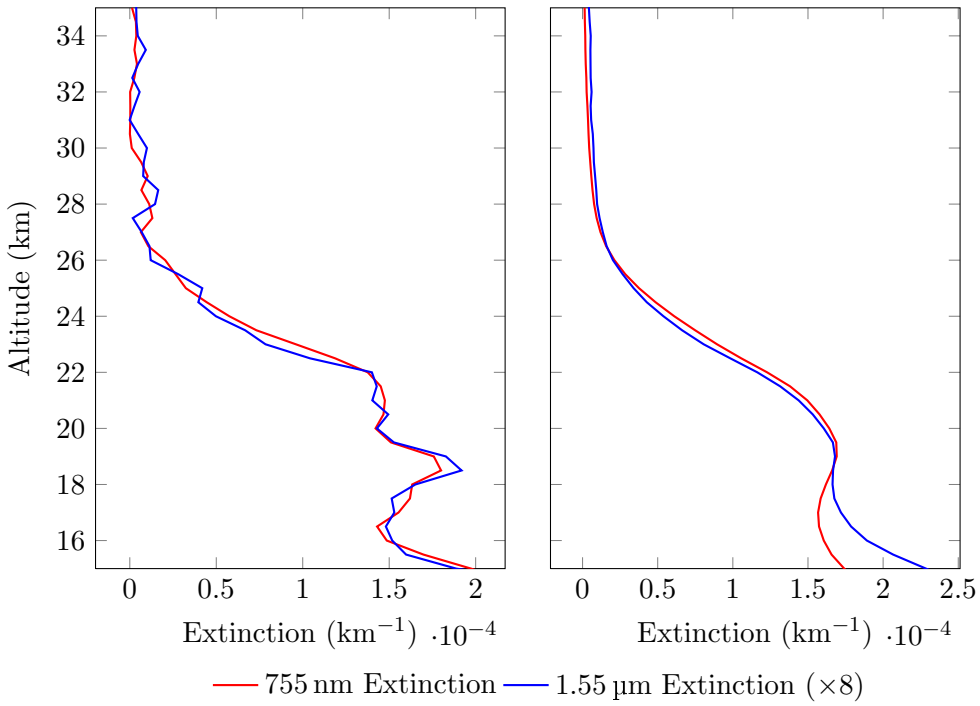

Figure A.5: 755 nm SAGE III aerosol extinction measurements shown in red with 1.55µm extinction measurements (scaled by ×8) shown in blue. Left panel is from a single scan and right panel shows average measurements for $40 - 50°$N in 2004.

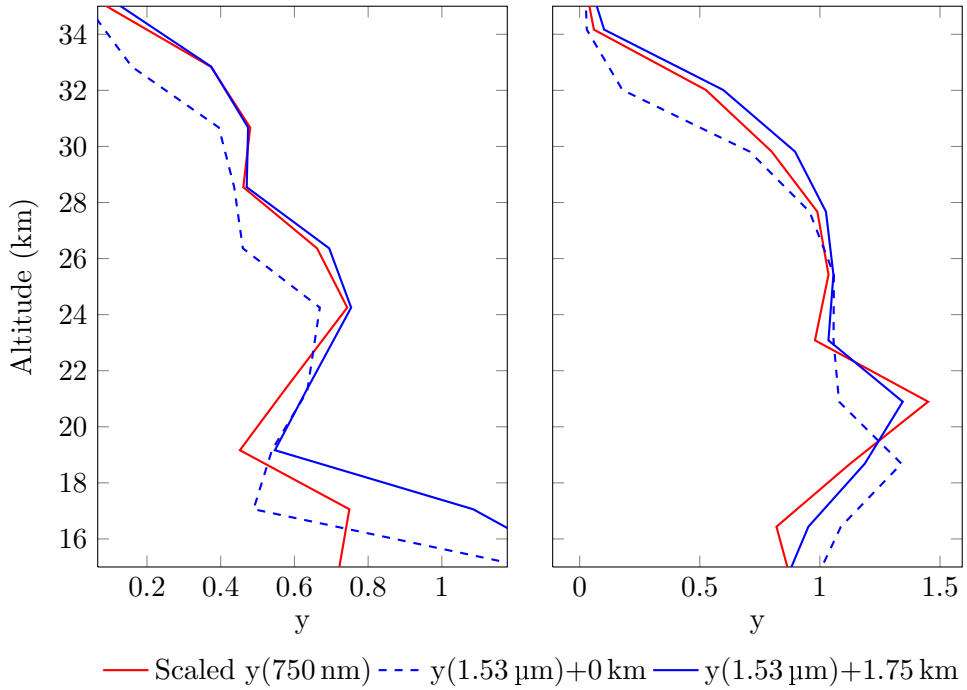

Figure A.6: OSIRIS 1.53 µm measurement vectors before and after altitude shift compared to the 750 nm measurement vectors.

Secondly, a more rigorous and possibly time dependent absolute altitude calibration should be performed. While the calibration done appears to have been successful and constant in time a larger statistical analysis may improve the results and yield information on any long term changes that were not seen in the more limited analysis.